SANDIA REPORT
SAND2009-5751
Unlimited Release
Printed September 2009

Science at the Interface: Grain Boundaries in Nanocrystalline Metals

Stephen M. Foiles
Elizabeth A. Holm
David L. Olmsted
Luke N. Brewer
David M. Follstaedt
Khalid M. Hattar
James A. Knapp
Mark A. Rodriguez
Blythe G. Clark
Douglas L. Medlin

Prepared by
Sandia National Laboratories
Albuquerque, New Mexico 87185 and Livermore, California 94550

Sandia is a multiprogram laboratory operated by Sandia Corporation,
a Lockheed Martin Company, for the United States Department of Energy's
National Nuclear Security Administration under Contract DE-AC04-94AL85000.

Approved for public release; further dissemination unlimited.

Sandia National Laboratories

Issued by Sandia National Laboratories, operated for the United States Department of Energy by Sandia Corporation.

NOTICE: This report was prepared as an account of work sponsored by an agency of the United States Government. Neither the United States Government, nor any agency thereof, nor any of their employees, nor any of their contractors, subcontractors, or their employees, make any warranty, express or implied, or assume any legal liability or responsibility for the accuracy, completeness, or usefulness of any information, apparatus, product, or process disclosed, or represent that its use would not infringe privately owned rights. Reference herein to any specific commercial product, process, or service by trade name, trademark, manufacturer, or otherwise, does not necessarily constitute or imply its endorsement, recommendation, or favoring by the United States Government, any agency thereof, or any of their contractors or subcontractors. The views and opinions expressed herein do not necessarily state or reflect those of the United States Government, any agency thereof, or any of their contractors.

Printed in the United States of America. This report has been reproduced directly from the best available copy.

Available to DOE and DOE contractors from
U.S. Department of Energy
Office of Scientific and Technical Information
P.O. Box 62
Oak Ridge, TN 37831

Telephone: (865) 576-8401
Facsimile: (865) 576-5728
E-Mail: reports@adonis.osti.gov
Online ordering: http://www.osti.gov/bridge

Available to the public from
U.S. Department of Commerce
National Technical Information Service
5285 Port Royal Rd.
Springfield, VA 22161

Telephone: (800) 553-6847
Facsimile: (703) 605-6900
E-Mail: orders@ntis.fedworld.gov
Online order: http://www.ntis.gov/help/ordermethods.asp?loc=7-4-0#online

SAND200X-XXXX
Unlimited Release
Printed September 2009

Science at the Interface: Grain Boundaries in Nanocrystalline Metals

Stephen M. Foiles, Elizabeth A. Holm, Luke N. Brewer, David L. Olmsted
Computational Materials Science and Engineering Department

David M. Follstaedt, Khalid M. Hattar, James A. Knapp, Blythe B. Clark
Radiation-Solid Interactions

Mark A. Rodriguez
Materials Characterization

Doug L. Medlin
Materials Physics

Sandia National Laboratories
P.O. Box 5800
Albuquerque, New Mexico 87185-MSXXXX

ABSTRACT

Interfaces are a critical determinant of the full range of materials properties, especially at the nanoscale. Computational and experimental methods developed a comprehensive understanding of nanograin evolution based on a fundamental understanding of internal interfaces in nanocrystalline nickel. It has recently been shown that nanocrystals with a bi-modal grain-size distribution possess a unique combination of high-strength, ductility and wear-resistance. We performed a combined experimental and theoretical investigation of the structure and motion of internal interfaces in nanograined metal and the resulting grain evolution. The properties of grain boundaries are computed for an unprecedented range of boundaries. The presence of roughening transitions in grain boundaries is explored and related to dramatic changes in boundary mobility. Experimental observations show that abnormal grain growth in nanograined materials is unlike conventional scale material in both the level of defects and the formation of unfavored phases. Molecular dynamics simulations address the origins of some of these phenomena.

ACKNOWLEDGMENTS

This program benefitted from collaborations sponsored by the U.S. Department of Energy's, Office of Basic Energy Sciences both through the core program at Sandia and through the Computational Materials Science Network program.

CONTENTS

1. Science at the interface: grain boundaries in nanocrystalline metals 9
1.1. Overview 9
1.2. References 14

2. A new class of metrics for the macroscopic crystallographic space of grain boundaries..... 17
2.1. Abstract 17
2.2. Introduction 17
2.3. Approach 18
2.4. Definition of the macroscopic crystallographic space of grain boundaries. 19
2.5. Definition of the metrics 21
2.6. Comments and comparisons 22
2.7. Sample calculations 22
2.8. Conclusions 24
2.9. Appendices 24
2.9.1. Appendix A 24
2.9.2. Appendix B 25
2.9.3. Appendix C 26
2.9.4. Appendix D. 27
2.10. References 27

3. Grain boundary interface roughening transition and its effect on grain boundary mobility for non-faceting boundaries 29
3.1. Abstract 29
3.2. Introduction 29
3.3. Approach and Results 30
3.4. Summary 36
3.5. References 37

4. Survey of grain boundary properties in FCC metals: I. Grain boundary energy 39
4.1. Abstract: 39
4.2. Introduction: 39
4.3. Computational Approach: 41
4.4. Results 44
4.5. Summary 51
4.6. Appendix A 53
4.7. References 53

5. Survey of grain boundary properties in FCC metals II: Grain boundary mobility 59
5.1. Abstract 59
5.2. Introduction 59
5.3. Method 61
5.3.1. The synthetic driving force method 61
5.3.2. Simulation parameters 64
5.4. Results and discussion 65
5.4.1. Mobility as a function of disorientation 65
5.4.2. Shear coupled motion 66

5.4.3. Mobility correlations 68
5.4.4. Temperature effects 71
5.5. Conclusions 76
5.6. Appendix A 77
5.7. References 77

6. Competitive Abnormal Grain Growth between Allotropic Phases in Nanocrystalline Nickel 81
6.1. Abstract 81
6.2. Introduction 81
6.3. Experimental Methods. 82
6.4. Results 82
6.5. Discussion 86
6.6. Conclusions 87
6.7. References: 87

7. Temperature dependence of grain boundary free energy and elastic constants 89
7.1. Abstract 89
7.2. Introduction 89
7.3. Computational Method 90
7.4. Results and Discussion 91
7.5. Summary 94
7.6. References 95

8. Direct molecular dynamics simulations of nanocrystalline grain growth 97
8.1. Introduction 97
8.2. Computational Method 97
8.3. Results 99
8.4. References 102

9. Distribution 103

FIGURES

Figure 1-1. TEM of Nanograined Ni 11
Figure 2-1. Energy difference as a function of crystallographic distance 23
Figure 2-2. Energy of Ni boundaries by their distance from coherent twin 24
Figure 3-1. Velocity as a function of driving force 31
Figure 3-2. Roughness as a function of temperature 32
Figure 3-3. Mobility as a function of driving force 33
Figure 3-4. Motion of grain boundary I 34
Figure 3-5. Roughness as a function of temperature 35
Figure 3-6. Mobility as a function of driving force 36
Figure 4-1. Minimized energy of set of initial structures 44
Figure 4-2. Grain boundary energy versus disorientation angle 45
Figure 4-3. Grain boundary energy versus inverse density of coincident sites 46
Figure 4-4. Grain boundary energy versus excess volume 47
Figure 4-5. Grain boundary energy versus angle to <111> direction 48

Figure 4-6. Energy difference of grain boundary pairs..... 49
Figure 4-7. Comparison of the grain boundary energy of Ni and Al..... 50
Figure 5-1. Mobility versus disorientation angle..... 66
Figure 5-2. Correlation between shear and energy or mobility 67
Figure 5-3. Correlations of mobility with other properties..... 70
Figure 5-4. Difference of mobility between boundary pairs..... 72
Figure 5-5. Temperature dependence of mobility..... 73
Figure 5-6. Distribution of roughening transition temperature..... 75
Figure 6-1. EBSD patterns for HCP nickel..... 83
Figure 6-2. EBSD phase maps of abnormally grown grains 83
Figure 6-3. Pole figures of FCC and HCP grains 84
Figure 6-4. TEM image and diffraction patterns from a abnormal HCP grain..... 85
Figure 6-5. Powder x-ray diffraction from as-deposited nickel thin film..... 86
Figure 7-1. Temperature dependence of grain boundary free energy..... 92
Figure 7-2. Temperature dependence of the elastic moduli..... 93
Figure 7-3. Scaled temperature dependent grain boundary free energy 94
Figure 8-1. Representative snapshots of MD simulated grain growth..... 100
Figure 8-2. Time evolution of grain size 101

TABLES

Table 4-1. Ratios of Ni and Al material properties..... 51

NOMENCLATURE

MD	Moelcular Dynamics
EAM	Embedded Atom Method
LAMMPS	Large-scale Atomistic Molecular Massively Parallel Simulator
TEM	Transmission Electron Microscopy
CSL	Coincident Site Lattice
DSC	Displacement Shift Complete Lattice
$\sum$	Inverse Density of Coincident Sites
DOE	Department of Energy
SNL	Sandia National Laboratories

1. Science at the interface: grain boundaries in nanocrystalline metals

1.1. Overview

In virtually every engineered material, interfaces – from free surfaces to interphase and grain boundaries –critically affect mechanical, electrical, optical and thermal properties as well as materials processing, stability and reliability [1-3]. The importance of interfaces is further magnified in nanostructured materials, where interfaces comprise a substantially greater proportion of the system.

Over the last several years, there has been increasing interest in incorporating improved descriptions of grain boundary properties in mesoscale simulations of microstructural evolution [4-7]. Realistic microstructural-scale simulations have revealed the powerful influence of boundary properties on microstructural processes, including normal and abnormal grain growth, texture development, and recrystallization. This has prompted substantial experimental and computational efforts to determine fundamental boundary properties as a function of grain boundary structure (misorientation and boundary plane) and to extend mesoscale simulations to incorporate this extra information. The available methods limit the scope of the results, however. For example, experimental efforts focus either on the average mobility of an ensemble of boundaries, ignoring boundary structure entirely, or on single, special boundaries, neglecting the diversity of boundary types. In a few special cases, molecular dynamics simulations have been used to examine boundary mobility; these simulations have their own limitations. Simulations of curved boundaries only provide information on the product of the boundary mobility and boundary stiffness; simulations of elastically strained bicrystals can model only those boundaries where elastic anisotropy can provide a sufficient driving force. Prior to this project, there was no experimental or computational toolkit for determining boundary properties over the range of boundary structure and crystallography.

Advances in the prediction of the properties of internal interfaces using novel atomistic simulations and advanced experimental methods have occurred at Sandia and elsewhere that allow for advancements in these areas. In particular, two novel molecular dynamics techniques that provide information about boundary properties that was previously unobtainable were developed prior to this project. In the first method, the fluctuations of grain boundary position are analyzed to determine both the boundary mobility and the boundary stiffness [8]. The stiffness is the sum of the grain boundary free energy and its second derivative with respect to boundary orientation and gives the driving force for curvature driven grain growth. This work is the first determination of grain boundary stiffness and provided unexpected results concerning the influence of crystallographic direction on stiffness. The second new method determines the true mobility of an arbitrary, flat grain boundary by applying an artificial driving force for boundary motion [9]. Prior to this project, this approach had only been used for preliminary demonstration calculations. These preliminary calculations showed that the boundary mobility is strongly dependent on the orientation of the boundary plane, contravening the usual assumption that the mobility depends only on the crystallographic misorientation between the grains.
These new simulation techniques for determining grain boundary properties complement atomic (atom-probe tomography) and nanoscale (TEM/SEM) observation of these features. High-resolution TEM observations of single boundaries have revealed previously unknown finite size

effects on grain boundary structure [10] and the effects of multi-boundary junctions on boundary structure [11, 12]. Both of these phenomena are particularly crucial in nanocrystalline materials, which contain a large volume fraction of short boundaries connected to one another at multi-boundary junctions. Atom-probe examination of boundaries in electrodeposited nanocrystalline Ni has disclosed the segregation and metastable precipitation of solutes at certain boundaries, both of which appear important to the thermal stability in these materials. Similarly, our TEM observations of nanocrystalline boundary networks provide the as-yet-unexplained observation that while microscale boundary motion removes lattice defects, nanoscale grain boundary motion appears to create them [13]. In particular, as shown in Figure 1, stacking fault tetrahedra are found in the abnormal Ni grains even though abnormal grain growth or recrystallization in traditional materials produces essentially defect free grains.

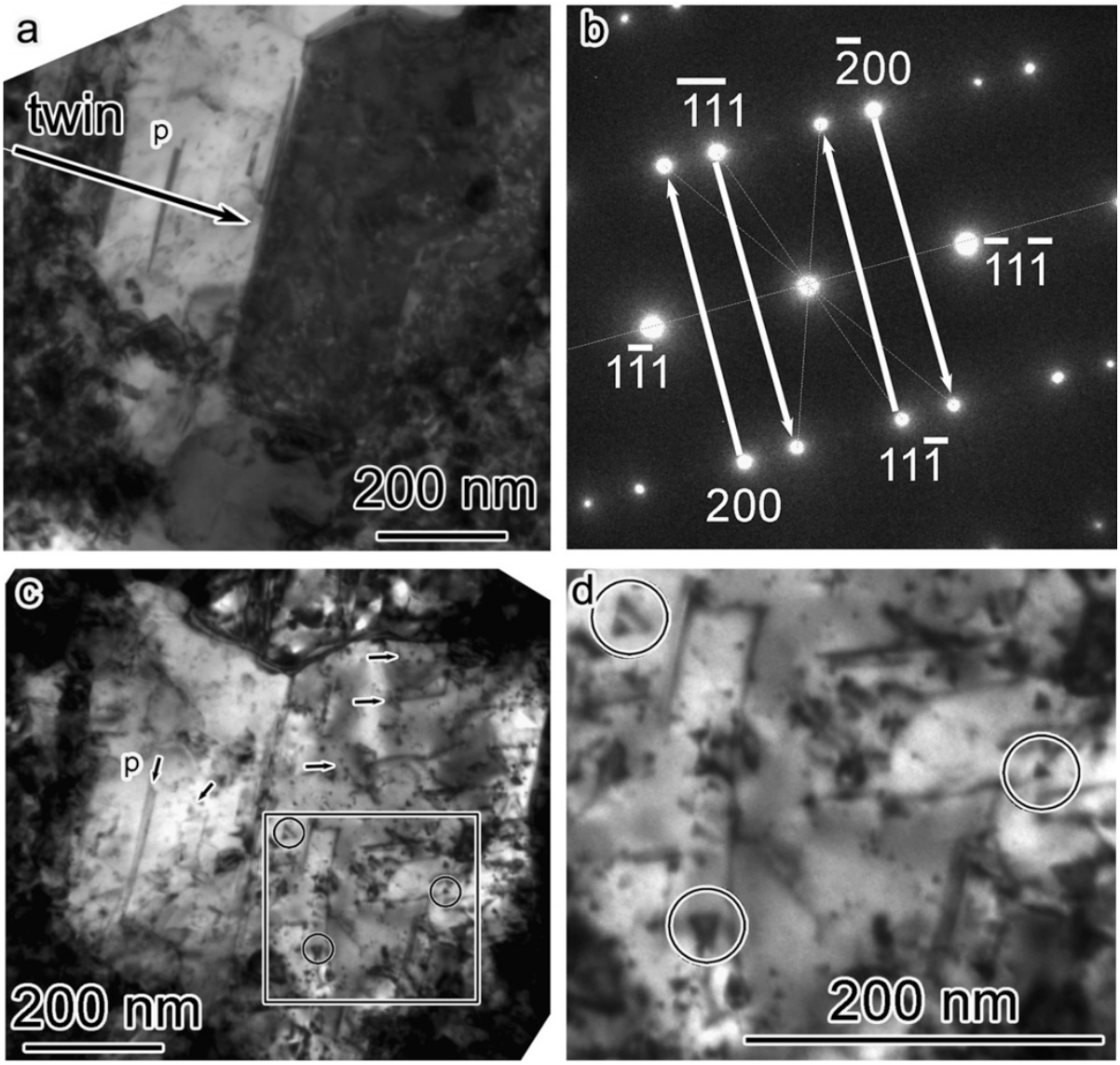

Figure 1-1. TEM of Nanograined Ni
(a) A large twinned grain in a 150-nm-thick film after annealing at 548 K for 20 min. (b) Electron diffraction pattern demonstrating the twinned relationship between the two grains. The arrows indicate the relationship between the matrix and twin diffraction spots. (c) Defect structure in the twinned grains; stacking-fault tetrahedra are circled, a planar defect is labeled p, and dislocations are arrowed. (d) Enlargement of the indicated area in (c) in which stacking-fault tetrahedra are circled. From reference [13].

The effects of grain boundary motion manifest on the mesoscale by governing the polycrystalline evolution that influences material properties. Sandia has a strong record of incorporating boundary structure and properties information into mesoscale models for the evolution of polycrystalline boundary networks. For example, the first simulations that included crystallographically dependent boundary energy and mobility in a realistic grain structure elucidated the nucleation mechanism in recrystallization [14]. Nanoscale polycrystals require additional physical information and input, however. For example, grain rotation has been shown to be an important grain growth mechanism for nanocrystals, though it is insignificant in

microscale polycrystals. Likewise, as our TEM and atom-probe observations indicate, finite size effects, defect incorporation mechanisms, solutes and precipitates, and film structure all influence how and where boundaries move in a nanocrystal. Thus, a comprehensive approach to nanostructural evolution requires a new integration of experimental observations and atomic-scale information into a mesoscale model that can capture the fundamental evolution processes. In this project, we applied and extended our novel computational and experimental methods to develop the first comprehensive characterization of internal interfaces in novel materials using nanocrystalline nickel as our benchmark. In nanocrystalline materials the network of grain boundaries has a profound effect on mechanical properties – strength, ductility, and toughness. The controversial Reverse Hall-Petch effect, where strength decreases below a threshold grain size, is a result of the scale and properties of the grain boundary network, as is the embrittlement and decreased ductility seen at nanoscale grain sizes. Intriguingly, investigators have recently shown that nanocrystals with a bimodal grain size distribution, containing a network of microscale grains in a nanoscale matrix, possess a unique combination of high strength, ductility, and wear-resistance [15]. Achieving a bimodal distribution of grain sizes is straightforward; nanocrystalline Ni undergoes abnormal grain growth just above room temperature [13]. However, under typical processing conditions, abnormal growth may proceed too far, consuming the nanocrystalline matrix. Thus, an understanding of the range of stability of the abnormal grain structure is important for the ultimate engineering applications of these materials, so structural stability is also of interest. This project will focus on computational and experimental characterization of the interfaces in such materials with the goal of understanding the interface properties that control the microstructural evolution and stability.

In this project, there have been several advances in the computational and theoretical understanding of the properties of grain boundaries as a function of the macroscopic degrees of freedom of the boundary. Recall that grain boundary crystallography is defined in a five dimensional space. The theoretical challenge is to understand the variation of properties within this space. This understanding can then be incorporated into mesoscale models of grain growth. The first contribution of this project was to address a long-standing fundamental mathematical issue with regard to grain boundary crystallography, namely the definition of a metric of the distance in crystallographic space between two macroscopic grain boundary geometries. The absence of such a metric had been discussed in detail by Cahn and Taylor [16]. Aside from the formal importance of such a metric, it is critical from a practical point of view. In the absence of an analytical model for the variation of some grain boundary property, a potential alternative is to develop a large database of properties as a function of crystallography and then interpolate in this database to estimate the properties of the desired boundary. A fundamental prerequisite for any interpolation scheme, though, is the definition of a metric that defines the “distance” between two grain boundary orientations. Chapter 2 (see also Olmsted [17]) presents such a metric along with a discussion of the formal mathematical properties of the metric. In addition, results are presented that demonstrate, at least for the case of grain boundary energy, that nearby boundary geometries have similar properties.

A key grain boundary property is the boundary mobility. This is the proportionality constant between the boundary velocity and the driving force for boundary motion and is a key quantity to describe grain evolution. The mobility has till now only been examined in a small number of studies. It has generally been assumed that the temperature dependence of the mobility follows

Arrhenius behavior typical of an activated process. Chapter 3 (see also Olmsted, Holm and Foiles [18]) presents a study, using the new synthetic driving force method mentioned above, of the temperature dependence. The results demonstrate that the temperature dependence of the mobility is far more complex. In particular, it is observed that there is a temperature at which there is an abrupt change in the mobility. This temperature is shown to correspond to a roughening transition. Below the transition temperature, smooth boundaries, the mobility is low while above the transition temperature the mobility is high. The presence of such a transition in the mobility with temperature had not been previously suspected and will have significant implications for grain evolution.

Chapter 4 (see also Olmsted, Foiles and Holm [19]) presents the most complete computational survey to date of the grain boundary energy as a function of the boundary crystallography. A set of 388 boundary orientations is generated. Previous studies have considered the variation of energy with respect to some subset of the crystallographic space. In this study, boundaries throughout the crystallographic space are considered. For each boundary, a careful structural optimization of the structure was performed and the energy computed. This dataset was used to examine various correlations between energy and crystallography that have been discussed previously in the literature. It was shown that none of these correlations provide useful predictors of boundary energy. The dataset can also be used in an interpolative fashion to estimate boundary energy. Results are presented that allow the estimation of the accuracy of such interpolations.

Chapter 5 (see also Olmsted, Holm and Foiles [20]) presents the first ever study of the variation of grain boundary mobility with respect to boundary crystallography. In this study, the grain boundary mobility was computed as a function of temperature for the set of 388 grain boundaries studied above. Several new observations of the variation of the mobility were made. It was seen that some boundaries move by the coupled shear mechanism and that this mechanism generally leads to high mobility. Various correlations between the high-temperature mobility and boundary crystallography are examined, but no predictive correlations were found. Finally, a crude estimate of the distribution of roughening transition temperatures was made.

A surprising experimental observation regarding the annealing of nanocrystalline Ni is presented in Chapter 6 (see also Brewer, et al. [21]). Thin films samples of pulse laser deposited (PLD) Ni were annealed at various temperatures with the intent of examining abnormal grain growth in this system. Recall that the equilibrium structure of Ni is face-centered-cubic (FCC). It was observed that some of the large abnormal grains have a highly defected structure close to hexagonal-close-packed (HCP). These large ‘HCP’ grains are surrounded by nanocrystalline grains with the FCC structure. It is therefore unexpected that grains with a nonequilibrium, higher-energy structure would grow at the expense of the grains in the equilibrium structure. Extensive characterization of these ‘HCP’ grains has been carried out. This observation is still unexplained, though it does point to the possibility of creating novel nonequilibrium structures in nanocrystalline metals.

Chapter 7 (see also Foiles [22]) concerns finite temperature effects on grain boundary properties. Even though almost all studies of grain boundary energy have calculated the zero-temperature excess enthalpy of the boundary, the quantity relevant to grain growth is the grain boundary free

energy. This quantity is much more difficult to compute due to the need to perform some form of thermodynamic integration. Here it is shown that the temperature dependence of the free energy can be estimated from the temperature dependence of the bulk elastic properties. This result will be of value to future studies that require an estimate of the free energy.

The final chapter presents direct molecular dynamics (MD) simulations of the grain growth of nanocrystalline metals. There are two interesting observations from these simulations. The first is that the MD simulations reproduce the experimental observation of Hattar et al. [13] that such growth produces defected grains. The presence of vacancy production within the grains is verified. More striking is the formation of a high density of twin boundaries during the growth process. Visualization of the growth provides insight into the mechanism of twin boundary formation in this case. The second observation concerns the grain growth kinetics. It is seen that at early times that the average grain size increases with the square root of time. This is consistent with the behavior of conventional scale grain growth and indicates that in this respect nanoscale systems do not behave differently than conventional scale metals. More surprising is the observation of grain growth stagnation. This is speculated to be a consequence of the bimodal distribution of mobilities that result from the roughening transition discussed above [18, 20]. This is relevant to a long-standing experimental observation that grain growth stagnates in real systems. This is an area that warrants further study.

1.2. References

[1] Gottstein G, Shvindlerman LS. Grain Boundary Migration in Metals: Thermodynamics, Kinetics, Applications. Boca Raton: CRC Press, 1999.

[2] Humphreys FJ, Hatherly M. Recrystallization and Related Annealing Phenomena. Oxford: Elsevier, 1995.

[3] Sutton AP, Balluffi RW. Interfaces in Crystalline Materials. Oxford: Clarendon Press, 1995.

[4] Gruber J, George DC, Kuprat AP, Rohrer GS, Rollett AD. Effect of Anisotropic Grain Boundary Properties on Grain Boundary Plane Distributions during Grain Growth. Scripta Materialia 2005;53:351.

[5] Holm EA, Hasson GN, Miodownik MA. On Misorientation Distribution Evolution during Anisotropic Grain Growth. Acta Materialia 2001;49:2981.

[6] Kazaryan A, Wang Y, Dregia SA, Patton BR. Grain Growth in Anisotropic Systems: Comparison of Effects of Energy and Mobility. Acta Materialia 2002;50:2491.

[7] Upmanyu M, Hassold GN, Kazaryan A, Holm EA, Wang Y, Patton B, Srolovitz DJ. Boundary Mobilityu and Energy Anisotropy Effects on Microstructural Evolution During Grain Growth. Interface Science 2002;10:201.

[8] Foiles SM, Hoyt JJ. Computation of Grain Boundary Stiffness and Mobility from Boundary Fluctuations. Acta Materialia 2006;54:3351.

[9] Janssens KGF, Olmsted D, Holm EA, Foiles SM, Plimpton SJ, Derlet PM. Computing the Mobility of Grain Boundaries. Nature Materials 2006;5:124.

[10] Marquis EA, Hamilton JC, Medlin DL, Leonard F. Finite-Size Effects on the Structure of Grain Boundaries. Physical Review Letters 2004;93:156101.

[11] Lucadamo G, Medlin DL. Geometric Origin of Hexagonal Close Packing at a Grain Boundary in Gold. Science 2003;300:1272.
[12] Marquis EA, Medlin DL, Leonard F. Stabilization of extended stacking faults by {111}/{112} twin junction interactions. Acta Materialia 2007;55:5917.
[13] Hattar K, Follstaedt DM, Knapp JA, Robertson IM. Defect structures created during abnormal grain growth in pulsed-laser deposited nickel. Acta Materialia 2008;56:794.
[14] Holm EA, Miodownik MA, Rollett AD. On abnormal subgrain growth and the origin of recrystallization nuclei. Acta Materialia 2003;51:2701.
[15] Wang Y, Chen M, Zhou F, Ma E. High tensile uctility in a nanostructured metal. Nature 2002;419:912.
[16] Cahn JW, Taylor JE. Metrics, Measures, and Parametrizations for Grain Boundaries: A Dialog. Journal of Materials Science 2006;41:7669.
[17] Olmsted DL. A New Class of Metrics for the Macroscopic Crystallographic Space of Grain Boundaries. Acta Materialia 2009;57:2793.
[18] Olmsted DL, Foiles SM, Holm EA. Grain boundary interface roughening transition and its effect on grain boundary mobility for non-faceting boundaries. Scripta Materialia 2007;57:1161.
[19] Olmsted D, Foiles SM, Holm EA. Survey of computed grain boundary properties in face-centered cubic metals: I. Grain boundary energy. Acta Materialia 2009;57:3694.
[20] Olmsted D, Holm EA, Foiles SM. Survey of computed grain boundary properties in face-centered cubic metals: II. Grain boundary mobility. Acta Materialia 2009;57:3704.
[21] Brewer LN, Follstaedt DM, Hattar KM, Knapp JA, Rodruguez MA, Robertson IM. Competitive Abnormal Grain Growth between Allotropic Phases in Nanocrystalline Nickel. Advances in Materials in press.
[22] Foiles SM. Temperature dependence of grain boundary free energy and elastic constants. Scripta Materialia submitted.

2. A new class of metrics for the macroscopic crystallographic space of grain boundaries.

2.1. Abstract

The macroscopic description of a defect-free, flat grain boundary in a pure material requires five degrees of freedom [1]. There is a need to define the distance between boundaries in this five dimensional space, because boundaries that are close together crystallographically should have similar properties. A. Morawiec has recently proposed such a metric, defined in terms of the misorientation of the two grains and their boundary normals [2]. This approach has the disadvantage that there is no unique way of weighting the importance of the difference in disorientation compared to the difference in boundary normals, as was pointed out by Cahn and Taylor [3]. In this work a metric is developed using a less familiar description of the crystallographic space which avoids this problem. Two technical results are proven, and a sample application to grain boundary properties is offered.

2.2. Introduction

The macroscopic description of a defect-free, flat grain boundary in a pure material requires five degrees of freedom [1]. As any of these degrees of freedom is changed, one expects that the properties of the boundary will change continuously. Traditionally grain boundaries were considered similar if they were close together in the misorientation space, which considers only three of the five macroscopic degrees of freedom. In particular the Brandon criterion [4] is based on a definition of when boundaries are close in misorientation space. However properties can vary greatly between different boundaries with the same misorientation [5]. While it had typically not been possible to study boundaries in terms of all five degrees of freedom, that has been changing recently, both experimentally and computationally [6,7,8,9,10]. Thus methods are needed which assess closeness with respect to boundary normal as well as misorientation, in other words with respect to all five degrees of freedom. A. Morawiec has recently proposed a metric defined on this space, described in terms of the misorientation of the two grains, and the boundary normal [2]. While this is one of the standard ways of defining the crystallographic space, in the context of building a metric it has the disadvantage that there is no unique way of weighting the importance of the difference in disorientation between two grains with the difference in boundary normals, as was pointed out by Cahn and Taylor [3]. In this work a new metric, and a variant of it, is developed in terms of a less familiar description of the crystallographic space which avoids this problem. This parameterization of the five dimensional space of grain boundaries, while having a noticeable disadvantage compared to the two common parameterizations, has advantages which should make it of value in other contexts as well. Two important technical results about the metrics are shown. First that the coincident site lattice (CSL) boundaries with rational boundary normals are dense in the space of grain boundaries. These special boundaries can then serve as approximations to any boundary, just as the rational numbers provide approximations to real numbers. Secondly, it is shown that the new metrics

and Morawiec's metric induce the same topology on the crystallographic space. Thus the answers to some questions, for example "is this point a local minimum of the grain boundary energy?", do not depend on which metric is chosen. As an example of the application of this metric to the analysis of grain boundary properties, a plot is shown of the predicted grain boundary energy from molecular statics calculations as a function of the distance of the boundary from the deep cusp at the coherent twin boundary.

2.3. Approach

There are at least two generally accepted methods of describing a grain boundary in terms of its five macroscopic degrees of freedom [1]. One is to start with the three degrees of freedom representing the misorientation between the two grains, and then add two degrees of freedom to describe the orientation of the boundary plane. The second is to start with the boundary normals in each grain, two x two = four degrees of freedom, and add one to describe the "twist". Both of these methods of describing the grain boundary include degrees of freedom of two types. For the purpose of describing a boundary, there is nothing wrong with this, but having two distinct types of parameters is inconvenient in defining a distance. For example, it is standard to measure distance in misorientation space in terms of the angle of rotation or some function of it. And for two boundaries with identical misorientations, it should be possible to define the difference in the boundary plane orientation. But for two boundaries with different misorientations, what does it mean to have the same boundary plane orientation? Any well-defined reference orientation for the boundary plane is suitable for describing a boundary, but here we need for "the same boundary plane orientation" to mean that the boundaries are as close as they could be, given their respective misorientations. A. Morawiec [2] takes the approach of looking at the boundary normals in each crystal and creating a 4x4 matrix which includes the misorientation matrix, (9 entries) the boundary normal in each crystal (6 entries) and a zero; and then defining a distance based on the difference in misorientation between two boundaries and the difference in boundary normals, with the difference in boundary normals in each crystal weighted equally. This is a nice approach, but as discussed by Cahn and Taylor [3], it requires a choice of weighting of the misorientation contribution to the distance vs. the boundary normal contribution[1]. Since any weighting will produce an equally mathematically valid definition of distance, each worker is free to choose their own weighting. In some circumstances this might allow tuning the definition of distance to the particular problem, but it would be desirable to have an approach that does not require mixing apples and oranges at all.

It is therefore useful to consider a description in which all of the parameters are of the same type. First choose a fixed reference configuration for the crystal. For a cubic crystal, for example, one might choose the coordinate axes to be the cubic axes. We must ensure, of course, that our definition of distance between two boundaries is independent of our choice of the reference configuration. Now consider the grain boundary situated so that the boundary plane is the plane z=0. We can describe the grain with $z < 0$ by the rotation matrix A required to turn the reference configuration into the configuration of that grain. Similarly the grain with $z>0$ is described by a

[1] It should perhaps be pointed out that in their discussion of possible metrics on the five dimensional space of grain boundaries based on misorientation difference and boundary normal difference Cahn and Taylor do not mention the need to handle the boundary normal as defined in crystal A and as defined in crystal B symmetrically.

rotation matrix B. Thus the grain boundary is described by two parameters, both of which are rotation matrices. Each rotation provides three degrees of freedom, so one of these must be redundant. This is because a common rotation of both grains about the z-axis does not change the boundary, but does change the rotations matrices. This will be dealt with shortly.

2.4. Definition of the macroscopic crystallographic space of grain boundaries.

Consider an infinite planar grain boundary, and choose coordinates such that the boundary plane is the plane z=0. Call the grain where z<0 grain A, and the grain where z>0 grain B. There is an arbitrary choice as to which direction in the plane of the boundary to call the x-direction. For a homophase boundary the choice of which normal direction is caused positive z could also be considered arbitrary, but for the moment we will consider A-B and B-A to be different boundaries. We are concerned with only the five macroscopic degrees of freedom, so we ignore relative displacements of the lattice, relaxation, etc. Thus, for our purposes, grain A is completely determined by its lattice vectors, given in the sample reference frame we have specified. We now need a mathematical description of this boundary, and will follow Cahn and Taylor in referring to this as a parameterization [3]. To do this, we choose a reference crystal. (For a heterophase boundary, we would need to choose a reference crystal for each material.) For example, for an fcc material, we could choose the fcc lattice vectors specified in cubic coordinates as the reference crystal. The choice of the coordinate frame in the reference crystal is arbitrary, and the metric will not depend on it. There is now at least one rotation matrix **A** that takes the lattice vectors of the reference crystal to the lattice vectors of grain A. (For a crystal with an inversion symmetry we require this to be a proper rotation. For a crystal without an inversion symmetry, we can follow Morawiec in treating the enantiomorphic versions as different materials, or we could say that the space of grain boundaries breaks down into two disconnected regions. In that case some boundaries would be infinitely far apart.) Similarly there is a rotation matrix **B**which gives the lattice vectors of grain B. Thus by specifying two rotation matrices (**A**, **B**), we have fully parameterized the boundary. We will not need to further parameterize the rotation matrices, but keep in mind that each rotation matrix represents three degrees of freedom, so as it stands our parameterization of the boundary has six degrees of freedom. The extra degree of freedom can be seen as coming from the arbitrary choice of coordinates in the plane of the boundary. That is to say, a rotation of the whole sample space about the z-axis will not change the boundary, but will change the rotation matrices that describe it. Thus (**UA**, **UB**) represents the same boundary as (**A**, **B**), where **U** is any rotation about the z-axis. We write $(\mathbf{UA}, \mathbf{UB}) \equiv (\mathbf{A}, \mathbf{B})$. If the crystal has non-trivial rotation symmetries, then the rotation matrix A will represent the same grain as the rotation matrix **AT**, where **T** is any element of the point symmetry group of the crystal which is a proper rotation (hereafter "rotation symmetry")[2]. Thus we can write $(\mathbf{UAT}_1, \mathbf{UBT}_2) \equiv (\mathbf{A}, \mathbf{B})$, where U is any rotation about the z-axis in the sample frame, and $\mathbf{T}_1$ and $\mathbf{T}_2$ are any rotation symmetries of the crystal expressed in the reference frame. For the moment we take as our description (definition) of the macroscopic

[2] Some crystals have symmetries that cannot be factored into a rotation and a translation. Because relative translation of the two grains is considered a microscopic, rather than a macroscopic, degree of freedom the translation can be ignored. Thus for such a crystal one would need to include rotations which differ from an element in the point group in our group of rotation symmetries, along with the rotations that are actually in the point group.

crystallographic grain boundary space these equivalence classes of ordered-pairs of rotation matrices. Note that this parameterization depends on the choice of orientation of the reference crystal, although the metrics will not.

In fact I will consider a couple of different definitions. The above definition is the simplest, and is probably suitable when a grain A is specified in a polycrystal and one asks about its boundary with a neighboring grain B at a given point where a well defined boundary normal exists. In considering the properties of individual grain boundaries, the choice of grain A as primary is arbitrary, however. Suppose we rotate the whole bicrystal about the y-axis in the sample space. This would then be considered the same boundary, and we can modify the definition above to let $(\mathbf{ZA}, \mathbf{ZB}) \equiv (\mathbf{A}, \mathbf{B})$, where **Z** is a rotation of 180 degrees about the y-axis in the sample frame. (The choice of which axis in the boundary plane to specify here does not matter, because we already have $(\mathbf{UA}, \mathbf{UB}) \equiv (\mathbf{A}, \mathbf{B})$ for any rotation about the z-axis.) This also seems a reasonable definition of when two boundaries are the same. And as a practical matter, for purposes of investigating the properties of individual grain boundaries one can go even further. If we take the bicrystal and reflect it about the x-z plane in the sample space, we get a mirror image of the original boundary. While one would not want to call this "the same boundary", it clearly will have the same energy, free energy, mobility, etc. Thus for interpolating into a table of grain boundaries energies, for example, one could treat two boundaries as close if one were close to a mirror image of the other. In the examples below, which involve the energy of single boundaries, boundaries are treated as the same if they differ by either of these operations.

As defined above, when the rotations **A** and **B** are identical the two crystals are perfectly aligned, and so there is no grain boundary. And two such "grain boundaries" are considered the same only if they have crystallographically equivalent "boundary normals". While these "no boundaries" are not interesting in themselves, how they are handled in defining the mathematical space of grain boundaries is important because it affects how the distance between low angle grain boundaries are defined, as discussed by Cahn and Taylor [3]. In misorientation space, clearly all low angle boundaries are close together, but their boundary planes may be very different. The approach that will be taken here is to say that a low angle boundary with boundary planes, for example, near <111> is not necessarily close to a low angle boundary with boundary planes near <100>; but that is not the only possible approach. Morawiec defines a separate distance measurement to determine how close a boundary is to being the "no-boundary boundary" [2]. Cahn and Taylor describe a method for taking a metric such as Morawiec's general metric and adjusting it so that all small angle boundaries are close together [3]. They also discuss the possibility of excluding the "no-boundary boundary" from the space altogether. In that case some small angle boundaries are not close to each other. Cahn and Taylor do not offer an explicit opinion with regard to the choice between these treatments. The approach I will advocate is in some ways equivalent to excluding the "no-boundary boundary". Here there is a two-dimensional family of points in the five dimensional space which correspond to no-boundary. This corresponds to a literal treatment of the misorientation/boundary normal description of the five dimensional space. A boundary is "no-boundary" when the misorientation is zero. This still leaves two degrees of freedom to describe its boundary normal. Consider the following physical "argument" to motivate this approach. Suppose I wish to describe a grain boundary in sample coordinates as follows. First I pick the boundary plane in sample space. Then I specify the orientation of the grain on each side of it. If I choose the orientations to be the

same, I have described a hypothetical "no-boundary" in the material. But the plane I chose originally has a specific orientation in the uniform crystal, so there are different "no-boundaries" possible depending on their boundary normal. This does not in itself provide evidence that treating these "no-boundaries" as different is the better approach, but it does seem to provide some rationale for considering it. More importantly, do the "properties" of these "no-boundaries" differ? Clearly the no-boundary itself has no properties that depend on its boundary normal. What about boundaries which are very close to it? As a boundary approaches any no-boundary its energy approaches zero. However, there is some evidence suggesting that as a boundary approaches zero-misorientation the zero-misorientation limit of its mobility depends on the boundary normal of the no-boundary it is approaching [10]. If this is indeed the case, it would provide a strong motive for treating "different" no-boundaries as different.

2.5. Definition of the metrics

Consider two boundaries (A,B) and (C,D) with representations $(\mathbf{A},\mathbf{B})$ and $(\mathbf{C},\mathbf{D})$. We will define a trial distance between the two boundaries based on the representation, and define the distance between the boundaries as the minimum over all equivalent representations. The rotation matrix to turn grain A into grain C, expressed in the reference coordinates is $\mathbf{A}^{-1}\mathbf{C}$, and the rotation angle for any rotation matrix **F** satisfies $\cos(\alpha) = [\mathrm{Tr}(\mathbf{F}) - 1]/2$. Two measures of how far we had to rotate grain A to turn it into grain C will be considered, $\alpha = \mathrm{acos}(\mathrm{Tr}(\mathbf{A}^{-1}\mathbf{C}) - 1]/2)$, and $3 - \mathrm{Tr}(\mathbf{A}^{-1}\mathbf{C}) = 2[1 - \cos(\alpha)] = 4\sin^2(\alpha/2) \approx \alpha^2$ for small α. We take the trial distance to be either $d_{\mathrm{Angle}} = \sqrt{\alpha^2 + \beta^2}$ where $\beta = \mathrm{acos}(\mathrm{Tr}(\mathbf{B}^{-1}\mathbf{D}) - 1]/2)$, or $d = \sqrt{3 - \mathrm{Tr}(\mathbf{A}^{-1}\mathbf{C}) + 3 - \mathrm{Tr}(\mathbf{B}^{-1}\mathbf{D})}$ which are approximately equal when they are small. Because the metrics depend only on combinations of the form $\mathrm{Tr}(\mathbf{A}^{-1}\mathbf{C})$ they are independent of the choice of orientation of the reference crystal. One key feature of a useful definition of distance, and a requirement to meet the mathematical definition of a "metric" is the triangle inequality [11]. This simply states that the distance from a point A to a point C cannot be further than the distance from A to a third point B, plus the distance from B to C. That is to say, going from A to C via B could be the shortest distance, or it could be going out of one's way, but it cannot be shorter than the shortest route. That the trial distances for specific representations of three grain boundaries must satisfy the triangle inequality follows from the fact α and $2\sin(\alpha/2)$ are standard metrics on $SO(3)$, along with the Minkowski inequality [12]. (Other variations on the Minkowski inequality could of course be chosen in combining the individual values for the two rotations instead of $p = 2$ [3].) That the minimizations over the various representations of each grain boundary do not disturb the triangle inequality is shown in Appendix A.

2.6. Comments and comparisons

The minimizations of the trial distance over the rotation symmetries of the crystal are straightforward as they involve a finite set of trial distances. The minimization over the rotations about the z-axis requires a numeric minimization with respect to the rotation angle, as far as I can see, in the case of d_{Angle}. For $d = \sqrt{3 - \text{Tr}(A^{-1}C) + 3 - \text{Tr}(B^{-1}D)}$, however, the minimization can be done analytically as given in Appendix B. This makes its computation much quicker that the computation of d_{Angle}.

In comparing these metrics to Morawiec's metric [2], it is most useful to ignore the special distance he defines for small angle boundaries, and simply compare to his general metric as if he had treated no-boundaries with different boundary normal as different boundaries. References to Morawiec's metric below refer to the general metric.

These metrics and Morawiec's metric satisfy the condition that for every $\varepsilon > 0$ there exists $\delta > 0$ such that $d_1(x, y) < \delta$ implies $d_2(x, y) < \varepsilon$, where d_1 and d_2 are any two of the three metrics. This is shown in Appendix C. In particular, this implies that these metrics induce the same topology on the space of grain boundaries as Morawiec's does.

The (countable) set of CSL boundaries with rational boundary normals is dense in the space of grain boundaries under these metrics. This is shown in Appendix D. Thus, as is at least implicitly well known, any boundary can be approximated as closely as desired by a CSL boundary with a rational normal. Because these boundaries can be simulated in MD using periodic boundary conditions and without misfit strain, this is valuable.

2.7. Sample calculations

A primary motivation for defining a metric on the space of grain boundaries is to use it to study grain boundary properties. For example, assuming that grain boundary energy is a uniformly continuous function of macroscopic crystallography, then a table of grain boundary energies for an adequate finite set of grain boundaries can be used to predict the energy of any grain boundary to within some tolerance. Using a set of 388 grain boundaries, and their energies in Ni as predicted by an EAM potential [9, 13], figure 1 shows the difference in energy plotted against the distance d for all pairs of boundaries with d<1.0. As expected, the plot is consistent with the energy being a uniformly continuous function of the macroscopic crystallography. The red line described in the figure caption can be used to estimate how close two grain boundaries need to be to obtain an acceptable estimate of the energy for one from the other.

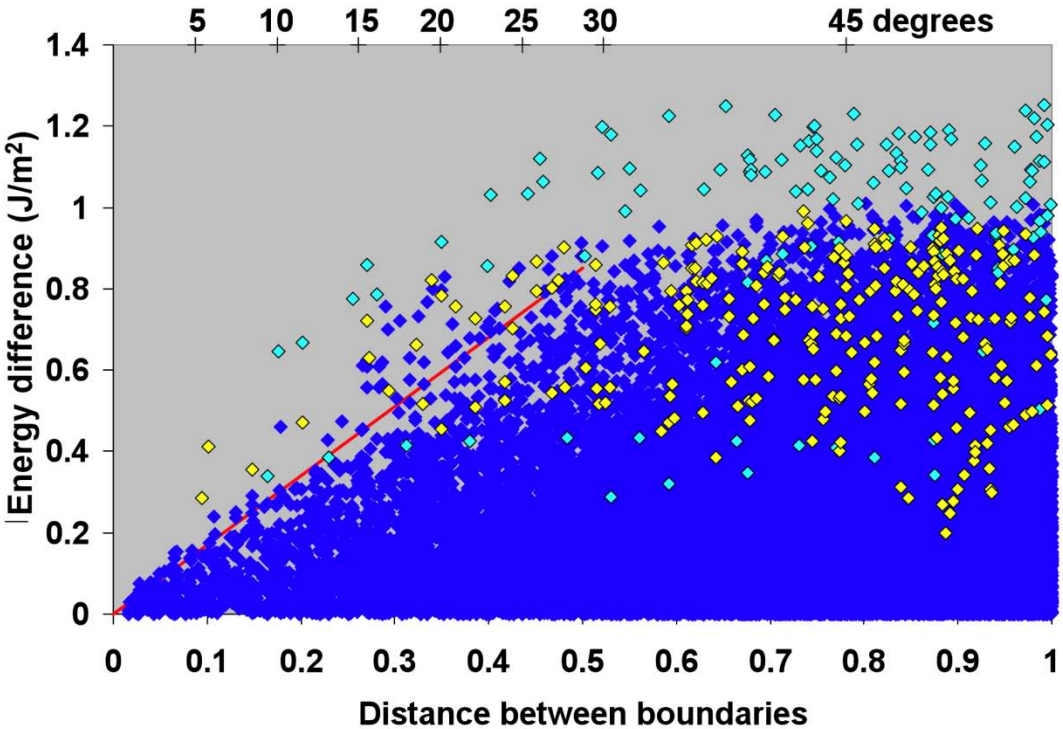

Figure 2-1. Energy difference as a function of crystallographic distance
The difference in energy between pairs of grain boundaries as a function of the crystallographic distance d between boundaries, based on 388 Ni boundaries. Only pairs separated by less than a distance of 1.0 are shown. The cyan points indicate that one of the two boundaries is the coherent twin, while the yellow points indicate that one of the two boundaries is the low energy Σ11. The red line is chosen to include 90% of the data points where the distance is less that 0.1, excluding boundary pairs containing either the coherent twin or the low energy Σ11 boundary) which are anomalously low in energy. Above the graph is shown a rough conversion of the distance to degrees, chosen so that for two pure twist boundaries about the same axis it is the difference in misorientation. (For small enough differences that rotational symmetries do not intervene.)

The metric can also be used to look at energy near a boundary which lies at a local minimum of the energy, such as the coherent twin boundary. Figure 2 shows the predicted energies of 425 Ni boundaries (including the 388 discussed above) as a function of the distance d from the coherent twin. The red symbols represent grain boundaries that have the same Σ3 misorientation as the coherent twin, but differ in that their boundary planes are no longer <111>. The slope of the cusp is lower for the Σ3 boundaries nearest the coherent twin than for the curve of <111> twist boundaries, indicated in green, which have different misorientations but the same boundary plane as the coherent twin. And another boundary can be seen close to the coherent twin that lies along a third direction in the five dimensional space along which the slope of the cusp is even higher.

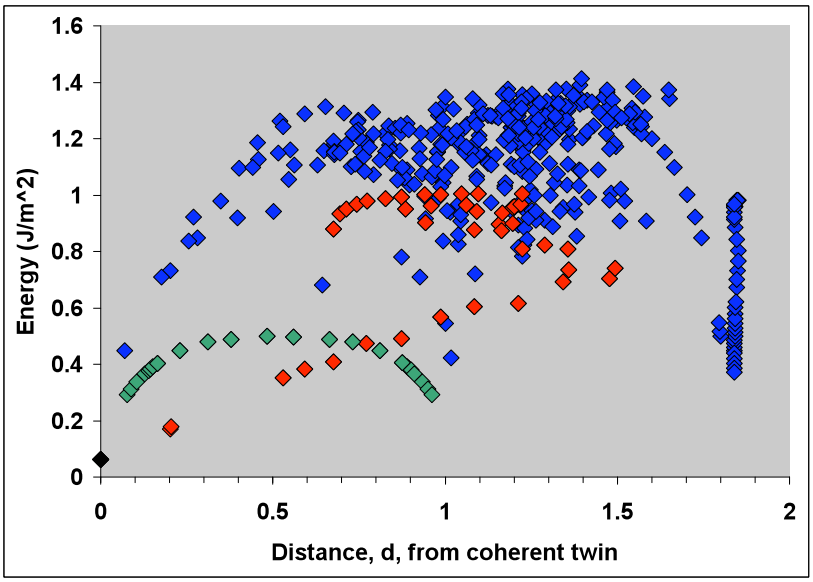

Figure 2-2. Energy of Ni boundaries by their distance from coherent twin
Energy of 425 Ni boundaries plotted by their crystallographic distance from the coherent twin. Red symbols indicate Σ3 boundaries. Green symbols indicate <111> twist boundaries. Black symbol indicates the coherent twin. Blue symbols indicate all other boundaries. The coherent twin represents a cusp in the grain boundary energy, however the rate of increase in energy as one moves away from it depends on the direction chosen in the five-dimensional space.

2.8. Conclusions

A new class of metrics for the five dimensional macroscopic crystallographic space of grain boundaries has been described. That space is defined in this work in terms of the two rotations that transform the upper (lower) grain of one boundary into the upper (lower) grain of the other boundary. Thus the space is defined as equivalence classes in SO(3) x SO(3). The space thus defined consists of the same points as when defined in terms of, for example, misorientation and boundary normal. In comparison with the metric developed by A. Morawiec, this approach avoids the issue of how to weight a difference in misorientation between the two boundaries and the difference in boundary normals. The two metrics described here, as well as the metric of Morawiec induce the same topology on the space of grain boundaries. It was shown that the CSL boundaries with rational boundary normals is dense in the grain boundary space under this topology.

2.9. Appendices

2.9.1. Appendix A

The metrics satisfy the triangle inequality. Consider three boundaries (A,B), (C,D) and (E,F). In computing $d((A,B),(C,D))$ some representation gave the minimum trial distance, say

$(\mathbf{OAT}_1, \mathbf{OBT}_2)$ and $(\mathbf{PCT_3}, \mathbf{PDT_4})$. In fact this can be simplified. The trial distance involves, for A and C, $\mathrm{Tr}((\mathbf{OAT_1})^{-1}\mathbf{PCT_3}) = \mathrm{Tr}(\mathbf{T_1}^{-1}\mathbf{A^{-1}O^{-1}PCT_3}) = \mathrm{Tr}(\mathbf{A^{-1}O^{-1}PCT_3T_1}^{-1}) = \mathrm{Tr}(\mathbf{A^{-1}O'CT}_1')$ where $\mathbf{O}' = \mathbf{O^{-1}P}$ is a rotation about the z axis, and $\mathbf{T}_1' = \mathbf{T_3T_1}^{-1}$ is a rotation symmetry. Thus, without loss of generality, we can assume that the representations that gave the minimum trial distance for d((A,B),(C,D)) were of the form $(\mathbf{A}, \mathbf{B})$ and $(\mathbf{OCT}_1, \mathbf{ODT}_2)$, and similarly for d((C,D),(E,F)) the chosen representation was $(\mathbf{C}, \mathbf{D})$ and $(\mathbf{PET}_3, \mathbf{PFT}_4)$. But the latter gives the same trial distance as the representation $(\mathbf{OCT}_1, \mathbf{ODT}_2)$ and $(\mathbf{OPET}_3\mathbf{T}_1, \mathbf{OPFT}_4\mathbf{T}_2)$. Thus we have

$$
\begin{aligned}
d((A,B),(E,F)) &\le d_{\text{trial}}(((\mathbf{A},\mathbf{B}),(\mathbf{OPET}_3\mathbf{T}_1,\mathbf{OPFT}_4\mathbf{T}_2)) \\
&\le d_{\text{trial}}((\mathbf{A},\mathbf{B}),(\mathbf{OCT}_1,\mathbf{ODT}_2)) + d_{\text{trial}}((\mathbf{OCT}_1,\mathbf{ODT}_2),(\mathbf{OPET}_3\mathbf{T}_1,\mathbf{OPFT}_4\mathbf{T}_2)) \\
&= d((A,B),(C,D)) + d((C,D),(E,F))
\end{aligned}
$$

for both of our metrics.

2.9.2. Appendix B

Analytical minimization of $\sqrt{3 - \mathrm{Tr}(\mathbf{A}^{-1}\mathbf{OC}) + 3 - \mathrm{Tr}(\mathbf{B}^{-1}\mathbf{OD})}$ with respect to the general rotation **O** about the z-axis. This is equivalent to minimizing $3 - \mathrm{Tr}(\mathbf{A}^{-1}\mathbf{OC}) + 3 - \mathrm{Tr}(\mathbf{B}^{-1}\mathbf{OD})$, which can be done as follows:

Taking **O** as

$$
\begin{bmatrix} \cos(\tau) & -\sin(\tau) & 0 \\ \sin(\tau) & \cos(\tau) & 0 \\ 0 & 0 & 1 \end{bmatrix},
$$

gives

$$
\mathrm{Tr}(\mathbf{A}^{-1}\mathbf{OC}) = F_1(\mathbf{A},\mathbf{C}) + \cos(\tau)F_2(\mathbf{A},\mathbf{C}) + \sin(\tau)F_3(\mathbf{A},\mathbf{C})
$$

where

$$
\begin{aligned}
F_1(\mathbf{A},\mathbf{C}) &= (A^{-1})_{i3}C_{3i} \\
F_2(\mathbf{A},\mathbf{C}) &= (A^{-1})_{i1}C_{1i} + (A^{-1})_{i2}C_{2i} \\
F_3(\mathbf{A},\mathbf{C}) &= (A^{-1})_{i2}C_{1i} - (A^{-1})_{i1}C_{2i}.
\end{aligned}
$$

Hence

$$
\begin{aligned}
3 - \mathrm{Tr}(\mathbf{A}^{-1}\mathbf{OC}) + 3 - \mathrm{Tr}(\mathbf{B}^{-1}\mathbf{OD}) = 6 &- [F_1(\mathbf{A},\mathbf{C}) + F_1(\mathbf{B},\mathbf{D})] \\
&- \cos(\tau)[F_2(\mathbf{A},\mathbf{C}) + F_2(\mathbf{B},\mathbf{D})] \\
&- \sin(\tau)[F_3(\mathbf{A},\mathbf{C}) + F_3(\mathbf{B},\mathbf{D})],
\end{aligned}
$$

and minimizing with respect to τ gives

$3 - \mathrm{Tr}(\mathbf{A}^{-1}\mathbf{O}_{\min}\mathbf{C}) + 3 - \mathrm{Tr}(\mathbf{B}^{-1}\mathbf{O}_{\min}\mathbf{D}) = a - \sqrt{b^2 + c^2}$,
where
$a = 6 - [F_1(\mathbf{A},\mathbf{C}) + F_1(\mathbf{B},\mathbf{D})]$
$b = F_2(\mathbf{A},\mathbf{C}) + F_2(\mathbf{B},\mathbf{D})$
$c = F_3(\mathbf{A},\mathbf{C}) + F_3(\mathbf{B},\mathbf{D})$.

2.9.3. Appendix C.

The metrics considered here, d_{Angle} and d, and Morawiec's metric[2], d_M satisfy the condition that for every $\varepsilon > 0$ there exists $\delta > 0$ such that $d_1(x,y) < \delta$ implies $d_2(x,y) < \varepsilon$, where d_1 and d_2 are any two of the three metrics.

I. For d_{Angle} and d this follows from the continuity of the arccosine.

II. $\forall \varepsilon > 0\, \exists \delta > 0 \ni d((A,B),(C,D)) < \delta$ implies $d_M((A,B),(C,D)) < \varepsilon$.
To show that $d_M((A,B),(C,D)) < \varepsilon$ we need to control $3 - \mathrm{Tr}((\mathbf{C}^{*-1}\mathbf{D}^*)^{-1}\mathbf{A}^{-1}\mathbf{B})$, $1 - \hat{\mathbf{m}}^* \cdot \hat{\mathbf{m}}$, and $1 - \hat{\mathbf{n}}^* \cdot \hat{\mathbf{n}}$, where $\mathbf{C}^* = \mathbf{C}\mathbf{T}_1$, $\mathbf{D}^* = \mathbf{D}\mathbf{T}_2$ for some rotation symmetry $\mathbf{T}_1, \mathbf{T}_2$ and $\hat{\mathbf{m}} = \mathbf{A}^{-1}\hat{\mathbf{e}}_3, \hat{\mathbf{n}} = \mathbf{B}^{-1}\hat{\mathbf{e}}_3, \hat{\mathbf{m}}^* = \mathbf{C}^{*-1}\hat{\mathbf{e}}_3, \hat{\mathbf{n}}^* = \mathbf{D}^{*-1}\hat{\mathbf{e}}_3$. Because $d((A,B),(C,D))$ is small, for some $\mathbf{O}$, T1, T2 $d_{\text{Trial}}((\mathbf{A},\mathbf{B}),(\mathbf{O}\mathbf{C}\mathbf{T}_1,\mathbf{O}\mathbf{D}\mathbf{T}_2))$ is small. Thus $\mathbf{A} \cong \mathbf{O}\mathbf{C}\mathbf{T}_1$, and $\mathbf{B} \cong \mathbf{O}\mathbf{D}\mathbf{T}_2$. This can be written $\mathbf{O}\mathbf{C}\mathbf{T}_1\mathbf{A}^{-1} \cong \mathbf{1}$, $\mathbf{B}(\mathbf{O}\mathbf{D}\mathbf{T}_2)^{-1} \cong \mathbf{1}$ and hence their product
$\mathbf{B}(\mathbf{O}\mathbf{D}\mathbf{T}_2)^{-1}\mathbf{O}\mathbf{C}\mathbf{T}_1\mathbf{A}^{-1} = \mathbf{B}\mathbf{T}_2^{-1}\mathbf{D}^{-1}\mathbf{C}\mathbf{T}_1\mathbf{A}^{-1} \cong \mathbf{1}$. Thus
$3 \cong \mathrm{Tr}(\mathbf{B}\mathbf{T}_2^{-1}\mathbf{D}^{-1}\mathbf{C}\mathbf{T}_1\mathbf{A}^{-1}) = \mathrm{Tr}(\mathbf{T}_2^{-1}\mathbf{D}^{-1}\mathbf{C}\mathbf{T}_1\mathbf{A}^{-1}\mathbf{B}) = \mathrm{Tr}((\mathbf{C}^{*-1}\mathbf{D}^*)^{-1}\mathbf{A}^{-1}\mathbf{B})$, where the cyclic property of the trace has been used. Because $\mathbf{O}$ is a rotation about the z-axis,
$\hat{\mathbf{m}}^* = \mathbf{C}^{*-1}\hat{\mathbf{e}}_3 = \mathbf{C}^{*-1}\mathbf{O}^{-1}\hat{\mathbf{e}}_3 = \mathbf{T}_1^{-1}\mathbf{C}^{-1}\mathbf{O}^{-1}\hat{\mathbf{e}}_3 \cong \mathbf{A}^{-1}\hat{\mathbf{e}}_3 = \hat{\mathbf{m}}$ and similarly $\hat{\mathbf{n}}^* \cong \hat{\mathbf{n}}$. Therefore
$1 \cong \hat{\mathbf{m}}^* \cdot \hat{\mathbf{m}}$ and $1 \cong \hat{\mathbf{n}}^* \cdot \hat{\mathbf{n}}$ as needed.

III. $\forall \varepsilon > 0\, \exists \delta > 0 \ni d_M((A,B),(C,D)) < \delta$ implies $d((A,B),(C,D)) < \varepsilon$.
This direction is slightly more complicated because of the need to determine the rotation $\mathbf{O}$ about the z-axis. Without loss of generality take $\mathbf{C} = \mathbf{C}^*$, and $\mathbf{D} = \mathbf{D}^*$. The misorientation matrices of the two boundaries are $\mathbf{M}_{AB} = \mathbf{A}^{-1}\mathbf{B}$, and $\mathbf{M}_{CD} = \mathbf{C}^{-1}\mathbf{D}$. From
[[$3 \cong \mathrm{Tr}(\mathbf{M}_{AB}^{-1}\mathbf{M}_{CD}) = \mathrm{Tr}(\mathbf{B}^{-1}\mathbf{A}\mathbf{C}^{-1}\mathbf{D}) = \mathrm{Tr}(\mathbf{D}\mathbf{B}^{-1}\mathbf{A}\mathbf{C}^{-1}) = \mathrm{Tr}(\mathbf{D}\mathbf{B}^{-1}(\mathbf{C}\mathbf{A}^{-1})^{-1})$]]
$3 \cong \mathrm{Tr}(\mathbf{M}_{AB}^{-1}\mathbf{M}_{CD}) = \mathrm{Tr}(\mathbf{B}^{-1}\mathbf{A}\mathbf{C}^{-1}\mathbf{D}) = \mathrm{Tr}(\mathbf{D}\mathbf{B}^{-1}\mathbf{A}\mathbf{C}^{-1}) = \mathrm{Tr}((\mathbf{B}\mathbf{D}^{-1})^{-1}\mathbf{A}\mathbf{C}^{-1})$ we have [[
$\mathbf{D}\mathbf{B}^{-1} \cong \mathbf{C}\mathbf{A}^{-1}$]]. $\mathbf{B}\mathbf{D}^{-1} \cong \mathbf{A}\mathbf{C}^{-1}$ We also have $1 \cong \hat{\mathbf{m}}^* \cdot \hat{\mathbf{m}} = (\mathbf{C}^{-1}\hat{\mathbf{e}}_3)\cdot(\mathbf{A}^{-1}\hat{\mathbf{e}}_3)$, so [[
$\mathbf{C}^{-1}\hat{\mathbf{e}}_3 \cong \mathbf{A}^{-1}\hat{\mathbf{e}}_3$, and $\mathbf{C}\mathbf{A}^{-1}\hat{\mathbf{e}}_3 \cong \hat{\mathbf{e}}_3$]] $\mathbf{C}^{-1}\hat{\mathbf{e}}_3 \cong \mathbf{A}^{-1}\hat{\mathbf{e}}_3$, and $\mathbf{A}\mathbf{C}^{-1}\hat{\mathbf{e}}_3 \cong \hat{\mathbf{e}}_3$. Thus $\mathbf{A}\mathbf{C}^{-1}$ is approximately a rotation about the z-axis, and what is needed is a rotation exactly about the z-axis approximately equal to it. Letting [[$\mathbf{F} = \mathbf{C}\mathbf{A}^{-1}$]] $\mathbf{F} = \mathbf{A}\mathbf{C}^{-1}$, consider $\mathbf{k} = \mathbf{F}\hat{\mathbf{e}}_1 - \hat{\mathbf{e}}_3(\mathbf{F}\hat{\mathbf{e}}_1 \cdot \hat{\mathbf{e}}_3)$, and

$\hat{\mathbf{k}} = \mathbf{k}/|\mathbf{k}|$. Because $\mathbf{F}\hat{\mathbf{e}}_3 \cdot \hat{\mathbf{e}}_3 \cong 1$, $\mathbf{F}\hat{\mathbf{e}}_1 \cdot \hat{\mathbf{e}}_3$ is small, $\hat{\mathbf{k}} \cong \mathbf{F}\hat{\mathbf{e}}_1$. Take $\mathbf{O}$ to be the rotation about the z-axis that takes $\hat{\mathbf{e}}_1$ to $\hat{\mathbf{k}}$. $\mathbf{O}\hat{\mathbf{e}}_3 = \hat{\mathbf{e}}_3 \cong \mathbf{F}\hat{\mathbf{e}}_3; \mathbf{O}\hat{\mathbf{e}}_1 = \hat{\mathbf{k}} \cong \mathbf{F}\hat{\mathbf{e}}_1$; and $\mathbf{O}\hat{\mathbf{e}}_2 = \mathbf{O}\hat{\mathbf{e}}_3 \times \mathbf{O}\hat{\mathbf{e}}_1 \cong \mathbf{F}\hat{\mathbf{e}}_2$. Thus [[$\mathbf{O} \cong \mathbf{C}\mathbf{A}^{-1} \cong \mathbf{D}\mathbf{B}^{-1}$]] $\mathbf{O} \cong \mathbf{A}\mathbf{C}^{-1} \cong \mathbf{B}\mathbf{D}^{-1}$.Hence $\mathbf{A} \cong \mathbf{OC}$, and $\mathbf{B} \cong \mathbf{OD}$ and $d_{\text{Trial}}((\mathbf{A},\mathbf{B}),(\mathbf{OC},\mathbf{OD}))$ as needed. The detailed estimations indicated by $\cong$ can all be worked out by writing the various rotation matrices in the form $\mathbf{R}_{ij} = \cos\alpha\delta_{ij} + (1-\cos\alpha)\rho_i\rho_j - \sin\alpha\varepsilon_{ijk}\rho_k$ where α is the rotation angle and ρ is the rotation axis taken as a unit vector, and computing.

2.9.4. Appendix D.

The set of CSL boundaries with rational boundary normals (CSL-RBN) is dense in the macroscopic crystallographic space of grain boundaries. By the result in appendix B, this will be true for all of the metrics under discussion if it is true for any one of them. I will show it using Morawiec's metric. Given any boundary (A,B) and any $\delta > 0$ we need to find a CSL-RBN boundary (A*,B*) with $d_M((A,B),(A^*,B^*)) < \delta$. Let $\hat{\rho}$ be the rotation axis of (A,B), expressed in the (fcc) reference coordinates and α the angle of rotation. We can choose a rational rotation axis $\hat{\sigma} = (h,k,l)/|(h,k,l)|$, where *h*, *k* and *l* are integers, such that each of the components of $\hat{\sigma}$ is as close as we need to $\hat{\rho}$. The key point is that there is an angle as close as we need to α, that gives a CSL misorientation. The angles that give CSL misorientations are those angles β where $\tan(\beta/2) = \frac{m}{n}(h^2+k^2+l^2)^{1/2}$ for any integers *m* and *n*. [1] This insures we can choose a β as close as we like to α. Now for the boundary normals. Let $\hat{\mathbf{m}}$ be the boundary normal in grain A, expressed in the reference coordinates. We can choose any rational boundary normal we wish in A*, and so can choose $\hat{\mathbf{m}}^*$ as close as needed to $\hat{\mathbf{m}}$. The boundary normal in grain B is $\hat{\mathbf{n}} = \mathbf{A}^{-1}\mathbf{B}\hat{\mathbf{m}}$ ($\mathbf{A}^{-1}\mathbf{B}$ is the misorientation matrix expressed in the reference coordinates.) The boundary normal in B*, $\hat{\mathbf{n}}^*$ is given in the same way.
To show that $d_M((A,B),(A^*,B^*)) < \delta$ we need to control $3 - \mathrm{Tr}((\mathbf{A}^{*-1}\mathbf{B}^*)^{-1}\mathbf{A}^{-1}\mathbf{B})$, $1 - \hat{\mathbf{m}}^* \cdot \hat{\mathbf{m}}$, and $1 - \hat{\mathbf{n}}^* \cdot \hat{\mathbf{n}}$. After writing $(\mathbf{A}^{-1}\mathbf{B})_{ij} = \cos\alpha\delta_{ij} + (1-\cos\alpha)\rho_i\rho_j - \sin\alpha\varepsilon_{ijk}\rho_k$ and similarly for $\mathbf{A}^{*-1}\mathbf{B}^*$; and computing the three values, straightforward estimation gives the desired result.

2.10. References

[1] Sutton A.P, Balluffi RW. Interfaces in Crystalline Materials, Clarendon Press, Oxford, 1995.
[2] Morawiec A..Symmetries of Grain Boundary Distributions, in Weiland H, Adams BL, Rollett A.D, editors. Proceedings of the Third International Conference on Grain Growth, , TMS, Warrendale, 1998, p. 509. Morawiec A.. Acta. Mater. 2000;48:3525.
[3] Cahn JW, Taylor JE. J. Mater. Sci. 2006;41:7669.
[4] Brandon DG. Acta Metall. 1966;14:1479.

[5] Janssens KJF, Olmsted D, Holm EA, Foiles SM, Plimpton SJ, Derlet PM. Nature Materials 2006;5:24.
[6] Saylor DM, Morawiec A, Rohrer GS. Acta Mater. 2003;51:3663.
[7] Saylor DM, Morawiec A, Rohrer GS. Acta Mater. 2003;51:3675.
[8] Randle V, Rohrer GS, Miller HM, Coleman M, Owen GT. Acta Mater. 2008;56:2363.
[9] Olmsted DL, Foiles SM, Holm EA. Survey of grain boundary properties in FCC metals: Grain boundary energy, submitted to Acta Mater.
[10] Olmsted DL, Holm EA, Foiles SM, Survey of grain boundary properties in FCC metals: Grain boundary mobility, in preparation.
[11] Kelly, JL. General Topology. Van Nostrand, Princeton, 1955. p118.
[12] Rudin, Walter. Real and Complex Analysis. McGraw-Hill, New York, 1966. pp.62-63.
[13] Foiles SM, Hoyt JJ. Acta Mater. 2006;54:3351.

3. Grain boundary interface roughening transition and its effect on grain boundary mobility for non-faceting boundaries

3.1. Abstract

Like other interfaces, equilibrium grain boundaries are smooth at low temperature and rough at high temperature; however, little attention has been paid to roughening except for faceting boundaries. Using molecular dynamics simulations of fcc Ni, we studied two closely related grain boundaries with different boundary planes. In spite of their similarity, their boundary roughening temperatures differ by several hundred degrees, and boundary mobility is much larger above the roughening temperature. This has important implications for microstructural development during metallurgical processes.

3.2. Introduction

Many engineered materials, including most metals and many ceramics and polymers, are polycrystalline; they are agglomerates of tiny, individual crystallites (grains), which are separated by internal interfaces (grain boundaries). Because grain boundaries contribute free energy to the system, there is a driving force for their removal. Thus, at high temperatures, grain boundaries move to decrease boundary area (e.g. via grain growth) or to eliminate high energy grains in favor of low energy grains. For example, grains with a magnetization vector parallel to an applied magnetic field are energetically preferred relative to those with magnetization orthogonal to the applied field; grains favorably aligned with a strain field are preferred relative to less favorably aligned grains. In both cases, given sufficient thermal energy the grain boundaries will move to eliminate the unfavored grains. The rate of grain boundary motion is governed by the boundary mobility.

Recent work has addressed the important issue of the dependence of the mobility of grain boundaries on their crystallography. Boundary crystallography is given by the angular misorientation of the neighbor grains (three degrees of freedom) and the boundary plane (two degrees of freedom)[1]. Since most experimental and computational investigations of grain boundary mobility study curved boundaries [2,3,4,5], they cannot characterize boundary plane effectsor determine the absolute mobility. A few studies have investigated motion of flat boundaries under applied magnetic or mechanical driving forces,[6,7,8] obtaining the absolute mobility as a function of misorientation and boundary plane; however, these studies are limited in the boundary structures and the materials that can be accessed.

For non-faceting boundaries, boundary motion is presumed to be an activated process, so the dependence of mobility on temperature is expected to be a simple Arrhenius function. It is well known that surfaces and interfaces, including grain boundaries, undergo a roughening transition

because of the competition between energy, which favors a smooth boundary, and entropy, which favors a rough one. While the behavior of a grain boundary will naturally differ between the smooth and rough states, this has typically been ignored, except in the case of faceting boundaries [1]. In this paper we show that, even for non-faceting boundaries, mobility is very different above and below the interface roughening transition. And since we also show that the roughening temperature itself can vary substantially with grain boundary crystallography, it is clear that the effect of roughness on grain boundary mobility requires more attention than it has received.

3.3. Approach and Results

In order to study the dependence of grain boundary mobility on temperature and crystallography conveniently, we must measure the absolute mobility of flat boundaries. To achieve this, we performed molecular dynamics (MD) simulations of flat boundaries moving under the synthetic driving force developed by K. G. F Jansenns et al.[9] This method uses a classical interatomic potential and adds a potential energy to each atom that depends on the location of its nearest neighbors. If the neighbor locations are exactly, or very close to, the favored crystal A, the added energy is zero. If the neighbor locations are exactly, or very close to, the unfavored crystal B, the added energy is a fixed amount *u*, which in this work varies in magnitude from 0.0025 eV to 0.05 eV per atom. For positive *u*, system energy decreases when atoms of crystal B are converted into the orientation of crystal A. This can be achieved by moving the boundary between B and A into crystal B (or by other mechanisms, such as crystal rotation, if the system allows). While this synthetic driving force does not arise from or represent a physical driving force, it is most similar to a magnetic driving force, which in appropriate cases it could mimic.

Results for two boundaries will be presented here. Both boundaries are ∑5 <001> tilt boundaries. One, which will be called boundary I, is an asymmetric boundary with boundary normals of <100> and <430>. The other, boundary II, is a symmetric boundary with <310> normals. For the results reported here, the simulation cells had periodic boundary conditions in the two directions lying within the grain boundary plane. At the ends parallel to the grain boundary they had free surfaces, so that there was a single grain boundary. The grain boundary was set up as a coincident site lattice boundary, and where atoms were within 1 Å of each other, one atom was removed; the system was subsequently relaxed before the driving force was applied. Mobility results shown below are generally based on eight simulations: four with positive and four with negative added potential energies; the average of all eight is shown. Simulation cell sizes varied from approximately 105 Å x 35 Å x 35 Å to 105 Å x 140 Å x140 Å, with about 70 Å available for boundary motion. Simulation times were chosen to make the total motion most of the available 70 Å. The simulations without driving force were run for 1 ns.

Whether and how mobility depends on the nature of the driving force is an open question in microstructural science[10]. It is especially pertinent to these simulations, which utilize a driving force that does not arise from a physical process. To investigate how the synthetic driving force compares with a physical driving force, we compared the motion of a boundary under the synthetic driving force to motion of the same boundary under an elastic driving force, as simulated by H. Zhang et al. [6]. Both simulations examine the same asymmetric Σ5 <100> tilt

boundary with <100> and <430> boundary normals (termed boundary I) using the Voter-Chen Embedded Atom Method (EAM) potential for Ni [11], the MD method, and similar simulation cells. As shown in Figure 1, in the limit of low driving force, the synthetic driving force and the elastic driving force yield the same mobility within statistical errors. Thus, boundary motion appears independent of the origin of the applied driving force, at least in this case, and the synthetic potential method gives physically relevant results.

At higher driving forces the synthetic driving force produces velocities that are closer to being linear in driving force than does the elastic driving force. As discussed in [6], the elastic driving force involves either a tensile or compressive stress, which gives an expected non-linearity at high driving forces. The synthetic driving force, which has no stress component, gives velocities that are approximately linear in driving force throughout the range studied. According to Sutton and Balluffi [1], typical stress induceddriving forces on grain boundaries are 10^{-5} to 10^{-4} GPa, well below even the smallest driving forces simulated. Thus we would expect agreement between the elastic and symthetic driving forces throughout the physically relevant range.

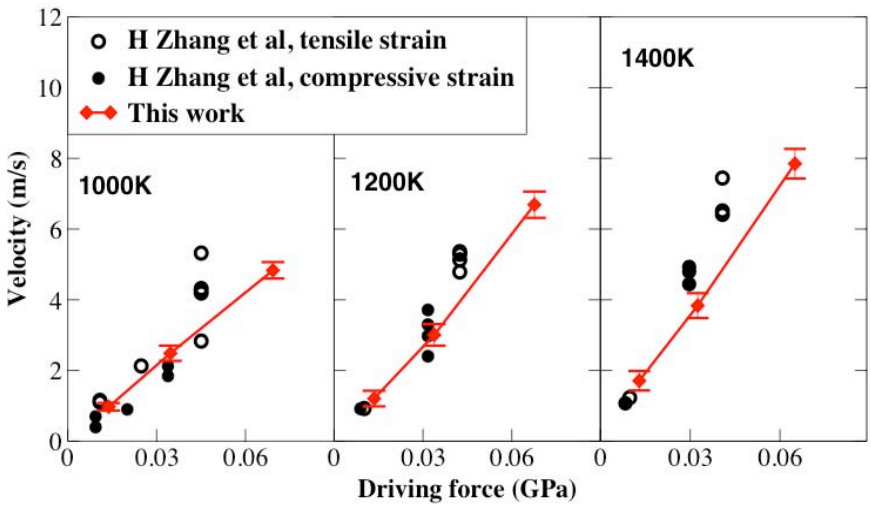

Figure 3-1. Velocity as a function of driving force
Velocity as a function of driving force: Ni (Voter-Chen), ∑5 <100> asymmetric tilt grain boundary with boundary normals <100><430>. In the limit of low driving force the results of the current, synthetic, driving force, and the elastic driving force of reference 6 are consistent.

One measure of boundary roughness is the standard deviation of boundary position. For periodic snapshots of our MD-generated boundaries, we measure the position of the interface in the direction normal to the interface relative to the average for that snapshot; this is often called the interface height function. Figure 1 shows the standard deviation of the interface height function averaged over all snapshots of boundary I. (Note that except for all results in Figure 1 are for the Foiles-Hoyt Ni EAM potential [12].) Roughness is a function of both temperature and simulation cell size. For the largest simulation cell shown, a roughening transition occurs in the neighborhood of 900K. At this temperature, the roughness becomes non-deterministic, with some simulation runs conforming to the higher temperature data, while others line up with lower temperature data. In smaller systems no clear indicator of the transition is apparent in the roughness metric. However, even at the smallest size studied, where the boundary is

approximately 35 Å by 35 Å, the results we show later exhibit a discontinuous change in the mobility at the roughening temperature.

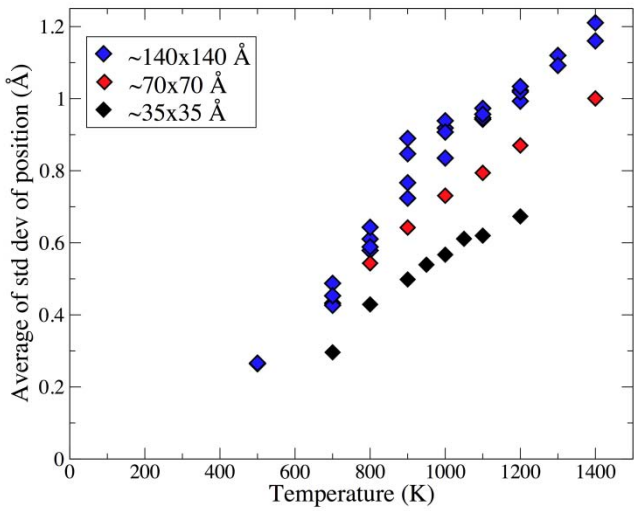

Figure 3-2. Roughness as a function of temperature

Roughness as a function of temperature: Ni (Foiles-Hoyt) Σ5 <100> asymmetric tilt grain boundary with boundary normals <100><430>.For the largest system size studied, a transition occurs at approximately 900K. At smaller sizes no transition is apparent. Identical symbols indicate different simulations under the same conditions.

While the key point in the current context is the existence of the transition and its temperature, notice that the spread of roughness values in Figure 2 at 900K suggests that the transition might be first order, with the potential for rough and smooth regions to coexist in the same boundary at the transition temperature. Although boundary roughening is often presumed second order, C. Rottman has suggested that long-range effective interactions between local boundary distortions can lead to a first order transition [13]. It would be interesting to perform hysteresis simulations to attempt to determine whether or not the transition is first order.

Figure 3 shows the absolute mobility (i.e. velocity divided by driving force) for boundary I as a function of temperature and driving force. Above the roughening temperature, the mobility is roughly independent of driving force and exhibits the expected Arrhenius behavior with an implied activation barrier of roughly 0.16 eV. Zhang et al. found an implied barrier of 0.26 +/- 0.08 eV for this boundary, but they included 800K data in the fit, which we believe is below the roughening transition and so should have different behavior.

Note that driving forces simulated are larger than almost all typical driving forces on real grain boundaries[1, page 524]. Thus the relevant results from our simulations are the low driving force limits of the simulation data.

For boundary I at 800K, which is below the roughening transition, Figure 3 shows that mobility decreases with driving force. Because MD is limited in the timescales it can achieve, we cannot observe very low mobilities, so we cannot measure a driving-force-independent limit for the mobility of the smooth boundary. However, we can conclude that the intrinsic mobility of the

smooth boundary is much smaller than that of the equivalent rough boundary. Moreover, this effect is not a simple Arrhenius dependence on temperature, but rather reflects a change in boundary motion mechanism as the boundary structure transforms from smooth to rough.

Evidence for this change in motion mechanism is captured in Figure 4, which shows spatial trajectories for the rough (1400K) and smooth (800K) boundaries. While the rough boundary moves continuously so that its position is linear in time, the smooth boundary moves in a stepwise manner, characterized by sudden motion events interspersed with static periods of varying duration. The step size is half the lattice parameter, as expected for motion of an atomic flat boundary of this orientation. Clearly, the rough and smooth boundaries move in fundamentally different manners.

Interestingly, at high driving force, the mobility of boundary I at 800K appears to become consistent with the mobility predicted by the activation barrier derived from the higher temperature data. This suggests that the mechanism of boundary motion has become indistinguishable from that of the rough boundaries. We conjecture that the 800K boundary has become "dynamically" roughened at high driving force, but have not attempted to measure the roughness of the moving boundaries directly.

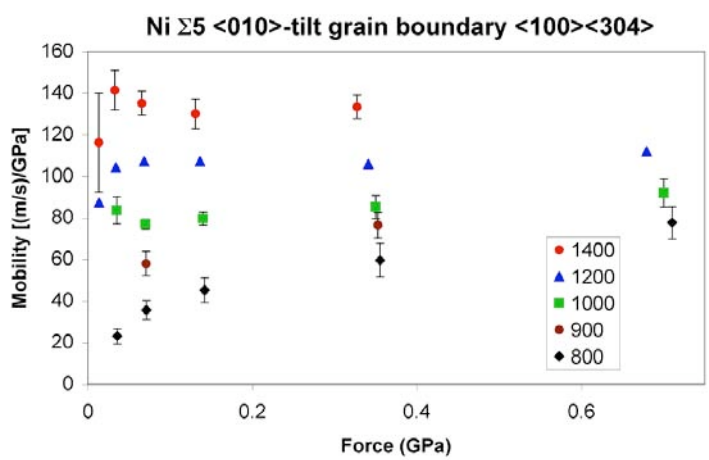

Figure 3-3. Mobility as a function of driving force

Mobility as a function of driving force: Ni (Foiles-Hoyt), ∑5 <100> asymmetric tilt grain boundary with boundary normals <100><430>.For temperatures of 1000K and above, the mobility is independent of the driving force within the range studied. For 800K, the mobility is similar to the high temperature mobility at very high driving force, but is substantially smaller at low driving force, and a low driving force limit is not reached at the lowest driving forces studied.

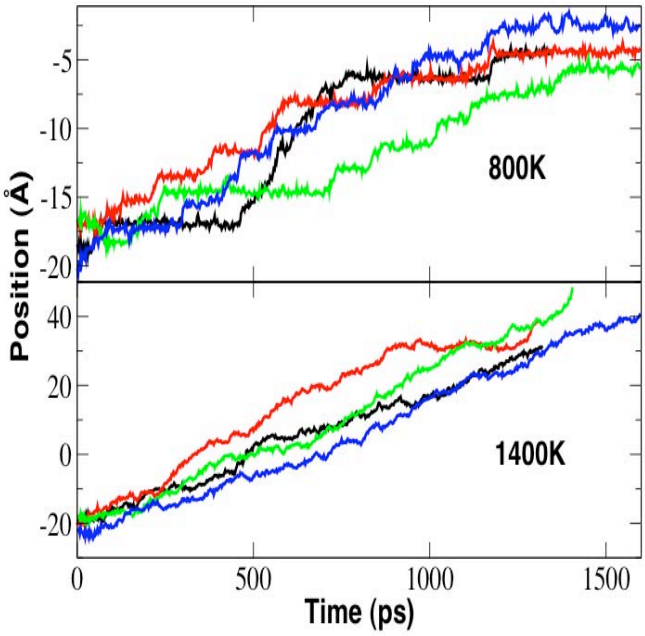

Figure 3-4. Motion of grain boundary I

Motion of grain boundary I at the smallest driving force at 800K and 1400K. At 1400K the boundary is rough and moves fairly continuously. At 800K the boundary is smooth and moves in distinct steps.

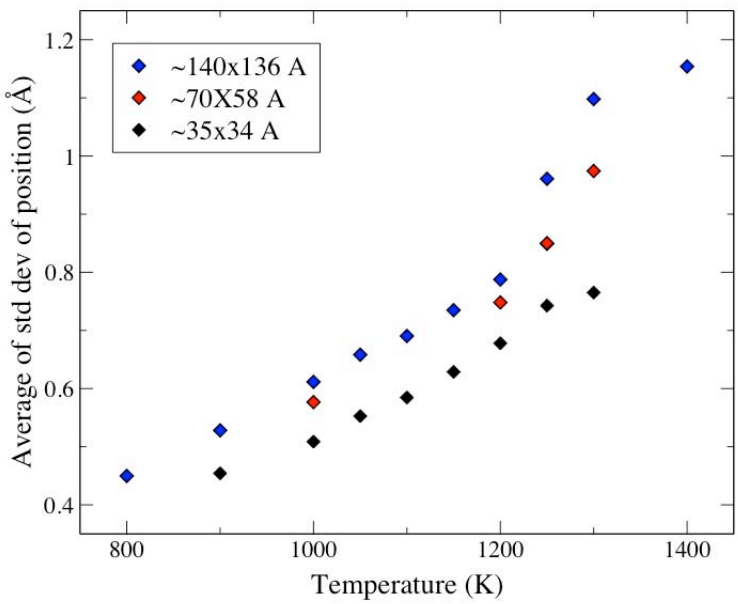

Figure 3-5. Roughness as a function of temperature
Roughness as a function of temperature: Ni (Foiles-Hoyt) Σ5 <100> symmetric tilt grain boundary with <310> boundary normals.For the two largest system sizes studied, a transition occurs at about 1250K.

Different behavior above and below the roughening transition has typically been studied only in faceting boundaries. However, boundary I is a general high angle boundary and should not exhibit faceting. We conclude that the difference in behavior between rough and smooth boundaries must be taken seriously for non-faceting boundaries as well. This is a primary conclusion of this paper.

Figure 5 and Figure 6 show the roughness and mobility of a symmetric Σ5 <100> tilt boundary with <310> boundary normals, which we will refer to as boundary II. This symmetric boundary is low energy, and boundaries vicinal to this one could show faceting, so it might be considered a faceting boundary in some sense. We do not observe any obvious faceting in these small systems, however.

For boundary II, Figure 5 shows a roughening transition near 1250K for the two larger system sizes studied.Notice the significant difference (~300K) in roughening temperature for boundaries I and II, which have the same misorientation and differ only in boundary plane. Because there is only one simulation for each parameter set, we cannot see “mixed” behavior at the transition temperature as we did for boundary I. Histograms of the data at the largest size suggest that the transition for boundary II is similar to that of boundary I, however.

The mobility of boundary II, shown in Figure 6, is qualitatively similar to that of boundary I.Above the roughening transition, mobility is independent of driving force and follows Arrhenius behavior. At 1000K, well below the roughening transition, mobility shows no

measurable lower limit as driving force decreases but at high driving force the smooth boundary approaches the high temperature mobility.Again it appears that there is a large discontinuity in mobility between smooth and rough boundaries that is mitigated at high driving forces.

We also have simulated the other symmetric Σ5 <100> tilt boundary, which has <210> boundary normals. Although we will not report on it here in detail, we should briefly mention that it shows additional behavior. This boundary appears to show a roughening transition around 1250K. Above and just below the roughening temperature it behaves qualitatively like the two boundaries discussed here. However, well below the roughening transition, from 500K to 1000K, boundary mobility increases as temperature decreases, indicating a barrier-free motion subject to damping that increases with increasing temperature. The increase in mobility is substantial enough that the 500K mobility is considerably higher than the 1400K mobility. This unexpected behavior appears to be related to a boundary motion mechanism involving shear [14,15], and will be discussed in another paper.

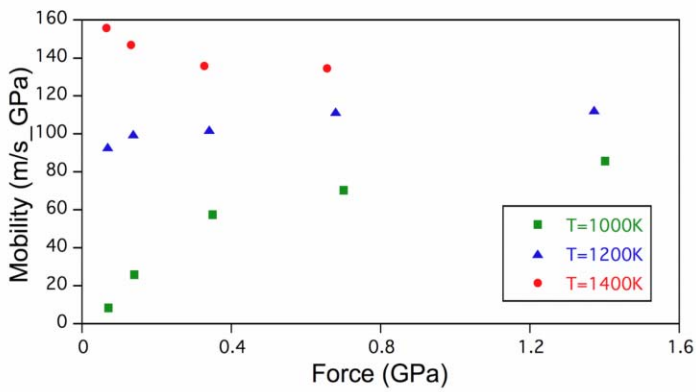

Figure 3-6. Mobility as a function of driving force
Mobility as a function of driving force: Ni (Foiles-Hoyt), Σ5 <100> symmetric tilt grain boundary with <310> boundary normals. For temperatures of 1200K and 1400K, the mobility is independent of the driving force within the range studied. At 1000K, the mobility is similar to the high temperature mobility at very high driving force, but is substantially smaller at low driving force, and a low driving force limit is not reached at the lowest driving forces studied.

3.4. Summary

In summary, we find that simulations of grain boundary mobility in Ni using synthetic and elastic driving forces give the same results. Thus, grain boundary mobility appears to be an intrinsic material property independent of driving force origin for these two driving forces.

A non-faceting, asymmetric Σ5 Ni grain boundary undergoes a roughening transition at 900K. Above the roughening temperature, boundary motion is continuous and mobility is high, independent of driving force, and Arrhenius in temperature. Below the roughening temperature, boundary motion is stepwise and mobility is low, decreasing with driving force, and non-Arrhenius. At high driving forces, the low temperature boundaries have mobilities consistent with rough boundary structures.

A symmetric Σ5 Ni grain boundaries exhibits similar behavior to the asymmetric boundary, but with a roughening temperature that differs from the asymmetric boundary by 300K.

Computational studies of grain boundary motion often give results for activation barriers and mobilities that fail to agree with experimental results. While this is often attributed to solute effects, our results imply that the boundary roughening transition is a likely source of differences as well.

The large change in mobility at the roughening transition may have major impacts on microstructural development in polycrystalline systems. Large differences in grain boundary mobility within a single microstructure can cause abnormal grain growth [16]. At a temperature where some boundaries are smooth and others are rough, such boundary mobility differences may exist and may substantially alter the course of microstructural evolution.

3.5. References

1. Sutton A. P. & Balluffi, R. W., Interfaces in Crystalline Materials. Clarendon Press, Oxford, 1995.
2. Upmanyu, M., Srolovitz, D. J., Shvindlerman, L. S. Gottstein, G., Acta Mater. 50 (2002) 1405.
3. Zhang, H., Upmanyu, M. & Srolovitz, D. J., Acta Mater. 53 (2005) 79.
4. Adams, B.L., Kinderlehrer, D., Mullins, W.W., Rollett, A.D. & Ta'asan, S., Scripta Mater. 38 (1998) 531.
5. Saylor, D. M., Morawiec, & A. Rohrer, G. S., Acta Mater. 51 (2003) 3675.
6. Zhang, H., Mendelev, M. I. Srolovitz, & D. J., Acta Mater. 52 (2004) 2569.
7. Huang, Y. & Humphreys, F. J., Acta Mater. 47(1999) 2259.
8. Winning, M., Gottstein, G. & Shvindlerman, L. S., Acta Mater. 50 (2002) 353.
9. Janssens, K. G. F. et al., Nature Mater. 5 (2006) 124.
10. Taheri, M. L, Molodov, D., Gottstein, G. & Rollett A. D., Z. Metallkd. 96 (2005) 1.
11. Voter A. F. & Chen S. P., Mater. Res. Soc. Symp. Proc. 82 (1987) 175.
12. Foiles, S. M. & Hoyt, J. J., Acta Mater. 54 (2006) 3351.
13. Rottman, C., Scripta Metall. 23 (1989) 1037.
14. Cahn, J. W., Mishin, Y. & Suzuki, A., Philos. Mag. 86 (2006) 3965.
15. Cahn, J. W. & Taylor, J. E., Acta Mater. 52 (2004) 4887.
16. Holm, E. A., Miodownik, M. A., & Rollett, A. D., Acta Mater. 51 (2003) 2701.

4. Survey of grain boundary properties in FCC metals: I. Grain boundary energy

4.1. Abstract:

The energies of a set of 388 distinct grain boundaries have been calculated based on embedded atom method interatomic potentials for Ni and Al. The boundaries considered are a complete catalog of the coincident-site-lattice boundaries constructible in a computational cell of a prescribed size. Correlations of the boundary energy with other boundary properties (disorientation angle, Σ value, excess boundary volume, and proximity of boundary normals to <111>) are examined. None of the usual geometric properties associated with grain boundary energy are found to be useful predictors for this data set. The data set is incorporated as supplemental material to facilitate the search for more complex correlations. The energies of corresponding boundaries in Ni and Al are compared and found to differ approximately by a scaling factor related to the Voigt average shear modulus or C_{44}. The correlation of the energy between boundaries that are crystallographically close is explored.

4.2. Introduction:

The grain-level microstructure of a metal influences a wide range of materials properties including strength, toughness, and corrosion resistance among others[1-3]. For that reason, understanding and controlling microstructural evolution is one of the central tasks of materials science. Since grain boundary properties, such as energy and mobility, play a key role in determining the growth of grains, there has been a long-standing interest in these topics. Recently, there has been a resurgence of interest in boundary properties due to the advent of microstructure modeling work that explicitly includes the variation of boundary properties with the boundary type[4-8]. These studies employ simple models for the variation in boundary properties with macroscopic boundary geometry and would benefit from a more complete description of the property variations. The theoretical challenge is the vast number of possible planar grain boundaries. Grain boundary crystallographic space is described by five macroscopic degrees of freedom[3]: three degrees of freedom define the relative rotation of the two neighboring grains and two more define the orientation of the boundary plane relative to the grains. Alternatively, one can describe a grain boundary in terms of the two surfaces that are joined at the boundary and a relative rotation around the boundary normal[9]. In that view, one needs two degrees of freedom to define each surface and a fifth degree of freedom to specify the rotation about the boundary normal. While there is some understanding of how boundary properties vary over special subsets of this 5-D space and while there has been a renewal of interest in the variation of grain boundary properties[10-17], the variation of boundary properties over the entire space is not yet fully understood. In this work, the energy of a large selection of boundaries is computed via atomic-scale simulations with the goal of providing a database for developing an understanding of the variation of grain boundary energy across the full 5-D space. Alternatively, the results could be used in an interpolative scheme to determine the energy of an arbitrary boundary. In a companion paper, the mobility of these boundaries have been computed[18] based on a recently developed synthetic driving force method[19].

There have been several previous computational studies[3, 16, 17, 20-25], of the structure and energy of grain boundaries as a function of subsets of the five macroscopic degrees of freedom for both fcc [21, 26-37] and bcc [38-40] metals. The studies for fcc metals considered grain boundaries on (111) and (100) planes [26, 30, 34], (110) and (113) planes [27], symmetric tilt boundaries [28, 31], asymmetric tilt boundaries [32, 41, 42], Σ3 boundaries [37] and general asymmetric boundaries for four choices of boundary normals [29]. These calculations have been reviewed in various places [23, 24, 33, 36, 43]. More recently, there have been experimental efforts to determine the relative free energies and the relative populations of grain boundaries geometries in aluminum [44-46], brass [47] and magnesia [48, 49].

There have also been various efforts to rationalize the variation of the grain boundary energy with the macroscopic degrees of freedom of grain boundaries. Sutton and Balluffi [23] critically examined the predictive power of various geometric criteria for low energy geometries compared to both experimental and computational data and found no support for the general usefulness of such criteria. The energy of low angle grain boundaries is predicted by a classic dislocation based model due to Read and Shockley[50]. Wolf demonstrated that the energies predicted by this approach can be extended to high-angle boundaries for the case of (111) and (100) twist boundaries and <111> and <100> symmetrical tilt boundaries [51]. Wolf and Philpot [52] proposed that grain boundaries formed along dense planes will have lower energies. They also noted a correlation between grain boundary energy and volume expansion of grain boundaries for the set of boundaries studied. Wolf [53] proposed, based on a series of simulations for symmetric and asymmetric tilt and twist boundaries, that the boundary energy variation can be rationalized in terms of the number of broken bonds in a manner similar to that for free surfaces. Wynblatt and coworkers proposed a more fully realized broken bond model for grain boundary energy[54, 55]. Recently, Tschopp and McDowell have suggested that the energy of asymmetric tilt boundaries can be modeled in terms of ideal faceting onto symmetric tilt boundaries[41]. The distribution of grain boundary geometries has been determined experimentally in commercially pure aluminum[45]. The results indicate that there is a higher population, and so presumed lower energy, for grains that terminate on low index planes with large interplanar spacing. In particular, boundaries terminated by (111) planes dominate the population and boundaries containing (113) planes also have a higher than random population.

The current work computes the energy of a large selection of grain boundary geometries for interatomic potentials that model Ni and Al. These energies are then used to examine various correlations between the energy and other boundary properties that have been suggested previously. In addition, the detailed boundary energy data is included as supplemental information to facilitate the use of this data to evaluate future proposed models, for comparison with experimental efforts to examine the variation of grain boundary energy and to provide data for interpolative approaches. The primary difference between the present work and the work mentioned above is the choice of the boundaries to be studied. The present study includes a wider range of more general boundaries in the set. In the above studies, particular types of boundaries, for example symmetric tilt boundaries, were chosen for study. In the present work, we consider all boundaries that can be constructed within a specified size limit as discussed below. While this set includes many of the boundaries included in earlier work, it also contains a large number of boundaries that have not been considered previously. A similar study of the properties of boundaries in two dimensional systems has been performed by Coffman and Sethna

[16]. Another difference between the current work and previous studies concerns the details of the energy minimization calculations. As discussed below, great care has been taken in the current work to determine optimal or near-optimal boundary structures and energies.

4.3. Computational Approach:

We wished to use atomistic simulations to study grain boundary properties throughout the five dimensional space of the macroscopic grain boundary parameters without arbitrarily considering preselected types of boundaries. To accomplish this, we considered all grain boundaries that can be constructed within a specified maximum cell size as described below. We chose to look at infinite planar boundaries, and so set up our system with periodic boundaries in the directions lying within the grain boundary plane. Taking the plane x = 0 as the nominal grain boundary plane, we thus have periodic boundary conditions in the y and z directions in both crystals. Both grains have the grain boundary as one surface in the x-direction. At the far surface in the x-direction are flat surfaces, with boundary conditions described below. This setup limits us to studying boundaries with coincident site lattice (CSL) misorientations[3], and rational boundary plane normals. Our approach to choosing a group of reasonably small boundaries, but without imposing other conditions, is to look at all boundaries that can be built in such a simulation cell where the periodic length of each grain along the principal axes of the simulation cell is no more than a maximum length, $L_{\max}$. Taking $L_{\max} = 15 a_0 / 2$, where a_0 is the lattice spacing, gives 388 distinct fcc boundaries, and these are the boundaries considered here. Note that we have treated mirror image boundaries as identical, since they must have identical properties.

All boundaries with CSL misorientation and rational boundary planenormals can be built in this configuration for large enough $L_{\max}$. While not all boundaries are precisely CSL boundaries, any non-CSL boundary, in a single material, can be approximated arbitrarily well by a CSL boundary[56]. Thus sampling the set of CSL boundaries should provide a good coverage of the space of possible boundary orientations while maintaining computational convenience. Some issues with the consideration of CSL boundaries have been discussed by Sutton[57]. CSL boundaries are often characterized by their Σ value which is the inverse density of coincident sites for that misorientation[3]. The largest Σ in this set of boundaries is 385; the smallest Σ *not* contained in this set of boundaries is 23. There are 72 distinct misorientations represented in the 388 boundaries. Some additional boundaries outside of this set were also considered, as discussed in the results section.

The grain boundary energies were predicted using molecular statics calculations based on embedded-atom method (EAM) potentials[58]. For Ni the Foiles-Hoyt[59] potential was used, and for Al the Ercolessi-Adams[60] potential. Both potentials reproduce the elastic moduli of the real materials. The Ni potential predicts stacking fault energy of 127 mJ/m^2 in good agreement with the experimental value of 125 mJ/m^2. The unstable stacking fault energy, which is related to dislocation nucleation, for this potential is 260 mJ/m^2 is good agreement with the value of 280 mJ/m^2 computed via density functional theory electronic structure calculations by van Schilfgaarde as reported by Zimmerman, *et. al.*[61]. The intrinsic and unstable stacking fault energies for the Al potential are somewhat below experiment values as discussed by Zimmerman *et.al.*[61].For each grain boundary, a large set of macroscopically equivalent initial

configurations was built and minimized using the conjugate-gradient method in the LAMMPS[62] code. The number of initial configurations depended on the grain boundary, with a simple boundary giving roughly 500 to 1000 configurations, and one of the most complex involving more than 50,000 minimizations. The details of the initial starting configuration are discussed below. While conjugate-gradient minimization of multiple starting configurations is not the most sophisticated approach to searching for the best energy minimum[63], its relative low cost is important to surveying large numbers of boundaries. The importance of examining multiple starting configurations has also been noted by Tschopp and McDowell[42].

The grain boundary energy calculations were done in a cell with periodic boundary conditions in the two directions in the plane of the boundary (y and z). The lengths of the cell in these directions were kept fixed at their lengths in the bulk perfect crystal. The cell contained one grain boundary, and had free surfaces in the direction normal to the boundary. A block of atoms at each surface was constrained to move as a single block, in order to avoid surface relaxation. This still permitted the blocks to move in the plane of the boundary to accommodate relative translation of the grains, and in the direction perpendicular to the boundary to accommodate volume expansion. The atoms in the constrained blocks were excluded from the energy calculation. The grain boundary energy was computed as the total energy of the free atoms, less the bulk energy per atom, divided by the area of the boundary.

The size of the cell was determined by the repeat structure of the grains making up the CSL boundary. We take x as the direction normal to the boundary. The y and z box lengths were the number of repeats required to give a length of at least 10 $a_0/2$ for the Ni boundaries, where a_0 is the lattice constant, or two repeats, whichever was larger. The length of each grain in the x-direction was the number of repeats required to give at least 40 $a_0/2$, or two repeats, whichever was larger. The Al boundaries were built in the same manner, except that the minimum box-length in the y and z directions was 17 $a_0/2$ (or two repeats if larger.)

To obtain an estimate of the optimal boundary energy, conjugate gradient minimizations were performed for a set of initial trial grain boundary structures. Construction of a set of initial trial grain boundary structures for a given bicrystal requires several considerations. For a specific choice of the orientations of crystal A and crystal B, translating one of the crystals relative to the other by the vectors in a primitive cell of the displacement shift complete (DSC) lattice yields the possible non-equivalent configurations of the interpenetrating crystal lattices. Having chosen a particular configuration, a grain boundary is formed by choosing a boundary plane (normal to the grain boundary normal) and discarding all A atoms to the right of the boundary and all B atoms to the left of the boundary. Different choices of where to locate the boundary give different configurations. Unlike the choice of the relative translation vector with the DSC primitive cell, however, only a finite number of non-equivalent choices exist. In particular, placing the boundary anywhere between two adjacent atomic planes gives the same configuration, and moving the grain boundary normal to the boundary plane by the distance between lattice planes in the CSL lattice gives identical configurations. After the grain boundary has been placed, some neighboring A and B atoms may end up too close together. Overlapping atoms must be resolved by removing one of the atoms from the system.

In this study, the initial configurations for each boundary were based on these three types of variations: the choice of offset vector between the two crystals, the placement of the boundary in the direction normal to the two crystals, and which overlapping atoms were discarded. Either 8 or 27 offset vectors were used, depending on the boundary. These were uniformly spread in three dimensions throughout a primitive cell of the DSC lattice[3]. For the simplest boundaries 27 offsets were used, while for most of the boundaries 8 were used. Each possible non-equivalent placement of the boundary plane in the normal direction was tried. Depending on the boundary and the offset vector this could vary from a single placement, to over 200 placements. Atoms that were closer than a (variable) cutoff to an atom in the other crystal were deleted by one of three methods. Atoms were either always deleted from crystal A; always deleted from crystal B; or both atoms were deleted and an atom inserted at their average position. The cutoff was varied from one-third of the nearest neighbor distance to 85% of the nearest neighbor separation in steps of 0.1 Å. In some cases, for example if the only atoms being deleted were exactly coincident, two or all three of the deletion methods produced the same starting configuration, so a few starting configurations for a given boundary may be identical. In summary, the initial configuration is a combination of the offset vector, the boundary placement in the normal direction, the deletion method, and the deletion cutoff. This process is similar to that used to examine the concept of multiplicity of grain boundary structures[35, 64]; however, the focus here is on finding a single, minimum energy structure rather than to examine the range of generated structures.

Figure 1 shows two examples of the results of the energy search. The energy after the conjugate gradient minimization is plotted for each of the starting configurations used, sorted by increasing energy. Panel (a) shows the results for a Σ111 boundary. About half of the configurations minimize to essentially the same energy, consistent with the possibility that this is the global minimum, at least for the cell size used. Some of the starting configurations minimized to significantly higher energies, demonstrating the need for the search. In particular note that for this case, if a single configuration was considered there is about a 50% chance that one would obtain an incorrect high energy and that the error in the energy could be over a factor of two. The importance of this observation has been demonstrated by recent studies of grain boundaries in silicon in which failure to consider alternative grain boundary structures lead to qualitatively incorrect conclusions about boundary properties[63, 65]. Panel (b) shows the results for an asymmetric Σ5 boundary with normals of <100><430>. In this case more than half of the configurations give essentially the same energy. However, a few configurations give slightly lower energies. This case suggests that even with the extensive sampling performed here, some boundary energies reported in this study may not be global minima. Fortunately, the behavior shown suggests that the errors in those cases are small. No search can guarantee to find true global minima, but we believe that the substantial care we have taken in this matter has produced results that are fully precise enough to support our conclusions.

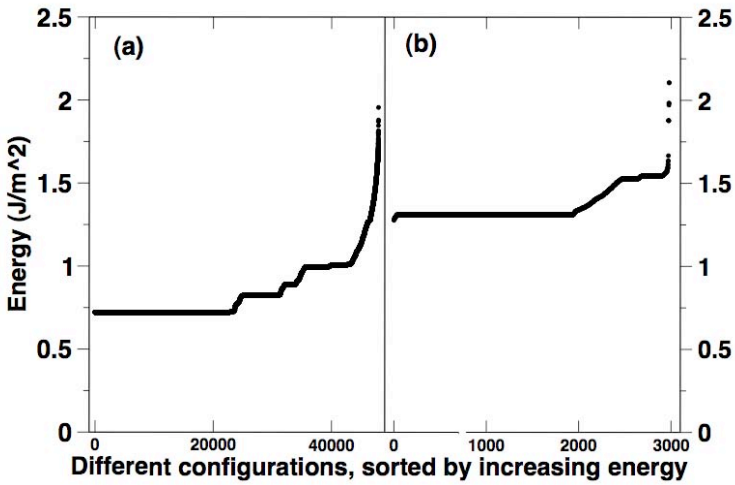

Figure 4-1. Minimized energy of set of initial structures
The minimized energy of the set of initial structures discussed in the text for (a) a Σ111 grain boundary and (b) a asymmetric Σ5 (100)/(430) grain boundary. The energies are sorted by increasing energy in the plot. Note that in (a) that about half of the initial structures yield the same, minimum, boundary energy while in (b) a small number of boundaries have energies somewhat below the most common energy.

4.4. Results

The computed energies for Ni grain boundaries are shown in Figure 2 as a function of the disorientation angle between the two grains. The corresponding plot for Al is similar. The disorientation angle is the minimum rotation angle in an axis-angle description of the rotation between the two crystals. It is computed by

$$\cos(\alpha) = \frac{Tr(\overleftrightarrow{R}) - 1}{2},$$

where $\overleftrightarrow{R}$ is the rotation matrix between the two grain orientations and the angle is minimized over the symmetry operations of the two crystals. Note that the disorientation angle is independent of the orientation of the grain boundary plane. The results shown are for the 388 boundaries described above plus some selected smaller angle boundaries and some boundaries closer to the coherent twin (plotted as triangles in Figure 2), selected to fill in gaps in the data set. (Note that these extra boundaries were studied using the same methods described above, but with a larger computational cell size to accommodate their larger repeat distances. In a few cases the search was more restricted than that described above.)

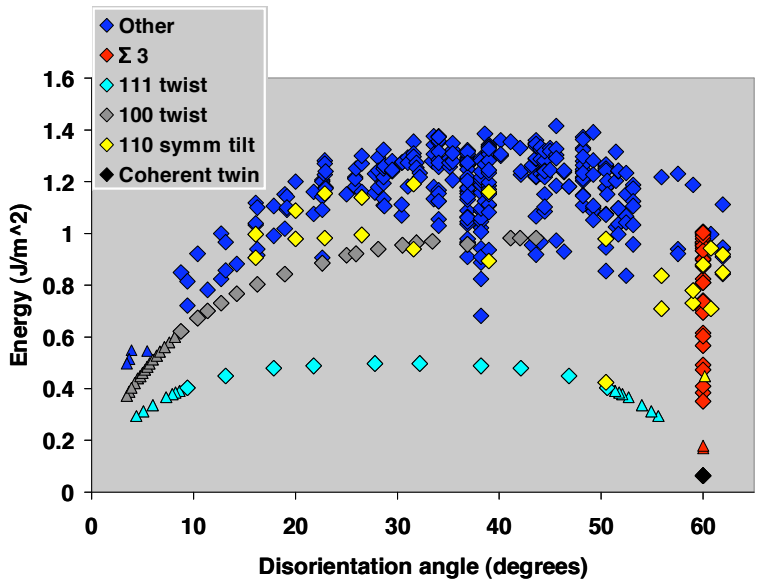

Figure 4-2. Grain boundary energy versus disorientation angle
The computed grain boundary energies for Ni plotted against the disorientation angle between the two grains. The red points correspond to Σ3 misorientations, the cyan points correspond to <111> twist grain boundaries, the grey symbols correspond to <100> twist grain boundaries, the yellow symbols correspond to <110> symmetric tilt grain boundaries and dark blue symbols correspond to all other boundaries. Triangles indicate data for boundaries outside the group of 388 boundaries defined by $L_{\max} = 15\,a_0/2$ as discussed in the text.

There are several features of note in these results. First, the lowest energy boundary shown is the coherent twin boundary [Σ3 60° (111)] as expected. While the coherent twin is a Σ3 boundary, it is important to note that there are forty-one Σ3 boundaries in this set which all have the same misorientation between the grains but different boundary planes. The energy of these Σ3 boundaries in the Ni simulations range from the coherent twin with an energy of ~0.06 J/m^2 to a high energy of about 1.0 J/m^2. This clearly demonstrates that the boundary plane has a crucial impact on the boundary properties. The variation of energy for Σ3 boundaries has been discussed previously based on experimental and computational data for Cu [37]. A similar conclusion about the importance of the boundary plane has been reached by Randle[66] based on analysis of polycrystal data. Clearly disorientation angle alone is not sufficient to determine boundary energy.

The <111> twist boundaries (plotted in cyan in Figure 2) are low in energy across the range of disorientation angles. The variation in energy of these boundaries is qualitatively consistent with the Read-Shockley[50] dislocation model which predicts that boundary energy is proportional to $\theta - \theta \ln \theta$, where θ is the disorientation angle. The <100> twist boundaries (plotted in grey in Figure 2) are also low in energy and qualitatively consistent with the Read-Shockley model.

Note that there is a lone boundary whose energy is close to that of the low energy (111) twist boundaries. This is the Σ11 50.48° <110> symmetric tilt boundary that has boundary plane normals of {113}. The relatively low energy of this boundary had been observed earlier by Hasson[21]. This boundary, along with the other <110> symmetric tilt boundaries, is plotted in

yellow. Note that the energies of the other <110> symmetric tilt boundaries do not stand out in this plot.

The energies plotted in blue correspond to boundary geometries not mentioned above. For all the boundaries, the energy appears to approach zero as the disorientation decreases, as expected. Note also that the general trends in the energy conform to the Read-Shockley model. However, higher disorientation angle boundaries (often referred to as general boundaries) show a significant spread in energy. The current results show that while the high angle boundaries have similar energies, about 1.2 J/m2 in this case, general boundary energy varies between about 0.8 and 1.4 J/m2. This degree of variation is sufficient to noticeably alter the microstructure of polycrystals from the familiar equiaxed, triconnected 'normal' grain structure. For example, triple junction angles will differ from 120°, and four-grain junctions may be stable[67]. Thus, general grain boundary energy cannot be treated as a single-valued parameter.

Historically, there has been speculation that the energy of a grain boundary can be interpreted in terms of its Σ value, which is the inverse of the density of coincident sites of the abutting grain lattices. The argument is that a small value of Σ (high density of coincident sites) suggests the lattices mesh together well and so the boundary energy would be lower. To examine this idea, boundary energy in Ni is plotted as a function of Σ in Figure 3. Note that there is not an apparent trend of the energy with Σ with the exception of the low energy of the coherent twin boundary. In particular, Σ5 and Σ9 misorientations have boundary energies that are not unusually small. The other important observation is that there is a wide variation in boundary energy for any given value of Σ. Recall that the Σ value derives from the relative orientation of the two grains, but does not depend on the orientation of the boundary plane. This large spread of the energy of boundaries with the same relative orientation again reflects the significant role that boundary plane orientation plays in grain boundary energy.

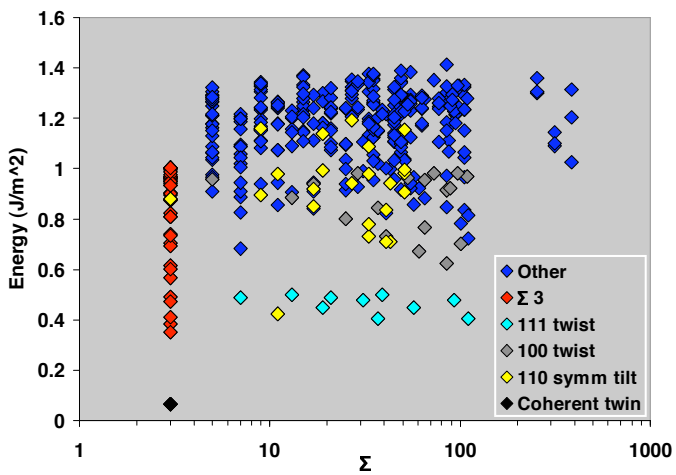

Figure 4-3. Grain boundary energy versus inverse density of coincident sites
The computed grain boundary energies for Ni plotted against Σ, the inverse density of coincident sites. The symbols are the same as in Figure 2.

Another correlation that has been discussed historically is that the grain boundary energy should vary with the net expansion of the grain boundary[26, 68, 69]. This idea is examined in Figure 4 where the grain boundary energy is plotted as a function of the excess volume per unit area (i.e. net expansion) of the boundary. The results indicate that there is a rough correlation between the grain boundary energy and the boundary expansion. The coherent twin boundary has both a very low energy and very small expansion. The other boundaries lie in a region which trends upward in energy with increasing expansion. Unfortunately, while there is an overall trend of increasing boundary energy with increasing boundary expansion, there is substantial variation about that trend such that one could not reliably predict the boundary energy based on the expansion. Further, just as there is no general expression for the grain boundary energy in terms of the macroscopic degrees of freedom, there is also no such relationship for boundary expansion.

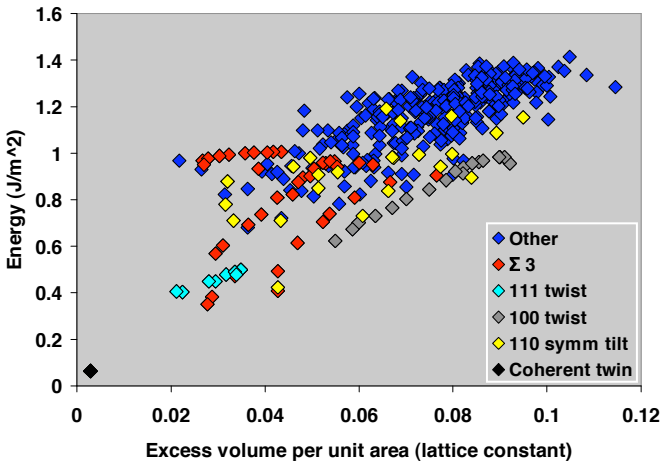

Figure 4-4. Grain boundary energy versus excess volume
The computed grain boundary energies for Ni plotted against the excess volume per unit area of the boundary in units of the lattice constant. The symbols are the same as in Figure 2.

It has been suggested that grain boundaries whose normals are close to (111) in either lattice are low in energy[45-47, 70]. This is consistent with the observation discussed above that the (111) twist boundaries form a low energy series in Figure 2. This idea has been challenged by Tschopp and McDowell [41].In order to test this assertion more generally, we define a parameter 1 – cos(a) + 1 – cos(b), where a and b are the angles between the boundary normals and the nearest <111> direction. If both normals are (111) the parameter is zero and it increases the further the normals deviate from <111> directions. Grain boundary energy is plotted with respect to this parameter in Figure 5. Overall, this does not appear to form a useful sorting of the boundaries either for low- or high-energy boundaries. It should be noted, though, that the density of points in our sampling of the five-dimensional grain boundary space does not examine the set of boundaries with boundary planes vicinal to (111). The closest normal to (111) represented in the set is (655) which is five degrees from <111>.

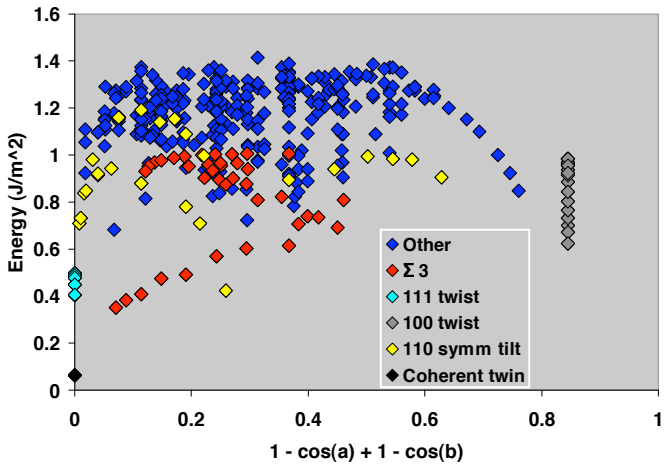

Figure 4-5. Grain boundary energy versus angle to <111> direction
The computed grain boundary energy for Ni plotted against 1 - cos(a) + 1 - cos(b), where a and b are the angles between the two boundary normals and the nearest <111> direction, which measures the deviation of the two boundary normals from (111). The symbols are the same as in Figure 2.

The fact that grain boundary energy cannot be predicted by a simple scalar parameter such as the disorientation or Σ value is not surprising and has been concluded previously [23]. Grain boundaries exist in a five dimensional, nonlinear space, where two boundaries that share one macroscopic descriptor may differ greatly in microscopic structure. That is not to say that grain boundary energy is not predictable. In fact, grain boundaries that are crystallographically close to one another are expected to have similar properties. This can be understood in the context of structural unit models [33]. The interesting and practically important question is how quickly do boundary properties vary with the crystallography. To address this issue, one needs a metric for crystallographic proximity that improves upon more traditional approaches [71, 72]. One of us has derived such a metric [56], which is described briefly in appendix A. Figure 6 shows the difference in energy between pairs of boundaries as a function of their crystallographic separation distance. Boundaries that are crystallographically close have similar energies as expected. Boundary pairs in which one boundary is of anomalously low energy (i.e. the coherent twin and the low energy Σ11) have a larger energy difference than typical boundary pairs. This is at odds with the commonly used Brandon criterion[73], which posits that boundaries that are crystallographically close to low energy boundaries (~ 15° $\Sigma^{-1/2}$) are also low in energy. The present results suggest that the low-energy region of crystallographic space near a low energy boundary is smaller than suggested by the Brandon criteria, and there does not appear to be any support for the variation of the size of the low energy region with Σ value.

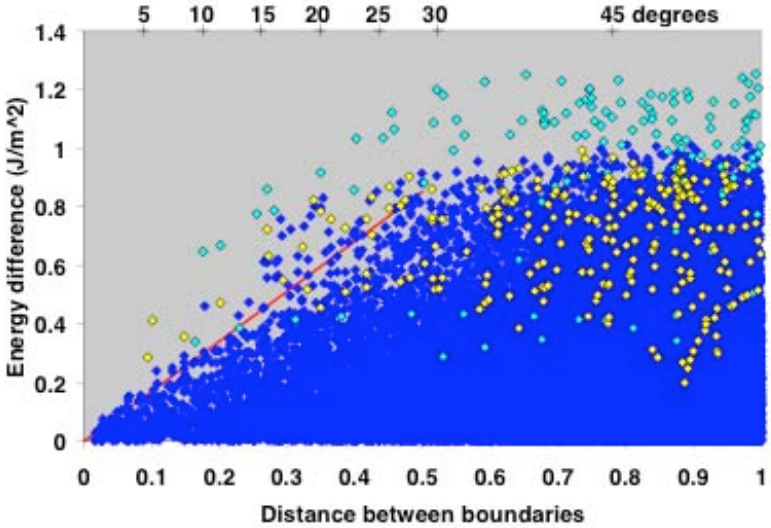

Figure 4-6. Energy difference of grain boundary pairs
The difference in energy between all pairs of grain boundaries as a function of the crystallographic distance between boundaries for boundaries separated by a distance of less than 1.0. The cyan points indicate that one of the two boundaries is the coherent twin. The yellow points indicate that one of the two boundaries is the low energy Σ11. The red line is chosen to include 90% of the data points where the distance is less than 0.1 excluding pairs where one of the boundaries is the coherent twin or the low energy Σ11. Above the graph is shown a rough conversion of the distance to degrees as described in Appendix A.

The energy difference between nearby boundaries (discounting pairs that include an anomalously low energy boundary) is largely bounded by a line proportional to the separation distance for small separations. This suggests that one can estimate the energy of a grain boundary from the measured energy of a nearby boundary. Many interpolation schemes can be envisioned; one simple one is to model the unknown boundary energy as the crystallographically nearest known energy, with an uncertainty given by the upper bound in Figure 6. Thus, a data set such as this one enables prediction of the energies of arbitrary boundaries; the accuracy of the predicted energy increases with the number of measured boundary energies in the data set. The present results provide insight into the accuracy of such interpolations given the separation of points in the data set.

An important question about grain boundary properties is the degree to which boundaries with the same macroscopic geometrical degrees of freedom in different materials have related properties. In Figure 7, the energies of the grain boundaries computed in Ni are plotted against the energies of the boundaries computed in Al for the same macroscopic degrees of freedom. Note that while the macroscopic degrees of freedom are the same, the microscopic structure need not be the same; each boundary structure is optimized separately in each material. For most boundaries, especially at moderate to high energies, the energies computed in Ni and Al are approximately proportional to each other. This suggests that, apart from a material dependent scaling factor, the energy of boundaries in different fcc metals will have about the same variation with the macroscopic geometrical degrees of freedom. While this result is generally assumed, this is the first direct confirmation of that assumption. There are some notable exceptions to this

for the low energy boundaries. The coherent twin boundary energy, while small in both materials, does not fall on this line. Instead, it is relatively lower in energy in Ni than in Al, in proportion to the stacking fault energy of each material. Similarly, the <111> twist boundaries and the lower energy Σ3 boundaries are relatively lower in energy in Ni. The low energy symmetric Σ11 boundary deviates in the opposite direction; it is relatively lower in energy in Al than in Ni. These results therefore suggest that general boundaries obey this scaling relation but that certain low energy boundaries do not.

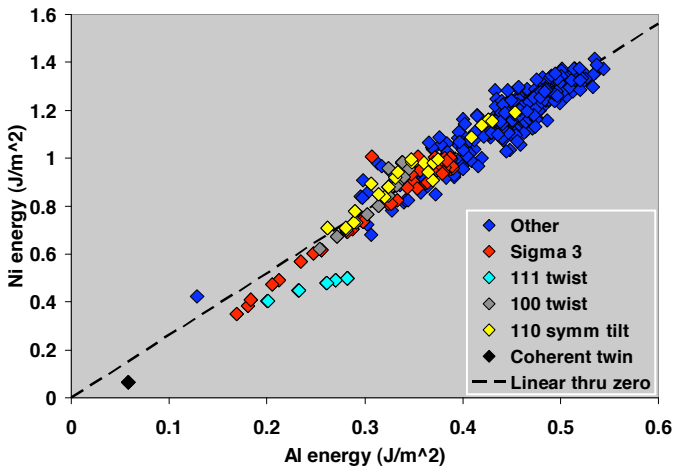

Figure 4-7. Comparison of the grain boundary energy of Ni and Al
Scatter plot of the computed grain boundary energies for Ni and Al. Each point represents the same macroscopic degrees of freedom though the microscopic structures may differ in some cases. The line indicates a by-hand linear fit constrained to pass through the origin to the data. The symbols are the same as in Figure 2.

It is interesting to explore how the ratio of the grain boundary energies observed for Ni and Al relates to the ratio of simple materials properties of these metals. Table 1 shows the ratio of the melting temperatures, sublimation energy (cohesive energy), vacancy formation energy, stacking fault energy, low index surface energies, bulk modulus and shear moduli. In all cases, the values are multiplied by the required power of the lattice constant to obtain quantities that have the same dimensions as the grain boundary energy, energy per length squared. Also, the results in Table 1 are based on the material property values obtained with the potentials used in the current study. The ratio of the Ni and Al grain boundary energies that best fits the computed values in Figure 7 is 2.6. An obvious possible scaling is that the boundary energies scale with the cohesive energy, which sets the energy scale of the interatomic interactions, divided by the square of the lattice constant. This predicts a ratio of 1.7, which is clearly inconsistent with the data. This demonstrates that the ratio of grain boundary energies in different materials reflects other aspects of the interatomic interaction. Certain other of the materials properties listed also do not provide reasonable estimates of this ratio; in particular the vacancy formation energy, stacking fault energy and bulk modulus do not predict a reasonable scaling. The melting temperature predicts a ratio somewhat below the observed one. It has been suggested that surface energies and grain boundary energies should be related. The low index surface energies predict a ratio of 2.2 – 2.3 which is reasonably close to the ratio of the grain boundary energies.

The best correlation is with two shear moduli: the ratio of the Voigt average shear modulus, which gives a ratio of 2.4, or C_{44}, which gives a ratio of 2.8. The relationship between a shear modulus and the grain boundary energy can be rationalized by a simple physical argument. Grain boundaries can be described as arrays of dislocations[3]. The elastic energy associated with a dislocation is proportional to the shear modulus[74]. Thus a direct relationship between the shear modulus and the grain boundary energy is plausible. Ni and Al have substantially different elastic anisotropies, so the ratio of shear moduli is not unique. Table 1 lists ratios predicted by the two extreme values of the shear modulus, $C' = (C_{11} - C_{12})/2$ and C_{44}, as well as the Voigt average, which falls in between. C' does not provide a good prediction of the relative energies.Udler and Seidman[75] proposed based on calculations of five boundaries for 7 metals, that the relative energies of grain boundaries should be linearly correlated with C_{44}. The agreement with the Voigt average shear modulus may be coincidental. The energies of boundaries need to be considered in more metals before a definitive statement can be made about which, if any, materials parameters predict relative grain boundary energy.

Table 4-1. Ratios of Ni and Al material properties

Property	Ratio
$k_B T_M/a_0^2$	2.2
E_{sub}/a_0^2	1.7
E_v^f/a_0^2	3.3
γ_{sf}	1.2
$\gamma_{(100)}$	2.2
$\gamma_{(110)}$	2.3
$\gamma_{(111)}$	2.2
Ba_0	1.9
$C' a_0$	1.6
$C_{44} a_0$	2.8
$\mu_{voight} a_0$	2.4

The ratio of selected materials properties calculated for Ni and Al using the present interatomic potentials. The various properties are scaled by a power of the lattice constant, if needed, to obtain quantities with dimensions of energy/area. The properties listed are the melting temperature, sublimation energy, vacancy formation energy, stacking fault energy, free surface energies for (100), (110) and (111) faces, bulk modulus, the two extreme shear moduli and the Voigt average shear modulus.

4.5. Summary

We have computed the energies of a large set of grain boundaries using an embedded atom method potential for Ni and Al. This work differs from previous computational surveys of grain boundary energy in two ways. First, a more extensive search for the optimum boundary structure has been performed. Second, a broader range of boundaries, comprised of all coincident-site-lattice boundaries that can be constructed within a prescribed computational cell

size, has been considered. While this set includes some boundaries studied previously, it also includes many boundaries of a more general character than have been considered in prior studies.

Our survey provides the following observations:

1. Disorientation angle by itself is insufficient to determine the boundary energy. The energy of general grain boundaries varies widely, though the boundary energy does tend to zero for small disorientations as expected.
2. Boundaries with the same disorientation angle but different boundary planes may have substantially different energies, as typified by the Σ3 boundaries; thus, boundary plane plays a critical role in the determination of boundary energy.
3. <111> twist and <100> twist boundaries are systematically low in energy and follow the Read-Shockley model for grain boundary energy. The Σ11 50.48° <110>/{113} symmetric tilt boundary is also of low energy.
4. Grain boundary energy does not correlate with Σ value, and there is a wide variation in energy for the same Σ value.
5. There is a rough correlation between the grain boundary energy and the net expansion (i.e. free volume) of the boundary. Boundaries with smaller net expansions tend to have smaller boundary energies; however, this correlation is not sufficiently strong to predict energy from expansion.
6. While boundaries with perfect (111) normals were low in energy, for the other boundaries there was not a clear relationship between energy and the deviation of the boundary normals from (111). This may reflect the fact that the current set does not contain boundaries with boundary planes vicinal to (111).
7. Boundaries that are close to one another in crystallographic space have similar energies, with the upper bound on energy difference roughly proportional to the separation distance up to about 15°.
8. The energy of corresponding boundaries in Ni and Al were computed. Overall, there was a strong scaling of boundary energy between the two materials, though low energy boundaries tended to deviate from this scaling. Candidates for simple materials properties that govern this behavior were considered. The most promising are the shear moduli. Examination of more materials is required to clarify this.

Overall, our survey of grain boundaries energies shows no clear correlation between energy and the parameters typically associated with energy in the literature. A similar conclusion was reached previously by Sutton and Balluffi [23]. Clearly, a more general model for grain boundary energy is called for. The current results provide an extensive database of grain boundary energies that could be used to motivate and/or test a global model for the variation of boundary energy over the five-dimensional space of boundary orientations. To facilitate the development and testing of such models, a catalogue of the macroscopic boundary geometries for these 388 boundaries and the corresponding calculated boundary energies for Ni and Al are available as supplementary data to this publication. In addition, these data could be mined for interesting trends using an informatics approach or could be used in an interpolative fashion to determine the energy of boundaries not directly modeled.A definition of distance in the five-dimensional crystallographic space[71] such as that developed by Morawiec[72, 76] or by one of the authors[56] is needed to implement such an interpolation approach[71].

Future work will consider the energetics of boundaries in additional materials to further clarify the issue of the scaling of boundary energies between materials. In related work, the mobilities of these boundaries have been computed using a recently developed synthetic driving force[19]; that work will provide a similar survey of boundary mobility for a portion of this catalog of boundary structures[18].

4.6. Appendix A

To define the crystallographic distance between two grain boundaries, a form of the description of an individual grain boundary must be chosen. Consider an initially perfect crystal and a fixed dividing plane. A grain boundary between grains A and B can be described by an ordered pair (**A**,**B**) where **A** and **B** are rotation matrices describing the rotation applied to grains A and B on each side of the dividing plane to form the boundary. Note that this description has six degrees of freedom. The additional degree of freedom occurs because a rotation of both crystals about the normal to the dividing plane produces physically equivalent grain boundaries. The distance between two grain boundaries (**A**,**B**) and (**C**,**D**) is defined to be $d = \sqrt{2}\,Min\sqrt{3 - Tr(\mathbf{A}^{-1}\mathbf{C}) + 3 - Tr(\mathbf{B}^{-1}\mathbf{D})}$. In this expression, Min refers to a minimization over: a) rotations around the boundary normal, b) the choice of the assignment of grains A and B, c) the symmetry operations of each of the crystals, and d) taking the mirror image of the boundary. This metric is from Olmsted [56], which provides a complete description of the metric and a discussion of its mathematical properties. In figure 6 the rough conversion of d to an angle is given by $2\cos^{-1}\left(1 - d^2/4\right)$. This agrees with the difference in twist angles of two twist boundaries about the same axis, as long as the difference is not so large that one of the rotation symmetries comes into play.

4.7. References

[1] Humphreys FJ, Hatherly M. Recrystallization and Related Annealing Phenomena. Oxford: Elsevier, 1995.

[2] Gottstein G, Shvindlerman LS. Grain Boundary Migration in Metals: Thermodynamics, Kinetics, Applications. Boca Raton: CRC Press, 1999.

[3] Sutton AP, Balluffi RW. Interfaces in Crystalline Materials. Oxford: Clarendon Press, 1995.

[4] Gruber J, George DC, Kuprat AP, Rohrer GS, Rollett AD. Effect of Anisotropic Grain Boundary Properties on Grain Boundary Plane Distributions during Grain Growth. Scripta Materialia 2005;53:351.

[5] Holm EA, Hasson GN, Miodownik MA. On Misorientation Distribution Evolution during Anisotropic Grain Growth. Acta Materialia 2001;49:2981.

[6] Upmanyu M, Hassold GN, Kazaryan A, Holm EA, Wang Y, Patton B, Srolovitz DJ. Boundary Mobility and Energy Anisotropy Effects on Microstructural Evolution During Grain Growth. Interface Science 2002;10:201.

[7] Kinderlehrer D, Livshits I, Rohrer GS, Ta'asan S, Yu P. Materials Science Forum 2004:1063.
[8] Kazaryan A, Wang Y, Dregia SA, Patton BR. Grain Growth in Anisotropic Systems: Comparison of Effects of Energy and Mobility. Acta Materialia 2002;50:2491.
[9] Wolf D. Atomic-level geometry of crystalline interfaces. In: Wolf D, Yip S, editors. Materials Interfaces: Atomic-level structure and properties. London: Chapman and Hall, 1992.
[10] Upmanyu M, Srolovitz DJ, Shvindlerman LS, Gottstein G. Misorientation dependence of intrinsic grain boundary mobility: simulation and experiment. Acta Materialia 1998;47:3901.
[11] Demirel MC, Kuprat AP, George DC, Rollett AD. Bridging Simulations and Experiments in Microstructure Evolution. Physical Review Letters 2003;90:016106.
[12] Upmanyu M, Smith RW, Srolovitz DJ. Atomistic Simulation of Curvature Driven Grain Boundary Migration. Interface Science 1998;6:41.
[13] Schönfelder B, Wolf D, Phillpot SR, Furtkamp M. Molecular-Dynamics Method for the Simulation of Grain Boundary Migration. Interface Science 1997;5:245.
[14] Zhang H, Mendelev MI, Srolovitz DJ. Computer simulation of the elastically driven migration of a flat grain boundary. Acta Materialia 2004;52:2569.
[15] Zhang H, Upmanyu M, Srolovitz DJ. Curvature driven grain boundary migration in aluminum: molecular dynamics simulations. Acta Materialia 2005;53:79.
[16] Coffman VR, Sethna JP. Grain boundary energies and cohesive strength as a function of geometry. Physical Review B 2008;77:144111.
[17] Lee B-J, Choi S-H. Computation of grain boundary energies. Modelling and Simulation in Materials Science and Engineering 2004;12:621.
[18] Olmsted D, Holm EA, Foiles SM. Survey of Grain Boundary Proerties in FCC Metals: II. Grain Boundary Mobility. in preparation.
[19] Janssens KGF, Olmsted D, Holm EA, Foiles SM, Plimpton SJ, Derlet PM. Computing the Mobility of Grain Boundaries. Nature Materials 2006;5:124.
[20] Wolf D, Yip S. Materials Interfaces: Atomic-level structure and properties. London: Chapman & Hall, 1992.
[21] Hasson G, Boos J-Y, Herbeuval I, Biscondi M, Goux C. Theoretical and Experimental Determinations of Grain Boundary Structures and Energies: Correlation with Various Experimental Results. Surface Science 1972;31:115.
[22] Shih KK, Li JCM. Energy of Grain Boundaries between Cusp Misorientations. Surface Science 1975;50:109.
[23] Sutton AP, Balluffi RW. On Geometric Criteria for Low Interfacial Energy. Acta Metallurgica 1987;35:2177.
[24] Sutton AP. Grain-boundary Structure. International Metals Reviews 1984;29:377.
[25] Sutton AP, Balluffi RW, Vitek V. On Intrinsic Secondary Grain Boundary Dislocations arrays in High Angle Symmetrical Tilt Grain Boundaries. Scripta Metallurgica 1981;15:989.
[26] Wolf D. Structure-energy correlation for grain boundaries in fcc metals I. Boundaries on the (111) and (100) planes. Acta Metallurgica 1989;37:1983.
[27] Wolf D. Structure-energy correlation for grain boundaries in fcc metals II. Boundaries on the (110) and (113) planes. Acta Metallurgica 1989;37:2823.
[28] Wolf D. Structure-energy correlation for grain boundaries in fcc metals III. Symmetrical tilt boundaries. Acta Materialia 1990;38:781.
[29] Wolf D. Structure-energy correlation for grain boundaries in fcc metals IV. Asymmetrical twist (general) boundaries. Acta Materialia 1990;38:791.

[30] Schwartz D, Bristowe PD, Vitek V. Dislocation structure and energy of high angle [001] twist boundaries: A computer simulation study. Acta Metallurgica 1988;36:675.
[31] Sutton AP, Vitek V. On the Structure of Tilt Grain Boundaries in Cubic Metals I. Symmetrical Tilt Boundaries. Philosophical Transactions of the Royal Society of London. Series A, Mathematical and Physical Sciences 1983;309:1.
[32] Sutton AP, Vitek V. On the Structure of Tilt Grain Boundaries in Cubic Metals II. Asymmetrical Tilt Boundaries. Philosophical Transactions of the Royal Society of London. Series A, Mathematical and Physical Sciences 1983;309:37.
[33] Sutton AP, Vitek V. On the Structure of Tilt Grain Boundaries in Cubic Metals. III. Generalizations of the Structural Study and Implications for the Properties of Grain Boundaries. Philosophical Transactions of the Royal Society of London. Series A, Mathematical and Physical Sciences 1983;309:55.
[34] Schwartz D, Vitek V, Sutton AP. Atomic structure of (001) twist boundaries in f.c.c. metals. Structural unit model. Philosophical Magazine A 1985;51:499.
[35] Wang G-J, Sutton AP, Vitek V. A Computer Simulation Study of <001> and <111> Tilt Boundaries: The Multiplicity of Structures. Acta Metallurgica 1984;32:1093.
[36] Wang G-J, Vitek V. Relationships between grain boundary structure and energy. Acta Metallurgica 1986;34:951.
[37] Schmidt C, Finnis MW, Ernst F, Vitek V. Theoretical and experimental investigations of structures and energies of Σ=3, [112] tilt grain boundaries in copper. Philosophical Magazine A 1998;77:1161.
[38] Wolf D. Correlation between the energy and structure of grain boundaries in bcc metals I. Symmetrical boundaries on the (110) and (100) planes. Philosophical Magazine B 1989;59:667.
[39] Wolf D. Correlation between the energy and structure of grain boundaries in b.c.c. metals II. Symmetrical tilt boundaries. Philosophical Magazine A 1990;62:447.
[40] Wolf D. Structure and energy of general grain boundaries in bcc metals. Journal of Applied Physics 1991;69:185.
[41] Tschopp MA, McDowell DL. Asymmetric tilt grain boundary structure and energy in copper and aluminum. Philosophical Magazine 2007;87:3871.
[42] Tschopp MA, McDowell DL. Structures and energies of Σ3 asymmetric tilt grain boundaries in copper and aluminum. Philosophical Magazine 2007;87:3147.
[43] Wolf D, Merkle KL. Correlation between the structure and energy of grain boundaries in metals. In: Wolf D, Yip S, editors. Materials Interfaces: Atomic-level structure and properties. London: Chapman-Hall, 1992. p.87.
[44] Yang C-C, Rollett AD, Mullins WW. Measuring relative grain boundary energies and mobilities in an aluminum foil from triple junction geometry. Scripta Materialia 2001;44:2735.
[45] Saylor DM, El Dasher BS, Rollett AD, Rohrer GS. Distribution of grain boundaries in aluminum as a function of five macroscopic parameters. Acta Materialia 2004;52:3649.
[46] Barmak K, Kim J, Kim K-S, Archibald WE, Rohrer GS, Rollett AD, Kinderlehrer D, Ta'asan S, Zhang H, Srolovitz DJ. Grain Boundary Energy and Grain Growth in Al Films: Comparison of Experiments and Simulations. Scripta Materialia 2006;54:1059.
[47] Kim C-S, Hu Y, Rohrer GS, Randle V. Five-parameter Grain Boundary Distribution in Grain Boundary Engineered Brass. Scripta Materialia 2005;52:633.
[48] Saylor DM, Morawiec A, Rohrer GS. The relative free energies of grain boundaries in magnesia as a function of five macroscopic parameters. Acta Materialia 2003;51:3675.

[49] Saylor DM, Morawiec A, Rohrer GS. Distribution of grain boundaries in magnesia as a function of five macroscopic parameters. Acta Materialia 2003;51:3663.
[50] Read WT, Shockley W. Dislocation Models of Crystal Grain Boundaries. Physical Review 1950;78:275.
[51] Wolf D. A Read-Shockley Model for High-Angle Grain Boundaries. Scripta Metallurgica 1989;23:1713.
[52] Wolf D, Phillpot SR. Role of the Densest Lattice Planes in the Stability of Crystalline Interfaces: A Computer Simulation Study. Materials Science and Engineering A 1989;107:3.
[53] Wolf D. A broken-bond model for grain boundaries in face-centered cubic metals. Journal of Applied Physics 1990;68:3221.
[54] Wynblatt P, Shi Z. Relation between Grain Boundary Segregation and Grain Boundary Character in FCC alloys. Journal of Materials Science 2005;40:2765.
[55] Wynblatt P, Takashima M. Correlation of Grain Boundary Character with Wetting Behavior. Interface Science 2001;9:265.
[56] Olmsted DL. A New Class of Metrics for the Macroscopic Crystallographic Space of Grain Boundaries. Acta Materialia 2009: 57:2793.
[57] Sutton AP. Irrational Interfaces. Progress in Materials Science 1992;36:167.
[58] Daw MS, Foiles SM, Baskes MI. The Embedded-Atom Method: A Review of Theory and Applications. Materials Science Reports 1993;9:251.
[59] Foiles SM, Hoyt JJ. Computation of Grain Boundary Stiffness and Mobility from Boundary Fluctuations. Acta Materialia 2006;54:3351.
[60] Ercolessi F, Adams JB. Europhysics Letters 1994;26:583.
[61] Zimmerman JA, Gao H, Abraham FF. Generalized Stacking Fault Energies for Embedded Atom FCC metals Modelling and Simulation in Materials Science and Engineering 2000;8:103.
[62] Plimpton SJ. Large-scale Atomic/Molecular Massively Parallel Simulator. Sandia National Laboratories, 2007.
[63] von Alfthan S, Kaski K, Sutton AP. Order and structural units in simulations of twist grain boundaries in silicon at absolute zero. Physical Review B 2006;74:134101.
[64] Vitek V, Minonishi Y, Wang G-J. Multiplicity of grain boundary structures: vacancies in boundaries and transformations of the boundary structure. Journal de Physique Colloque 1985;46:141.
[65] von Alfthan S, Haynes PD, Kaski K, Sutton AP. Are the Structures of Twist Grain Boundaries in Silicon Ordered at 0 K? Physical Review Letters 2006;96:055505.
[66] Randle V. The Role of the Grain Boundary Plane in Cubic Polycrystals. Acta Materialia 1997;46:1459.
[67] Cahn JW. Stability, Microstructural Evolution, Grain Growth, and Coarsening in a Two-Dimensional Two-Phase Microstructure. Acta Metallurgica et Materialia 1991;39:2189.
[68] Merkle KL. Quantification of atomic-scale grain boundary parameters by high-resolution electron microscopy. Ultramicroscopy 1992;40:281.
[69] Wolf D. Correlation between energy and volume expansion for grain boundaries in fcc metals. Scripta Metallurgica 1989;23:1913.
[70] Rohrer GS, Saylor DM, Dasher BE, Adams BL, Rollett AD, Wynblatt P. The distribution of internal interfaces in polycrystals. Zeitschrift für Metallkunde 2004;95:197.
[71] Cahn JW, Taylor JE. Metrics, Measures, and Parametrizations for Grain Boundaries: A Dialog. Journal of Materials Science 2006;41:7669.

[72] Morawiec A. Method to Calculate the Grain Boundary Energy Distribution over the Space of Macroscopic Boundary Parameters from the Geometry of Triple Junctions. Acta Materialia 2000;48:3525.
[73] Brandon DG. The Structure of High-Angle Grain Boundaries. Acta Metallurgica 1966;14:1479.
[74] Hirth JP, Lothe J. Theory of Dislocations, Second Edition. New York: John Wiley & Sons, 1982.
[75] Udler D, Seidman DN. Grain Boundary and Surface Energies of FCC Metals. Physical Review B 1996;54:R11133.
[76] Morawiec A. Symmetries of Grain Boundary Distributions. In: Weiland H, Adams BL, Rollett AD, editors. Third International Conference on Grain Growth: TMS, 1998. p.509.

5. Survey of grain boundary properties in FCC metals II: Grain boundary mobility

5.1. Abstract

The absolute grain boundary mobility of 388 nickel grain boundaries described in Part I was calculated using a synthetic driving force molecular dynamics method. Over 25% of the 388 boundaries, including most of the non-Σ3 highest mobility boundaries, moved by a coupled shear mechanism. The range of non-shearing boundary mobilities is from 40 to 400 $m/s \cdot GPa$, except for Σ3 incoherent twins with mobilities of 200 to 2000 $m/s \cdot GPa$. Some boundaries, including all the <111> twist boundaries, are immobile within the resolution of the simulation. Boundary mobility is not correlated with scalar parameters such as disorientation angle, Σ value, excess volume, or boundary energy. Boundaries less than 15° from each other in five-dimensional crystallographic space tend to have similar mobilities. Some boundaries move via a non-activated motion mechanism, which greatly increases low temperature mobility. Thermal roughening of grain boundaries is widely observed, with estimated roughening temperatures substantially among boundaries.

5.2. Introduction

Microstructure – defined as the distribution of internal interfaces, defects, and phases – governs many properties of materials, including strength, toughness, conductivity, magnetic susceptibility, etc. Because microstructure is critical to materials performance, materials processing focuses on controlling and optimizing it. In polycrystalline materials, grain structure is a dominant feature of the microstructure. Since grain structure changes via motion of the grain boundaries, grain boundary properties play an important role in microstructural evolution.

Grain boundary motion is generally observed to be a driven process [1], with boundary velocity proportional to the product of a mobility and a driving force. In essence, the driving force is the *reason* grain boundaries move; the mobility determines *how fast* they move. Both the driving force and the mobility can be extrinsically manipulated to some extent. For example, second phase particles may be added to decrease the interfacial energy driving force via Zener pinning [2]; solute species may be added to decrease grain boundary mobility via solute drag [3]. The driving force and mobility together control the development of both the grain morphology (grain size distribution, abnormal grain growth) and crystallography (texture, boundary character distribution). The survey of grain boundary energies in Part I addresses the driving force for curvature driven motion as a function of boundary crystallography [4]. Since it is half of the equation that governs microstructural evolution, characterizing mobility is equally important to understanding material processing and is the subject of this paper.

Understanding the intrinsic grain boundary mobility is complicated by the fact that the mobility depends on grain boundary crystallography, which has five degrees of freedom [5]. (A grain boundary has three macroscopic degrees of freedom that describe crystallographic misorientation – typically a rotation angle and axis of rotation – and two macroscopic degrees of freedom that characterize the grain boundary plane.) Grain boundary mobility varies with all five degrees of freedom [6], and the differences can be substantial. For example, the <111> coherent twin is far less mobile than the <111> incoherent twins [1], despite sharing a common misorientation.

The variation in intrinsic grain boundary mobility with crystallography has been widely studied and reviewed, c.f. [1, 7]. Early experimental studies on lead bicrystals used a stored energy driving force to move a high angle boundary through a dislocation substructure [8, 9]. These studies focused on solute effects, but also showed that certain crystallographically special boundaries have very different mobility than general boundaries. Only the reduced mobility (the mobility-driving force product) could be measured in this way, and the boundary plane could not be determined. Later bicrystal studies refined both grain boundary geometry and driving force. Examination of bicrystal boundaries moving under a curvature driving force gave reduced mobility as a function of misorientation (but not boundary plane) [10, 11]. Other studies propelled flat grain boundaries via magnetic [12], shear [13] or stored energy [14] driving forces, providing measurements of absolute mobility as a function of full boundary crystallography and confirming that mobility is independent of driving force. The range of boundaries studied was limited both by the difficulty of the experimental methods and, for magnetic and shear driving forces, the fact that only certain boundary geometries permit such a driving force.

Other investigators elected to study large numbers of boundaries in polycrystals, determining reduced mobility as a function of scalar parameters such as average disorientation angle [15, 16] or boundary complexion [17]. One polycrystal method sought to extract reduced mobility as a function of all five boundary degrees of freedom using careful characterization of the geometry and crystallography of triple junctions [18]; this method has not yet proved tractable, however.

Atomic-scale computer simulation has offered an alternative method for studying grain boundary mobility. Some studies directly parallel experimental efforts, generally sharing the same strengths and limitations; examples include the misorientation dependence of reduced mobility in curved bicrystal boundaries [10, 19, 20] and absolute mobility of flat boundaries under an elastic [21-23] or artificial [24-26] driving force. Other studies take advantage of the length and time resolution of atomic simulations to study mobility of flat boundaries in the zero driving force limit using fluctuation [27] or random walk [28] theory. To date, all of these studies are limited to at most a few tens of grain boundary structures.

Polycrystalline microstructures typically contain a large diversity of grain boundaries. Modeling the evolution of such systems requires knowing the mobility of a spectrum of grain boundaries, from low to high angle, special to general. The boundary mobility should be the absolute mobility given in terms of the full five crystallographic degrees of freedom. To date, none of the experimental or computational efforts have succeeded in generating such a dataset.

Our goal for this study is to develop and apply a computational method for determining the absolute mobility of a wide range of grain boundaries spanning the five-dimensional space of boundary crystallography. To accomplish this efficiently, we require an automated method that can operate on flat boundaries using a small system size for short run times. To this end, a synthetic driving force method for determining grain boundary mobility was developed [24]. We describe the method and its results below.

5.3. Method

5.3.1. The synthetic driving force method

Grain boundaries move in response to a driving force, which is a free energy decrease per unit volume swept out [29]. In normal grain growth, the driving force is the reduction in grain boundary free energy and results in motion by curvature. Other driving forces for boundary motion may include chemical, magnetic or mechanical free energy contributions. On the atomic scale, the precise nature of the driving force should be irrelevant; atomic fluctuations that move the boundary are favored if the free energy decreases, regardless of the source of the decrease. Thus, in the limit of low driving force, the mobility should be independent of the type of driving force.

While atomic scale simulations can model driving forces that arise from physical processes, they also offer the opportunity to manipulate driving force directly via the atomic potential energy function, creating a 'synthetic driving force' for boundary motion. A synthetic driving force can overcome some computational challenges posed by physical driving forces. For example, atomic scale simulations of boundary motion by curvature require large system sizes and cannot resolve boundary plane effects [10, 20]. Simulations of stress- or magnetically-driven boundary motion are limited to certain boundary geometries [12, 13]. On the other hand, the synthetic driving force may be applied to any boundary configuration, curved or flat. This enables us to examine boundary mobility for arbitrary boundary geometries as a function of the five crystallographic degrees of freedom.

In previous studies, we compared the mobility produced by a synthetic driving force to that occurring from the simulation of a physical driving force (stress anisotropy) [25]. We found that the two driving forces gave the same mobility, suggesting that mobility is a physical property of a boundary, independent of the nature of the driving force.

The synthetic driving force method for computing grain boundary mobility has been described briefly in [24]and will be discussed in more detail here. A similar approach was also proposed by another group in [26]. Classical molecular dynamics (MD) is based on a position-dependent potential energy function $\Phi = \Phi(\mathbf{r}_1, \mathbf{r}_2, \ldots, \mathbf{r}_N)$, where N is the number of atoms, and $\mathbf{r}_i$ is the position of atom i. In order to exert a driving force on the grain boundary, the potential is taken as $\Phi = \Phi_0 + \Phi_u$, where Φ_0 is the normal potential describing the material, and $\Phi_u = \sum_{i=1}^{N} u_i$ is an additional potential where u_i depends on the crystallographic environment of each atom. We choose u_i such that the orientation of one grain is energetically favored over the orientation of the other grain.

To compute u_i we select one of the grains as the reference crystal, and let $\{\mathbf{R}_\alpha\}_{\alpha=1,12}$ be the 12 fcc nearest neighbor vectors in the perfect lattice of the reference grain, scaled to the lattice constant at the nominal simulation temperature. For the 12 nearest neighbors of atom i (or all of the neighbors within a certain distance, if there are less than 12) we look at $\Delta_{ij} \equiv \left|\mathbf{r}_{ji} - \mathbf{R}_\alpha\right|$ where $\mathbf{r}_{ji} = \mathbf{r}_j - \mathbf{r}_i$, and $\mathbf{R}_\alpha$ is chosen from the 12 possible near neighbor vectors to minimize Δ_{ij}. We

define an order parameter for each atom $\xi_i \equiv (12/n_i)\sum_{j=1}^{n_i}\Delta_{ij}$, where n_i is the number of neighbors. For atoms in the interior of the reference crystal, ξ is expected to be small, while for atoms in the interior of the other grain we expect $\xi \approx \xi_0 \equiv \min\sum_{\alpha=1}^{12}|\mathbf{R}'_\alpha - \mathbf{R}_\alpha|$, where $\{\mathbf{R}'_\alpha\}_{\alpha=1,12}$ are the nearest neighbor vectors in the other grain. We thus expect ξ/ξ_0 to be close to 0 in the reference crystal and close to 1 in the other crystal. Because thermal fluctuations cause these values to vary, we choose high and low cutoff values, $\xi_{\text{low}} \equiv f_{\text{low}}\xi_0$ and $\xi_{\text{high}} \equiv f_{\text{high}}\xi_0$, and treat all atoms with $\xi_i \le \xi_{\text{low}}$ as consistent with the reference grain, and all atoms with $\xi_i \ge \xi_{\text{high}}$ as consistent with the other grain. In this work we have taken $f_{\text{low}} = 0.25$ and $f_{\text{high}} = 0.75$.

We normalize the order parameter across the boundary such that

$$\omega_i \equiv \begin{cases} 0 & \xi_i \le \xi_{\text{low}} \\ \dfrac{\xi_i - \xi_{\text{low}}}{\xi_{\text{high}} - \xi_{\text{low}}} & \text{for} \quad \xi_{\text{low}} \le \xi_i \le \xi_{\text{high}} \\ 1 & \xi_i \ge \xi_{\text{high}} \end{cases} \tag{1}$$

and define the synthetic potential energy

$$u_i = (u_0/2)[1 - \cos(\pi\omega_i)] \tag{2}$$

where u_0 is a constant with dimensions of energy and controls the strength of the driving force. This form for u_i makes it continuous with continuous first derivatives (except in a few rare cases), and hence the forces are continuous functions of the positions of the atoms.

If the grain boundary moves a distance *x*, to a position where its structure is identical to its beginning structure, the potential energy will change by xAu/Ω, where A is the area of the boundary and Ω is the volume per atom, assuming that there are no excursions above ξ_{low} in the reference grain, or below ξ_{high} in the other grain. This creates a driving force for grain boundary motion. The actual thermodynamic boundary force, however, is the change in free energy, not the change in potential energy, and there will in fact be some excursions outside the ξ_{low} and ξ_{high} limits. The actual driving force must therefore be determined.

The actual thermodynamic driving force depends on u_0 and the boundary misorientation but not on the boundary plane. Call the reference crystal A and the other crystal B. The free energy difference per atom between crystal A and crystal B, both with the added potential turned on, is equal to the free energy difference between crystal A with the added potential turned on and with it off, less the same difference for B. The free energy difference between a crystal with the potential turned off and turned on can be computed as

$$\Delta G = \int_0^{u_0} \frac{1}{u}\left\langle \Phi_u \right\rangle_{u_0=u} du \tag{3}$$

where $\langle\ \rangle_{u_0=u}$ denotes the expectation value when the actual potential has $u_0 = u$, u is the dummy integration variable, and u_0 in the integral limit is the value for which the free energy difference is being calculated, e.g. [30]. In our computations the integrand is well behaved. For crystal B, the integrand is always equal to 1.0 to at least five decimal places, and so the free energy per atom is almost exactly u_0. For crystal A, however, the integrand is not always small. At 1200K the integrand varies from less than 0.01 to more than 0.99, depending primarily on the misorientation. The free energy difference between crystal A and crystal B at 1200K varies from 0.993 u_0 down to 0.008 u_0 for $u_0 = 0.01\,\mathrm{eV}$. Some other synthetic potential simulations presumed the potential energy difference and the driving force were equivalent [24, 26]; however since mobility is computed as a function of thermodynamic driving force, we must calculate and use the actual driving force, i.e. the free energy difference.

It should be noted that the synthetic potential does not conserve linear or angular momentum. For angular momentum, this should seem natural. The synthetic potential is trying to rotate grain B into the orientation of grain A; rotation is prevented by the boundary conditions parallel to the boundaryplane. The failure to conserve linear momentum can lead to an acceleration of the entire cell. Any motion of the entire cell is ignored in the analysis. That is to say, the motion of the grain boundary is measured with regard to the current position of the cell.

We also note that the synthetic potential method is effective only when the disorientation between the two grains is large enough that the difference between the near neighbor vectors in the two perfect crystals is greater than the typical differences in near neighbor vectors because of thermal fluctuations.

We utilize the synthetic driving force potential to compute grain boundary mobility by implementing it as an addition to the interatomic potential in a molecular dynamics code. The initial system is an energetically minimized bicrystal (generated as described below). We select one grain to be the reference grain A, with potential $\Phi=\Phi_0$, where Φ_0 is an appropriate classical potential, i.e. EAM Ni. The other grain B is given synthetic potential $\Phi=\Phi_0+\Phi_u$. (Note that Φ_u can be positive or negative, thus disfavoring or favoring orientation B; in this study, we use only positive Φ_u.) We then perform a MD simulation via a code such as LAMMPS[31, 32] and observe the motion of the boundary.

Since boundary velocity $v=Mf$ where M is the absolute mobility and f is the driving force, we can calculate M from the slope of the boundary position versus time plot. To determine boundary position, we use an order parameter closely related to that used in the synthetic driving force. For each atom we compute the difference between the driving force order parameter with crystal A as the reference and with crystal B as the reference. The final order parameter is approximately 1 in crystal A and -1 in crystal B. At small intervals in the direction of motion, say at position x', a weighted average of the order parameter for all atoms with their x coordinate close to x' is made, with closer atoms getting more weight. The position of the grain boundary is taken as the value of x' for which the average order parameter is zero. For an asymmetric boundary this order parameter is not necessarily (anti)symmetric with respect to reversing the x direction, so another approach (e.g. fitting a tanh function) might give a different position for the center of the boundary. Since our interest is not in finding the center of the boundary, but in determining how

far it has moved during the simulation, any difference based on the shape of the boundary is irrelevant unless the boundary is changing shape.

We note the following features of boundary motion computed by this method:

- For a given driving force the average boundary velocity is constant over time, giving a constant mobility. Some boundaries show stepwise motion; others move continuously. Some boundary configurations undergo an initial transient before achieving constant velocity.
- For appropriate driving forces, velocities are well below the speed of sound in the crystal.
- For rough boundaries, the mobility is independent of the driving force over the range tested. For smooth boundaries, the mobility typically tends to zero at low driving force and increases with driving force as discussed in [25].
- For most boundaries the mobility is independent of which grain is favored; changing the direction of motion does not change *M*. For 4% of our boundaries there appear to be different mobilities in the two directions, at least for some temperatures.
- The mobility does not depend on thermodynamic ensemble [24].
- In this study, we use a positive Φ_u so that the unfavored grain has excess energy relative to the baseline potential. We have observed that using a negative Φ_u can affect boundary motion, possibly due to activation barrier effects discussed in [33].

5.3.2. Simulation parameters

In this study, we used the synthetic potential method to determine the mobility of 388 distinct grain boundaries, which were constructed as described in Part I [4]. These boundaries represent a complete catalog of all boundaries that can be constructed in a periodic cell of size $15a_0/2$ or smaller, where a_0 is the lattice parameter. Since the computational cell is periodic in the plane of the boundary, all of these boundaries are CSL boundaries, with a maximum Σ of 385; there are 72 distinct misorientations represented. Boundaries were not of one specific character, but rather encompassed tilt, twist, mixed, high angle and low angle types; however, due to the construction method these boundaries are not uniformly distributed throughout the five dimensional boundary crystallography space. The boundaries were constructed and their energy was minimized using a thorough search scheme [4].

The computational cell was a bicrystal, with the boundary normal to the *x* direction and one grain arbitrarily assigned as the reference (favored) grain. The cell was periodic in the *y*- and *z*-directions, with free surfaces in the *x*-direction. Using free surfaces in the *x*-direction permitted a smaller cell size than in a fully periodic system and precluded boundary-boundary interactions. The total cell size was sufficient to give at least two repeats of the periodic structure in each direction [4]. This resulted in system sizes from 7,424 to 44,036 atoms.

Boundary motion was simulated via the synthetic driving force method, using the Foiles-Hoyt EAM Ni interatomic potential (which has a melting temperature of 1565K) [27], positive Φ_u on the unfavored grain, and actual driving forces ranging from ~0.04 to 0.35 GPa. The reported mobility value is for the largest driving force studied, at 1400K. Boundaries were typically driven at 600, 800, 1000, 1200 and 1400K for 160 ps at the largest driving force, with longer run times for the smaller driving forces. Simulations were performed using the LAMMPS MD code [31, 32].

The short time scale of MD simulations limits the boundary mobility range that can be accessed. During a 160 ps simulation, the boundary must move sufficiently to calculate a velocity that is not purely noise. We required the boundary to move about 10 angstroms in order to report a velocity. The situation is further complicated by the fact that the actual driving force becomes very small relative to the applied synthetic potential at small disorientations, as discussed above, so boundary velocity decreases proportionately. The limits of MD mobility resolution were calculated and are shown explicitly in some of the results below. While boundary mobilities below the resolution limit are reported as zero, their actual value may range from zero up to the mobility resolution limit.

5.4. Results and discussion

5.4.1. Mobility as a function of disorientation

Figure 1(a) shows grain boundary mobility as a function of disorientation angle at 1400K for a driving force generated by u=0.025 eV/atom for the 388 boundaries studied. We observe little, if any, correlation between mobility and disorientation. Σ3 60° twin boundaries have a very wide range of mobilities, depending on boundary plane, as reported earlier [1, 24], and <111> twist boundaries have uniformly low mobility [1] (below the resolution limits of the simulation). Other commonly studied boundary types, such as <100> twist and <110> symmetric tilt boundaries, show no systematic variation with disorientation. The range of measured mobilities is from 40 to 2000 $m/s \cdot GPa$ (excluding unresolvable boundaries), much larger than is observed experimentally.

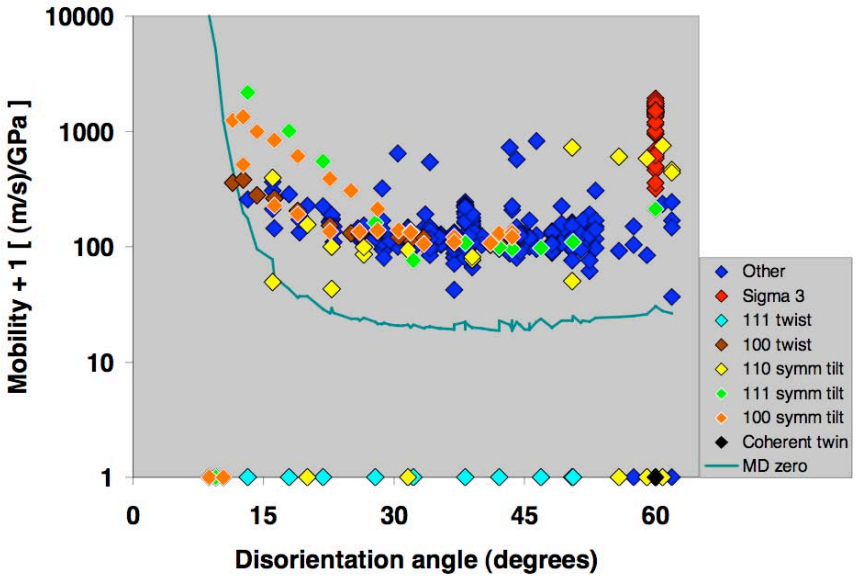

Figure 5-1. Mobility versus disorientation angle
Mobility as a function of disorientation angle for EAM Ni at 1400K (a)for all 388 boundaries simulated and (b)for the 285 boundaries with relative shear motion less than 0.15. Symbols are grain boundary mobilities, colored according to boundary type. The solid line is the resolution limit of the MD simulation.

5.4.2. Shear coupled motion

The computational cells in these simulations are bicrystals, unconstrained in the *y*- and *z*-directions. Cahn and Mishin have reported a shear coupled motion mechanism in some unconstrained bicrystal systems [34, 35], in which boundary motion in the *x*-direction is accompanied by shear in the *x*-plane. This shear can be substantial relative to the boundary displacement; for example, in the Σ5(310) boundary, the ratio of shear to displacement, or relative shear, is 1 at 800K.

When we measured shear during boundary motion at 1400K, we found that over a quarter of our 388 boundaries underwent significant shear, with 53 boundaries having relative shear greater than 0.25 and another 50 with relative shear between 0.15 and 0.25. While the tendency to shear is related to boundary structure, we did not find a correlation between shear motion and boundary energy, as shown in Figure 2(a). However, shear is strongly related to boundary mobility, with most of the non-Σ3, highest mobility boundaries moving by the coupled shear mechanism, as shown in Figure 2(b). (It is worth noting that many boundaries with 'normal' mobility undergo significant shear.) In contrast, the incoherent Σ3 twin boundaries have very high mobility and no indication ofcoupled shear. It appears that shear coupled motion is correlated with a mechanism for fast boundary motion; however, there is another fast motion mechanism available to Σ3 boundaries that involves essentially no shear.

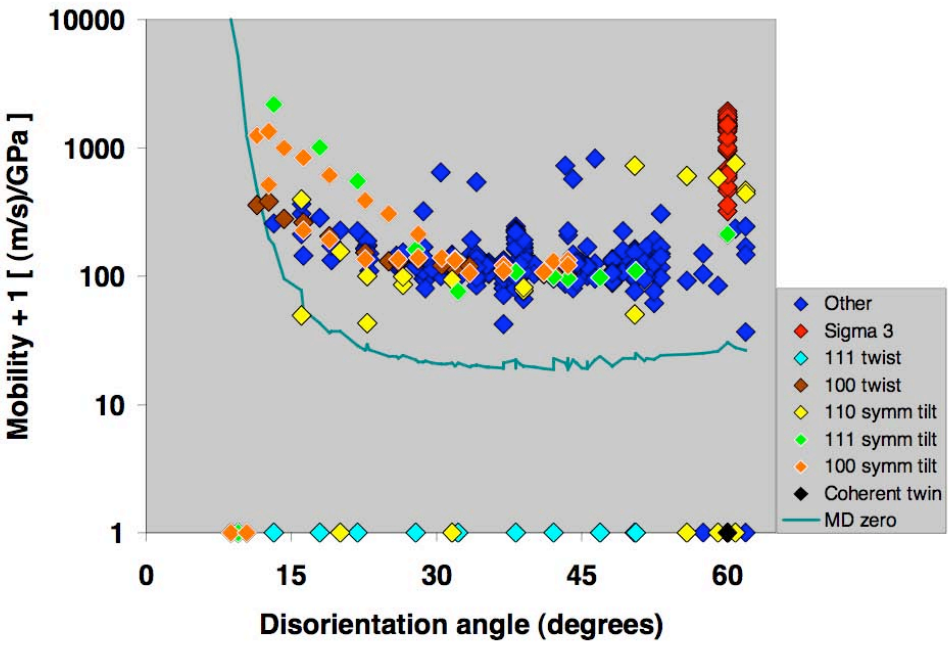

(a)

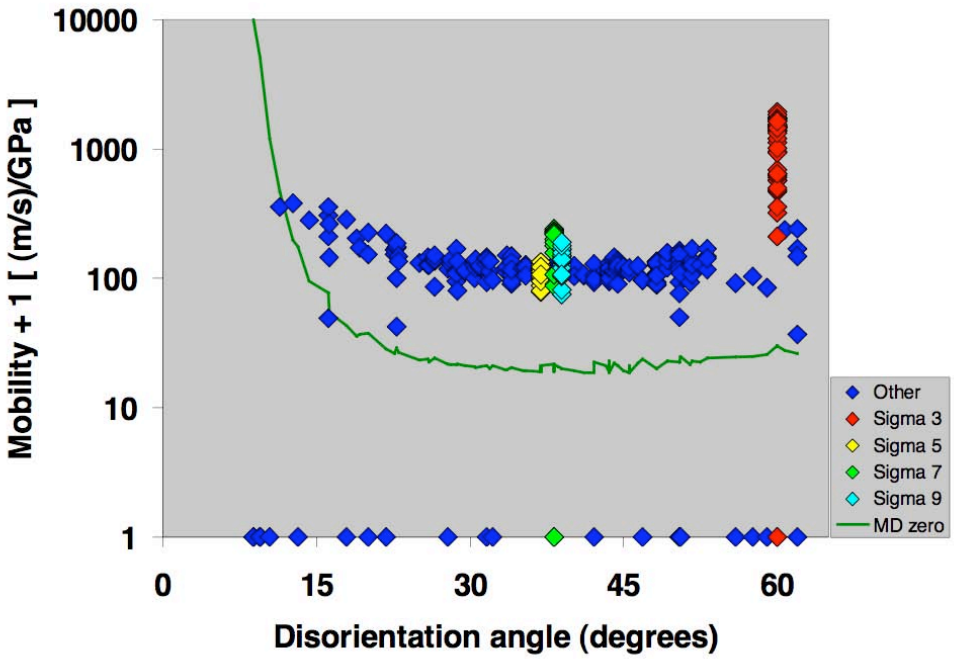

Figure 5-2. Correlation between shear and energy or mobility

(b)

Correlation between relative shear and (a)grain boundary energy or (b)grain boundary mobility for the 388 boundaries studied. Relative shear is defined as the ratio of shear strain to boundary displacement. Mobility data is for Foiles-Hoyt EAM Ni at 1400K and an applied potential of 0.025 eV/atom. Relative shear is an average over all applied potentials at 1400K. In (b) red symbols indicate incoherent S3 boundaries.

While we have not studied the effects of shear coupling in depth, we tested the effect of inhibiting shear motion by re-simulating a number of boundaries using fixed surface boundary conditions, where atoms are not permitted to leave the original periodic box. The 19 boundaries with relative shear between 0.12 and 0.15 were tested and showed no significant change in mobility when shear was inhibited. Five boundaries with relative shear between 0.21 and 0.28 and mobilities in excess of 400 $m/s \cdot GPa$ were also tested with shear motion inhibited. For these boundaries the mobility decreased to a value within the 'normal' range of 40 to 400 $m/s \cdot GPa$, or their mobility was below the limits of our simulations. Presumably, the normal, diffusion-mediated motion mechanisms are available to all boundaries, but are overshadowed by the faster shear mechanism when it is available.

Because constraints prevent shear from occurring during boundary motion in a bulk polycrystal, shear coupled boundary motion is likely not seen in most grain growth situations. If we eliminate shearing boundaries from our dataset, we find a much smaller range of mobilities, from 40 to 400 $m/s \cdot GPa$ (excluding unresolvable mobilities and incoherent Σ3 twin boundaries), as shown in Figure 1(b). These mobilities are much closer to, though still higher than, experimentally observed values and are of the same order of magnitude as seen in other MD studies of fcc grain boundaries [21-23, 26-28]. Since these boundaries are impurity-free, and because at the high temperatures and driving forces simulated some boundaries will be rough (high mobility) that would be smooth (low mobility) at the lower temperatures and driving forces often studied in experiments, the remaining discrepancy with experiments seems quite reasonable. Incoherent Σ3 twin boundaries remain very mobile, with mobilities from 200 to 2000 $m/s \cdot GPa$, approximately an order of magnitude faster than 'normal' boundaries. Σ 7 and Σ 9 boundaries also have a wider mobility range, though far less so than Σ 3. At low disorientation angles (below about 20°) mobility increases slightly, with mobilities for boundaries near 15° about three times typical mobilities at large angles, in contrast with most experimental results; our dataset does not include low angle boundaries below about 10°, however. The increase in mobility at small disorientation occurs near the limit of our mobility resolution. Additional tests at longer run times and twice the driving force, which decreases the resolvable mobility at 15° by a factor or 25, indicate that the mobility increase at low disorientations in not an artifact caused by the resolution limit. Overall, when shearing boundaries are not considered, boundary mobilities are more uniform, consistent, and physically reasonable.

5.4.3. Mobility correlations

Boundary mobility is often presumed to be related to other properties of the boundary. Having removed the anomalous shear boundaries, we examined the mobility data for some of these correlations.

Since grain boundaries with a low Σ value have a high density of coincident atoms, it has been suggested that they have low mobility (due to a small free volume to accommodate diffusive processes) or high mobility (due to the availability of diffusionless motion mechanisms). Figure 3(a) indicates that the mobility is not correlated with Σ value, with the lone exception of the generally fast Σ3 boundaries.

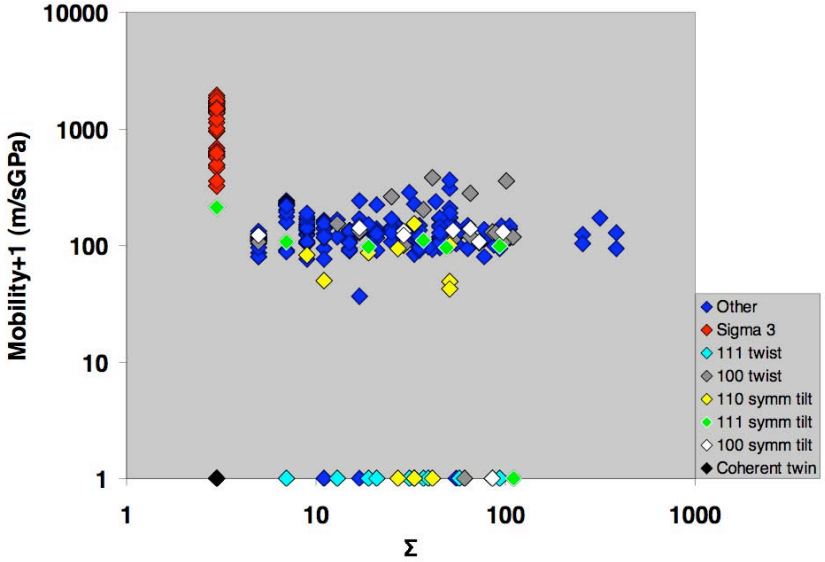
10000
1000
100
10
1
Mobility+1 (m/sGPa)
1
10
100
1000
Σ
Other
Sigma 3
111 twist
100 twist
110 symm tilt
111 symm tilt
100 symm tilt
Coherent twin

(a)

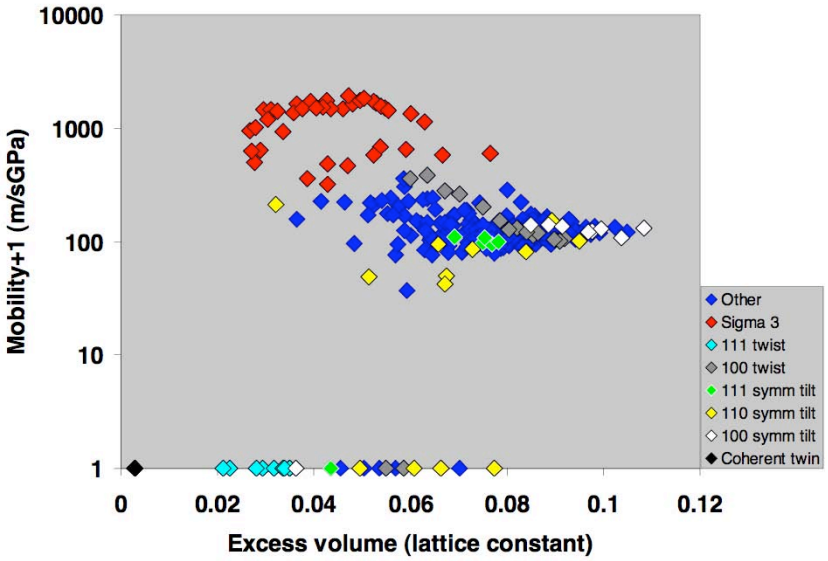
10000
1000
100
10
1
Mobility+1 (m/sGPa)
0
0.02
0.04
0.06
0.08
0.1
0.12
Excess volume (lattice constant)
Other
Sigma 3
111 twist
100 twist
111 symm tilt
110 symm tilt
100 symm tilt
Coherent twin

(b)

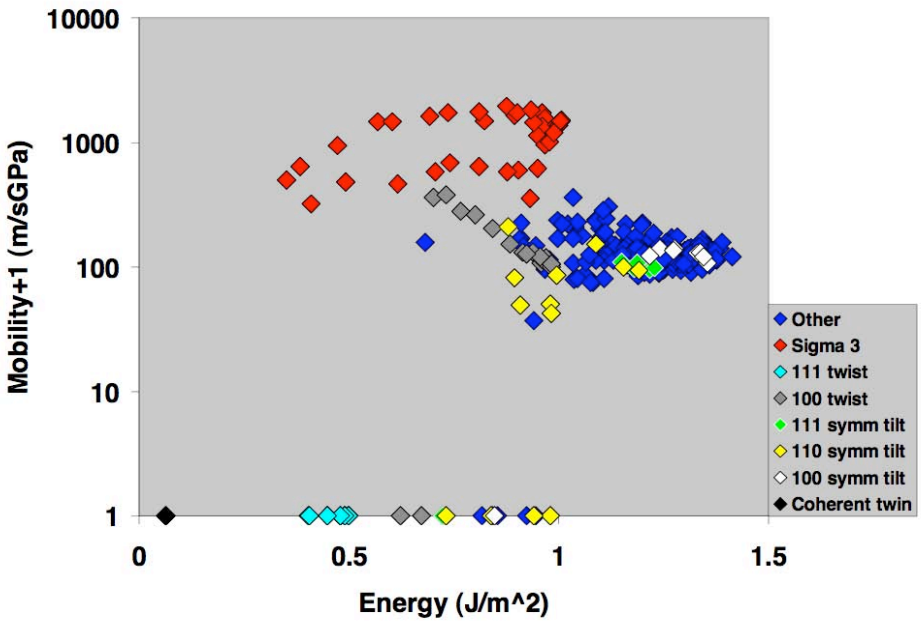

(c)

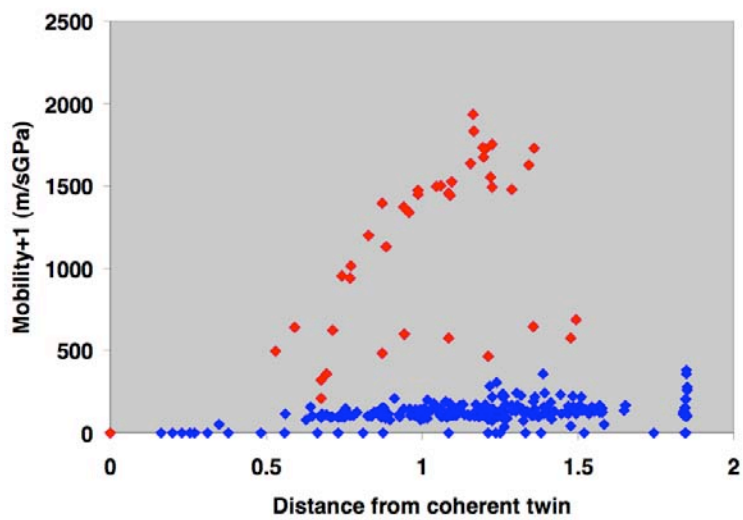

(d)

Figure 5-3. Correlations of mobility with other properties
Correlation of boundary mobility with (a)sigma value, (b)excess volume, (c)boundary energy, and (d)crystallographic distance from the coherent twin. All data are for Foiles-Hoyt EAM Ni at 1400K, and boundaries with relative shear motion greater than 0.15 are excluded.

A large excess volume (i.e. net expansion) at the grain boundary may decrease the activation barrier for diffusive processes (thus increasing *M*) or hinder boundary motion by eliminating multi-atom processes (thus decreasing *M*). Figure 3(b) shows that the mobility is not correlated with excess volume, although the range of observed mobilities increases as excess volume decreases, primarily due to the Σ3 boundaries, which are of high mobility and low excess

volume. Interestingly, both the highest and the lowest mobility boundaries have small excess volume.

Boundary mobility is often assumed to be related to boundary energy, since the structural factors that affect energy might also influence kinetic processes at the boundary. Figure 3(c) indicates that boundary mobility and energy are not correlated. (This is consistent with our previous results that energy is proportional to excess volume [4].) Again, the spread in mobility increases as energy decreases, primarily because the high mobility Σ3 boundaries have generally low energy.

The Σ3 coherent twin is of exceptionally low mobility, both experimentally and in this study. It is reasonable to hypothesize that boundaries that are crystallographically close to the coherent twin (perhaps sharing structural elements with it) would be slow as well. Figure 3(d), which plots mobility versus distance from the coherent twin using a crystallographic metric developed by one of us [36] and described briefly in Appendix A, indicates that boundaries near the coherent twin have very low mobility. As a caveat, however, we must note that this dataset does not contain any boundaries closer than about 10° to the coherent twin.

Overall, boundary mobility does not appear to be correlated with most of the obvious candidates: disorientation angle, Σ value, energy, or excess volume. There is some correlation with twin-like character; however, that correlation is valid only for boundaries quite close to the coherent twin in crystallographic space. Thus, we cannot predict mobility using these physical properties. Is it possible to predict the mobility of boundaries not included in this dataset from the boundaries studied here?

Figure 4 shows the difference in boundary mobility between pairs of boundaries as a function of the crystallographic distance between them as defined in Appendix A [36]. Boundaries that are close to each other in crystallographic space (that is, less than about 15° of separation) tend to have similar mobilities. The upper bound on the difference in mobilities is approximately proportional to separation distance, although the actual mobility difference may be lower for a given pair of boundaries. For boundaries farther apart than 15°, mobility difference is not well correlated, and may vary from very small to very large. This implies that the mobility results for the 388 boundaries studied here may be used to interpolate the mobility of other boundaries. Many interpolation schemes may be envisioned; perhaps the simplest is to approximate an unknown mobility as the crystallographically nearest known mobility, with error bars given by the upper bound in Figure 4. Thus, given a set of known boundary mobilities, we can determine unknown boundary mobilities to a confidence level that increases with the size of the known dataset. This is the input necessary for modeling microstructural evolution in a polycrystal containing many boundaries of arbitrary crystallography.

5.4.4. Temperature effects

To this point, we have considered boundaries at 1400K (~0.9 T_m) only. A full survey of the temperature dependence of boundary mobility is beyond the scope of this paper. However, two important temperature-dependent phenomena are non-activated boundary motion and the boundary roughening transition, which we discussed earlier for a few individual boundaries [25].

5.4.4.1. Non-Activated boundary motion

For most of the 388 boundaries in our dataset, when we plot mobility against temperature for a given driving force, we see evidence of an activated process: Mobility increases with temperature in an Arrhenius manner as shown in Figure 5(a). However, for 117 boundaries, we find that mobility decreases as temperature increases, at least over some temperature range, implying a non-activated motion mechanism. Non-activated boundaries undergo shear motion about as often as activated boundaries.

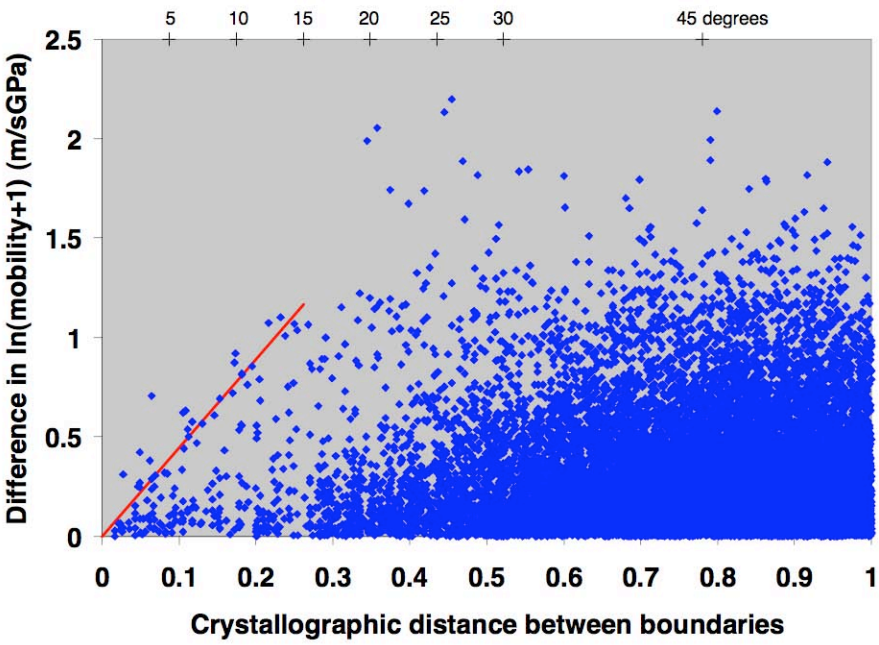

Figure 5-4. Difference of mobility between boundary pairs
The difference between the mobilities of pairs of boundaries as a function of the crystallographic distance between the boundaries. Only pairs separated by less than a distance of 1.0 are shown. The red line is chosen to include 90% of the data points where the distance is less that 0.25 (about 15°). Distance is calculated by a metric described in [36] and converted to degrees of separation as noted in Appendix A. All data are for Foiles-Hoyt EAM Ni at 1400K, and S3 boundaries, boundaries with relative shear motion greater than 0.15, and boundaries with mobility less than the resolution limit are excluded.

It is well known that dislocations can move in a barrier-free manner, where phonon damping decreases mobility at high temperatures. Since grain boundaries have a dislocation character, it is conceivable that they could move by a similar mechanism. In fact, Cahn and Mishin have observed diffusionless boundary motion that might be consistent with a non-activated process [34, 35]. In such systems, we expect mobility to scale as $1/T$.

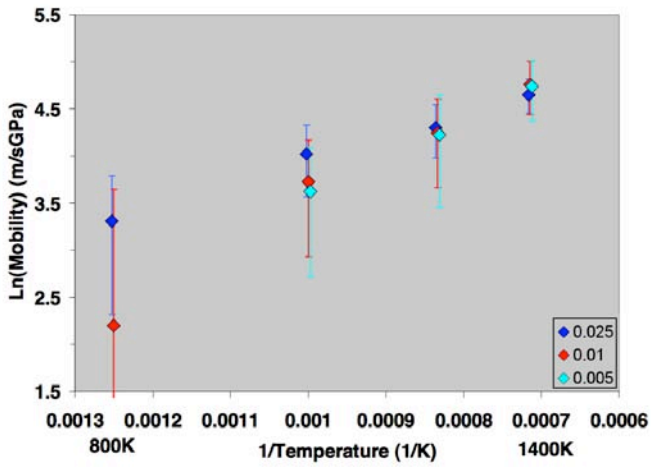

(a)

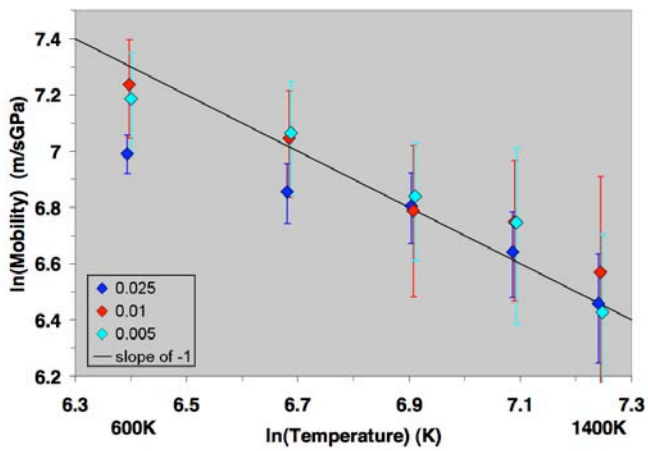

(b)

Figure 5-5. Temperature dependence of mobility

Temperature dependence of boundary mobility at driving forces of 0.025, 0.01, and 0.005 eV/atom for two representative grain boundaries. (a)Most boundaries in our dataset, including this S9 boundary with <5 4 2> and <2 1 0> normals (index number 271 in the supplemental data) undergo activated motion, where mobility increases with temperature in an Arrhenius manner. The slope of the log(*M*) versus 1/*T* curve is the activation energy. (b)117 boundaries in our dataset, including this S3 boundary with <11 8 5> normals (index number 366 in the supplemental data) undergo non-activated motion, characterized by a mobility that decreases as temperature increases. For most of these boundaries, mobility is proportional to 1/*T*, suggesting phonon damped motion. The error estimates for mobility are approximate, based on velocity fluctuations during boundary motion.

While we have not examined motion mechanisms in detail, most of the non-activated boundaries (about 63 of 117) show mobility linear with 1/*T* over some temperature range as shown in Figure

5(b), consitent with phonon-damped motion. (The remaining 54 non-activated boundaries are not easily classified, but share the common feature that the mobility is not monotonically increasing with temperature.) Many of the non-activated boundaries remain so over the temperature range studied; however, about 20 show a transition from non-activated motion at low temperature to activated motion at high temperature. The remaining boundaries show other temperature dependencies. It is interesting that of 43 boundaries that are non-activated over the full temperature range studied, 30 are Σ3 boundaries with high mobility at 1400K. (The remaining 13 Σ3 boundaries studied show activated motion.)

Some boundaries that have normal, activated mobilities at low driving forces move in a non-activated manner at high driving force. These 'dynamically mobile' boundaries are in addition to the 117 non-activated boundaries described above. Since mobility is not correlated with non-activated motion (i.e. non-activated boundaries may be fast, slow, or in-between), we do not call out the non-activated boundaries when reporting mobility. However, this motion mode is distinct from the presumptive activated behavior, and deserves recognition and further study.

Whether non-activated, phonon-damped motion can occur in the presence of other motion disruptors, such as dislocations, solutes, or triple junctions, is an open question. It is possible that this motion mechanism cannot be realized in physical systems.

5.4.4.2. Boundary roughening transition

Both faceted and unfaceted boundaries are observed to undergo a transition from a smooth configuration to a rough configuration as temperature increases [25]. We previously described the characteristics of the ideal roughening transition for activated boundary motion. At low temperatures, the boundary is smooth; boundary mobility is low and decreases as the driving force tends to zero; and boundary motion is stepwise in units consistent with the atomic repeat distance. At the roughening temperature T_r, there is a jump in mobility. Above T_r, the boundary is rough; boundary mobility is high and constant with driving force; and boundary motion is continuous. We note that among the boundaries we have studied, there are many exceptions to this 'ideal' roughening behavior, including the non-activated motion described above.

We examined the mobility of our 388 boundaries at several temperatures and driving forces, and we identified 259 boundaries that conformed reasonably well to the 'ideal' roughening profile. (This set excludes the 117 non-activated boundaries, as well as 14 otherwise anomalous boundaries.) For each of the well-behaved boundaries we estimated T_r based on both a qualitative transition in the mobility versus driving force behavior at T_r. We note that this estimate is both subjective (depending where we perceived a change in behavior in a typically noisy data set) and approximate (because M was measured in 200K increments). In addition, the distribution of roughening temperatures for our boundaries cannot be taken as representative of boundaries in general, because our dataset includes a greater than random fraction of high symmetry boundaries. Nonetheless, we found a distribution of roughening temperatures for these boundaries as shown in Figure 6. Boundaries that have mobility independent of driving force at 600K are assumed to have roughening transitions below 600K, and boundaries that do not move at 1400K are assumed to have roughening transitions above 1400K; both are indicated by open symbols in Figure 6.

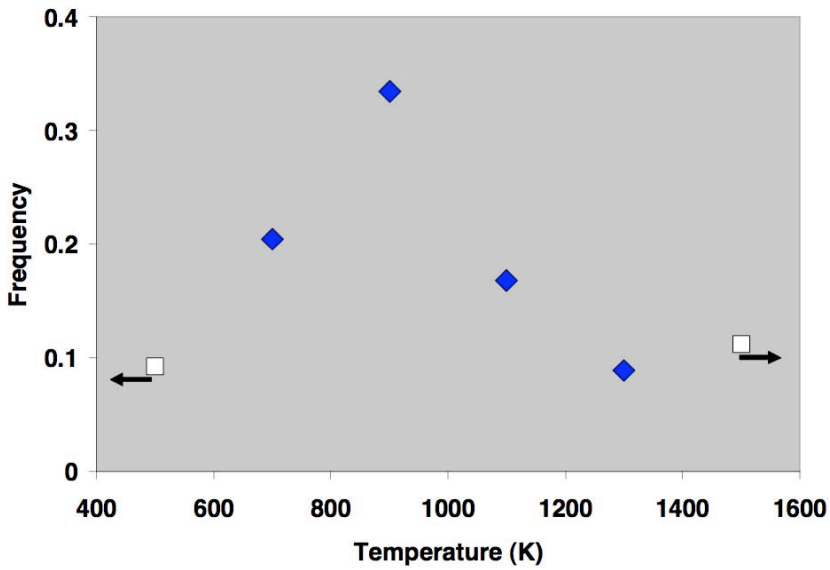

Figure 5-6. Distribution of roughening transition temperature
Distribution of roughening transition temperature T_r for 259 grain boundaries. Boundaries that have mobility independent of driving force at 600K are assumed to have roughening transitions below 600K, and boundaries that do not move at 1400K are assumed to have roughening transitions above 1400K; both are indicated by open symbols. Leaving out the endpoints, the mean roughening temperature is about 900K, with a standard deviation of about 200K. Note that the assignment of a roughening transition temperature is somewhat subjective and approximate.

The distribution of roughening temperatures (excluding endpoints) appears approximately symmetric, with a mean T_r of about 900K and a standard deviation of about 200K. Note that only about 60% of the boundaries have roughened at 900K (0.58 T_m, a reasonable annealing temperature), and about 10% of the boundaries remain smooth (low mobility) at 1400K, or about 90% of the melting temperature, the temperature of most of the mobility data presented here.

We note that we do not observe any correlation between T_r and disorientation angle or boundary energy, but we do find that boundaries that are crystallographically close tend to have similar roughening temperatures. This suggests that T_r is a physical property of grain boundaries and not just a simulation artifact.

Boundary roughening could have a significant effect on microstructural evolution in polycrystals. At typical annealing temperatures, significant fractions of grain boundaries may be smooth and have very low mobility. Microstructures that contain fast and slow boundaries can evolve very differently from homogeneous systems; microstructural outcomes can include abnormal grain growth, pinning, and changes in grain size distribution, c.f. [37].

In bulk polycrystals, grain boundaries are not flat, as simulated here, but curved. How boundary curvature affects the roughening transition is an open question.

5.5. Conclusions

In this study, we used a synthetic driving force method to compute absolute grain boundary mobility and applied it to a catalog of 388 grain boundaries in fcc nickel. The method is efficient, operating on flat boundaries using small systems and short runs. The result is the largest and broadest set of boundary mobility data generated to date.

From these results, we made the following observations:

- Over a quarter of the 388 boundaries moved by a coupled shear mechanism, in which boundary motion is accompanied by significant shear parallel to the boundary.

- Most of the highest mobility grain boundaries move by coupled shear. When shear is inhibited, mobility decreases to a more moderate level. In contrast, the Σ3 incoherent twins, which also have very high mobility, move without significant shear.

- Some boundaries have a non-activated motion mechanism available, which greatly increases low temperature mobility.

- Discounting boundaries that move by coupled shear, the range of boundary mobilities is from 40 to 400 $m/s \cdot GPa$, higher than in experiments but consistent with other MD studies. Some boundaries, including all the <111> twist boundaries, are immobile within the resolution of the simulation. Σ3 twin boundaries have a wider range of mobilities, from 200 to 2000 $m/s \cdot GPa$, with the coherent twin essentially immobile.

- Boundary mobility is not correlated with any typical, scalar parameters we have studied, including disorientation angle, Σ value, excess volume, or boundary energy.

- Boundaries that are less than 15° apart from each other in five-dimensional crystallographic space tend to have similar mobilities, with the upper bound on mobility difference approximately proportional to crystallographic separation distance. This permits an unknown mobility to be interpolated from a known mobility. The mobilities of boundaries farther than 15° apart not well correlated.

- Thermal roughening of grain boundaries is widely observed in our boundary catalog. Boundaries below their roughening temperature have low mobility, and mobility increases sharply above the roughening temperature. The estimated roughening temperatures are distributed over a 1000K range, with mean roughening temperature approximately 900K and standard deviation about 200K. A few boundaries remain smooth at 90% of the melting temperature.

Overall, this study does not suggest a simple, physical model for grain boundary mobility; however, it does enable interpolation of unknown mobilities from the calculated values. Further investigations in the mobility database may reveal insights toward model development or trends via data mining. To that end, the catalog of boundary geometries and their associated mobilities are available online as supplementary data to this publication.

This study has revealed great complexity in the temperature dependence of grain boundary mobility. Further study is clearly required in order to understand both thermal roughening and temperature-dependent motion mechanisms that may be important in polycrystalline microstructural evolution.

5.6. Appendix A

To define the crystallographic distance between two grain boundaries, a form of the description of the boundary must be chosen. Consider an initially perfect crystal and a fixed dividing plane. A grain boundary can be described by an ordered pair (**A**,**B**) where **A** and **B** are rotation matrices describing the rotation applied to the material on each side of the dividing plane to form the boundary. Note that this description has six degrees of freedom. The additional degree of freedom occurs because a rotation of both crystals about the normal to the dividing plane produces physically equivalent grain boundaries. The distance between two grain boundaries (**A**,**B**) and (**C**,**D**) is defined to be $d = Min\sqrt{3 - Tr(A^{-1}C) + 3 - Tr(B^{-1}D)}$. In this expression, Min refers to a minimization over: a) rotations around the boundary normal, b) the choice of the assignment of crystals A and B, c) the symmetry operations of each of the crystals, and d) taking the mirror image of the boundary. Note that minimization a) can be performed analytically and the other minimizations involve a finite number of discreet operations. A rough conversion of *d* to an angle is given by $2\arccos\left(1 - \frac{d^2}{4}\right)$. This agrees with the difference in twist angles of two twist boundaries, as long as the difference is not so large that one of the rotation symmetries comes into play. A complete description of the metric and a discussion of its mathematical properties is presented by Olmsted [36].

5.7. References

1. Gottstein, G., D.A. Molodov, and L.S. Shvindlerman, *Grain Boundary Migration in Metals: Recent Developments.* Interface Science, 1998. **6**: p. 7-22.
2. Smith, C.S., *Grains, Phases and Interfaces: An Interpretation of Microstructure.* Trans. AIME, 1948. **175**: p. 15-51.
3. Cahn, J.W., *The impurity-drag effect in grain boundary motion.* Acta Metallurgica, 1962. **10**(9): p. 789-798.
4. Olmsted, D., S.M. Foiles, and E.A. Holm, *Survey of grain boundary properties in FCC metals: Grain boundary energy.* in press, 2008.
5. Sutton, A.P. and R.W. Balluffi, *Interfaces in Crystalline Materials*. 1995, Oxford: Clarendon Press.
6. Randle, V., *The Role of the Grain Boundary Plane in Cubic Polycrystals.* Acta Materialia, 1997. **46**: p. 1459-1480.
7. Grant, E., A. Porter, and B. Ralph, *Grain boundary migration in single-phase and particle-containing materials.* Journal of Materials Science, 1984. **19**: p. 3554-3573.
8. Aust, K.T. and J.W. Rutter, *Grain boundary migration in high-purity lead and dilute lead-tin alloys.* Trans. AIME, 1959. **215**: p. 119-127.

9. Aust, K.T. and J.W. Rutter, *Temperature dependence of grain migration in high-purity lead containing small additions of tin.* Trans. AIME, 1959. **215**: p. 820-831.
10. Upmanyu, M., et al., *Misorientation dependence of intrinsic grain boundary mobility: simulation and experiment.* Acta Materialia, 1999. **47**: p. 3901-3914.
11. Furtkamp, M., et al., *Grain boundary migration in Fe-3.5% Si bicrystals with [001] tilt boundaries.* Acta Materialia, 1998. **46**(12): p. 4103-4110.
12. Molodov, D.A., et al., *True absolute grain boundary mobility: Motion of specific planar boundaries in Bi bicrystals under magnetic driving forces.* Acta Materialia, 1998. **46**(16): p. 5627-5632.
13. Winning, M., G. Gottstein, and L.S. Shvindlerman, *On the mechanisms of grain boundary migration.* Acta Materialia, 2002. **50**: p. 353-363.
14. Taheri, M.L., et al., *Grain boundary mobility under a stored-energy driving force: A comparison to curvature-driven boundary migration.* Z. Metallkd., 2005. **96**(10): p. 1-5.
15. Huang, Y. and F.J. Humphreys, *Subgrain growth and low angle boundary mobility in aluminium crystals of orientation (110)(001).* Acta Materialia, 2000. **48**(8): p. 2017-30.
16. Huang, Y., F.J. Humphreys, and M. Ferry, *The annealing behaviour of deformed cube-oriented aluminium single crystals.* Acta Materialia, 2000. **48**: p. 2543-2556.
17. Dillon, S.J. and M.P. Harmer, *Intrinsic grain boundary mobility in alumina.* J. Am. Ceram. Soc., 2006. **89**(12): p. 3885-3887.
18. Yang, C.-C., A.D. Rollett, and W.W. Mullins, *Measuring relative grain boundary energies and mobilities in an aluminum foil from triple junction geometry.* Scripta Materialia, 2001. **44**: p. 2735-3740.
19. Upmanyu, M., R.W. Smith, and D.J. Srolovitz, *Atomistic Simulation of Curvature Driven Grain Boundary Migration.* Interface Science, 1998. **6**: p. 41-58.
20. Zhang, H., M. Upmanyu, and D.J. Srolovitz, *Curvature driven grain boundary migration in aluminum: molecular dynamics simulations.* Acta Materialia, 2005. **53**: p. 79-86.
21. Schönfelder, B., G. Gottstein, and L.S. Shvindlerman, *Comparative study of grain-boundary migration and grain-boundary self-diffusion of [001] twist-grain boundaries in copper by atomistic simulations.* Acta Materialia, 2005. **53**: p. 1597-1609.
22. Zhang, H., M.I. Mendelev, and D.J. Srolovitz, *Computer simulation of the elastically driven migration of a flat grain boundary.* Acta Materialia, 2004. **52**: p. 2569-2576.
23. Zhou, L., H. Zhang, and D.J. Srolovitz, *A size effect in grain boundary migration: A molecular dynamics study of bicrystal thin films.* Acta Materialia, 2005. **53**: p. 5273-5279.
24. Janssens, K.G.F., et al., *Computing the mobility of grain boundaries.* Nature Materials, 2006. **5**: p. 124-127.
25. Olmsted, D.L., S.M. Foiles, and E.A. Holm, *Grain boundary interface roughening transition and its effect on grain boundary mobility for non-faceting boundaries.* Scripta Materialia, 2007. **57**: p. 1161-1164.
26. Schönfelder, B., G. Gottstein, and L.S. Shvindlerman, *Atomistic simulations of grain boundary migration in copper.* Metallurgical and Materials Transactions A, 2006. **37A**: p. 1757-1771.
27. Foiles, S.M. and J.J. Hoyt, *Computation of grain boundary stiffness and mobility from boundary fluctuations.* Acta Materialia, 2006. **54**: p. 3351-3357.
28. Trautt, Z.T., M. Upmanyu, and A. Karma, *Interface Mobility from Interface Random Walk.* Science, 2006. **314**: p. 632-635.

29. Taylor, J.E., J.W. Cahn, and C.A. Handwerker, *I - Geometric Models of Crystal Growth.* Acta Metallurgica et Materialia, 1992. **40**(7): p. 1443-1474.
30. Straatsma, T.P., H.J.C. Berendsen, and J.P.M. Postma, *Free energy of hydrophobic hydration: A molecular dynamics study of noble gases in water*. J. Chem. Phys., 1968. **85**: p. 6720-6727.
31. Plimpton, S.J., *LAMMPS: Large-scale Atomic/Molecular Massively Parallel Simulator*. 2007, Sandia National Laboratories.
32. Plimpton, S.J., *Fast parallel algorithms for short-range molecular dynamics.* J. Comp. Phys., 1995. **117**: p. 1-19.
33. Upmanyu, M. and A.D. Rollett, *Effect of non-linear interface kinetics on coarsening phenomena.* in press, 2008.
34. Cahn, J.W., Y. Mishin, and A. Suzuki, *Coupling grain boundary motion to shear deformation.* Acta Materialia, 2006. **54**: p. 4953-4975.
35. Cahn, J.W., Y. Mishin, and A. Suzuki, *Duality of dislocation content of grain boundaries.* Philosophical Magazine A, 2006. **86**(25-26): p. 3965-3980.
36. Olmsted, D.L., *A new class of metrics for the macroscopic crystallographic space of grain boundaries.* in press, 2008.
37. Humphreys, F.J. and M. Hatherly, *Recrystallization and Related Annealing Phenomena*. 1995, Oxford: Elsevier.

6. Competitive Abnormal Grain Growth between Allotropic Phases in Nanocrystalline Nickel

6.1. Abstract

This article discusses both the presence and the competitive growth of the hexagonal close packed phase concurrently with the face centered cubic phase in nanocrystalline nickel thin films. Nickel thin films were produced by pulsed laser deposition and were then annealed at several temperatures (523-623K) in vacuum. Using transmission electron diffraction and electron backscattered diffraction, HCP grains were observed to grow within an initially nanocrystalline FCC matrix at several different annealing conditions (523-623K) and in appreciable fractions. Both phases exhibit abnormal grain growth in which a sub-population of grains grows much larger and more rapidly than the majority of the microstructure. In addition, the defect structures for the abnormal grains are qualitatively different depending upon the particular phase of the abnormal grain. We hypothesize that it is the differences in defect energies within the hexagonal and cubic lattices that might make this metastable arrangement possible.

6.2. Introduction

The central driving force for the study of nanoscale materials is the expectation that these materials will behave in substantially different ways than in their more traditional, microscale counterparts. In particular, a great deal of work has examined the changes in thermodynamic phase stability as a function of nanoparticle or nanocrystallite size. [1-6] It has been shown that allotropic stability, melting temperature, and lattice parameters all change for particles below a certain size. For example, metals such as chromium and tungsten are observed in the FCC structure instead of their normal body-centered cubic (BCC) structure, for particles less than 30 nm in diameter [2]; similarly zirconium is BCC instead of hexagonal close packed (HCP).

When processed through traditional means, the metal nickel is almost always observed with the face centered cubic (FCC) crystal structure. However, there have been reports of the unexpected hexagonal close-packed (HCP) phase in nanocrystalline nickel, produced both by chemical routes [7, 8], thermal reduction [9]and by pulsed laser deposition (PLD) [10]. In all of these examples, the supposition and observation have been that the HCP phase is less stable than the FCC phase and that simple annealing of the material would cause a direct phase transformation to the more stable form. The work of Vergara and Madurga on nickel thin films created by PLD has shown specifically that films with an initially single phase, HCP structure, can be systematically transformed as a function of time and temperature to single phase, FCC structure. [10]

We show in this paper the both the presence and the competitive growth of the HCP phase concurrently with the FCC phase. We will discuss the conditions for the HCP phase appearance and growth, the qualitative differences between the HCP and FCC phases, and will offer an initial hypothesis to explain this suprising metastable state.

6.3. Experimental Methods.

The nickel thin films were produced by pulsed laser deposition and prepared for TEM as described in the recent work of Hattar, Follstaedt, et al. [11]. This work also describes the *in situ TEM* heating protocols used for annealing the samples at several temperatures (523-623K). The TEM analyses were performed on a Philips CM20T instrument operated at 200 kV. The average initial grain size in these films was measured to be 10 nm with a range of 2-16 nm as determined by transmission electron microscopy (TEM).

Electron backscattered diffraction (EBSD) experiments were performed on these same TEM samples after annealing in the TEM. The EBSD data was taken on a Zeiss Supra 55 VP-FEG SEM at 20keV using the HKL Channel 5 system with the Nordlys II CCD camera. Individual EBSD patterns were analysed using crystallographic input structures of Ni-FCC, Ni-HCP, Ni_2P, Ni_3P, NiO, NiS, NiS_2, and Ni_3S_2. The EBSD maps were taken with a step size of 10nm per point with scans of 200x200 steps.

X-ray diffraction was performed on a Siemens D500 instrument employing a sealed-tube Cu-Kα radiation source (40 kV / 30 mA), diffracted-beam graphite monochomator, and scintillation detector. The x-ray diffraction data was collected from an as-deposited film on a sodium chloride substrate.

6.4. Results

Electron backscattered diffraction (EBSD) measurements were able to identify individual HCP and FCC grains **(Fig. 1)**. The indexed grains were those that had grown substantially to sizes greater than 20 nm in diameter. Maps of EBSD data were generated for several annealing conditions **(Fig. 2)** for films with a nominal thickness of 90 nm. These maps show that HCP grains are present for all temperatures examined except for the 623K anneal. The HCP grains in the maps are similar in size and shape to the abnormal FCC grains and show no particular crystallographic orientation with respect to the film geometry, which is in contrast to the strong <111> fiber texture observed for the FCC phase **(Fig. 3)**. An anneal at 548K for 17 hours produced the greatest amount and largest size of HCP grains, 15% by area and 200 nm average diameter, respectively. The presence of HCP grains less than 20 nm in diameter could not be confirmed due to the spatial resolution of the EBSD technique.

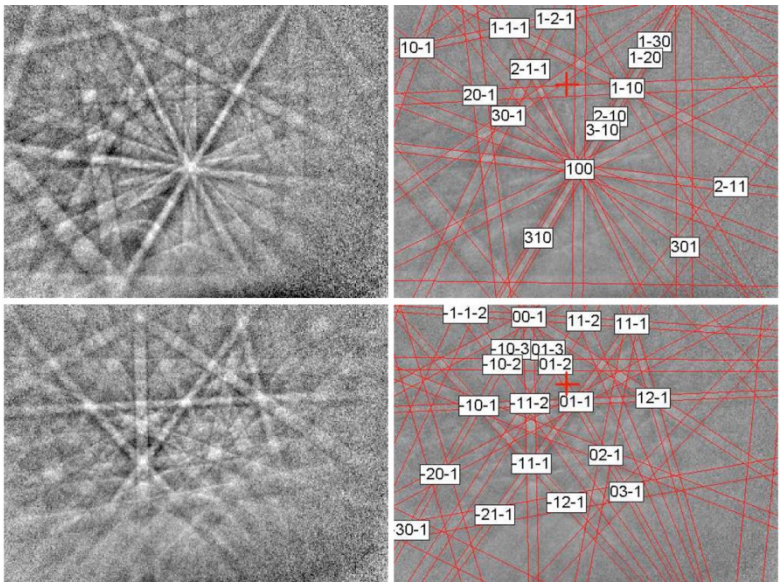

Figure 6-1. EBSD patterns for HCP nickel

EBSD patterns and indexed solutions for HCP nickel (Miller index notation). These patterns could not be correctly indexed for the FCC structure or for other possible impurity phases (e.g. NiO, NiS_2, Ni_2P, etc.).

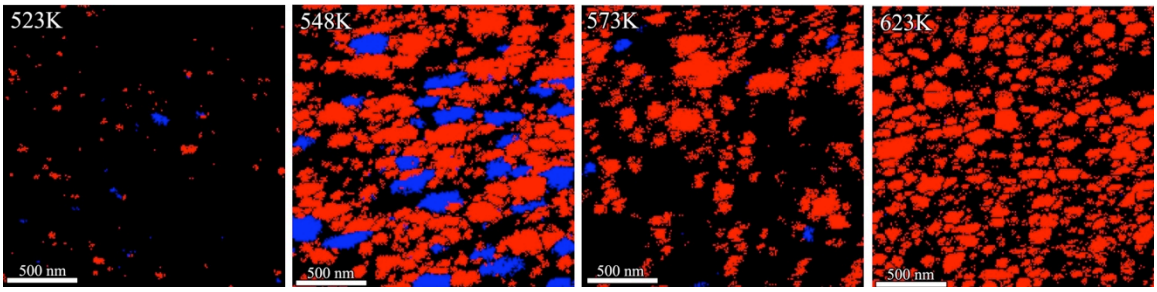

Figure 6-2. EBSD phase maps of abnormally grown grains

EBSD phase maps showing the distribution of the abnormally grown grains for both the FCC (red) and HCP (blue) phases. Annealing conditions were 14 hrs. at 523K, 17 hrs at 548K, 40 min. at 573K and 10 min. at 623K.

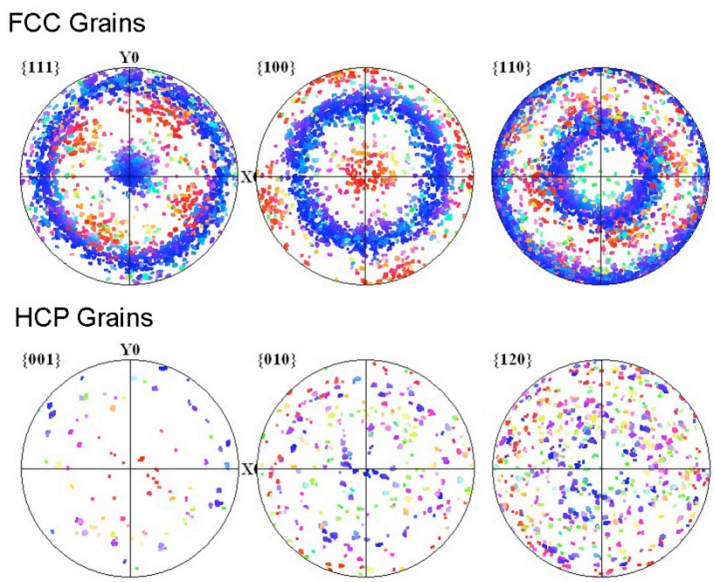

Figure 6-3. Pole figures of FCC and HCP grains
Pole figures generated from EBSD data showing the pronounced <111> fiber texture of the FCC abnormal grains in constrast with the lack of texture of the HCP abnormal grains (Miller index notation).

These observations of the HCP nickel phase were corroborated by transmission electron microscopy (TEM) images and diffraction patterns. Several grains in two 50 nm-thick films annealed at 548K and 623K were identified as HCP in the TEM by indexing selected area diffraction (SAD) patterns and by demonstrating the hexagonal symmetry via tilting experiments **(Figs. 4a and 4c)**. The HCP grains had the scalloped, concave boundary shapes **(Fig. 4b)** that have been previously observed for abnormal grain growth in PLD nickel. Certain orientations also showed streaking along the c-axis of the diffraction pattern (Fig. 4c) with corresponding images showing lamella parallel to the [0001] direction in the HCP lattice **(Fig. 4d)**. This layered structure is reminiscent of stacking faults and twins observed in FCC metals as well as lamellae observed in the martensitic phase transformation from FCC to HCP observed in cobalt and cobalt-nickel alloys. [12, 13] In addition to the HCP pattern, a second set of spots lying along the streaks can be indexed to a coherently strained FCC lattice with the following orientation relationship with respect to the HCP lattice:

$(0002)^{HCP} \parallel (111)^{FCC}$ (interfacial plane)

$[11\bar{2}0] \parallel [\bar{2}\bar{1}1]$ (directions in the plane)

While the aligned directions are not the orientation relationship found for cobalt, all the additional reflections can be accounted for by twinning of this FCC structure and multiple diffraction between the two phases. Additional investigation is needed to understand the formation, growth, and collapse of this defect structure, but a transformation from HCP to equilibrium FCC is reasonable to expect. At this point, we also do not know whether all HCP grains have this defective structure at all points of their growth or only as they are transformed to the FCC structure.

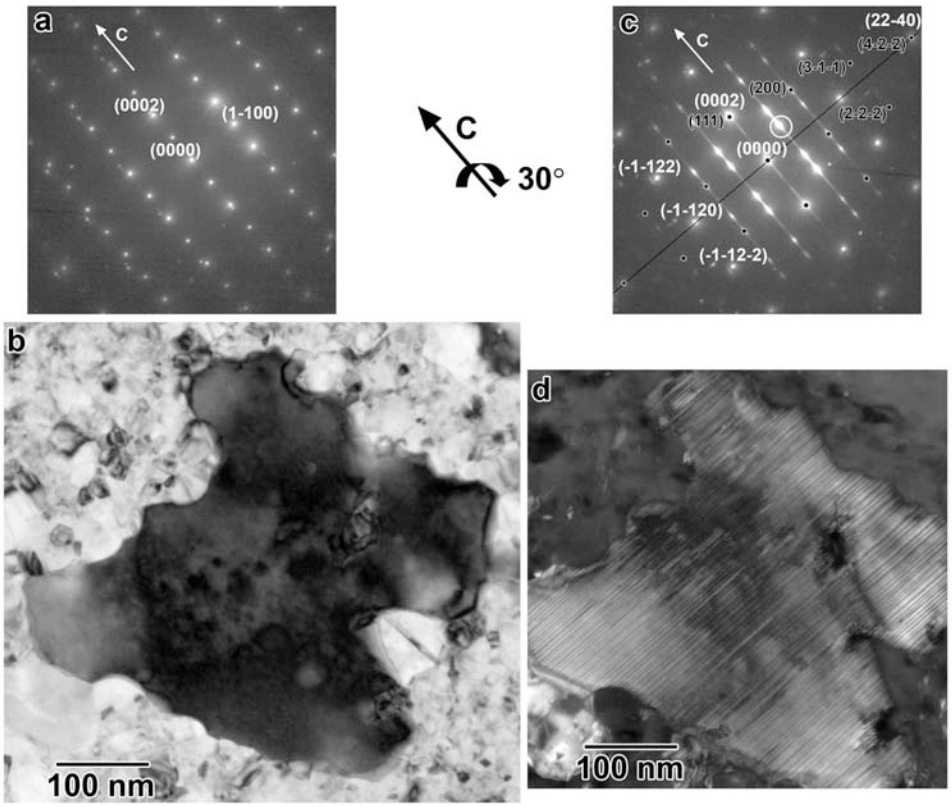

Figure 6-4. TEM image and diffraction patterns from a abnormal HCP grain
TEM images and diffraction patterns from a single, abnormal HCP grain (548K anneal). A.) Indexed selected area diffraction (SAD) pattern from the <11-20> zone axis of the HCP crystal. B.) Bright-field image of the scalloped grain in that orientation. C.) Indexed SAD pattern from the same grain rotated 30º about the c axis to the <1-100> HCP zone axis (indexed in white), with proposed strained <01-1> FCC zone axis pattern (black spots and indices). Other spots along the streaks result from FCC twinning and multiple diffraction. D.) Dark-field image showing lamella in the grain in the <1-100> orientation of C) using the streak and reflection circled.

Neither TEM nor x-ray diffraction showed the presence of the HCP phase in as-deposited films. The only visible diffraction rings from TEM selected area diffraction were indexed to the FCC phase. X-ray diffraction on an as-deposited film also showed only signal from the FCC phase **(Fig. 5)**. Despite this observation, simulations of powder x-ray diffraction for the as-deposited film geometry suggest that small, 10 nm, HCP grains could be present without producing enough diffracted signal to be observed with the current experimental conditions. Based on these results, it seems probable, but not certain, that the HCP phase is nucleating from initially FCC material.

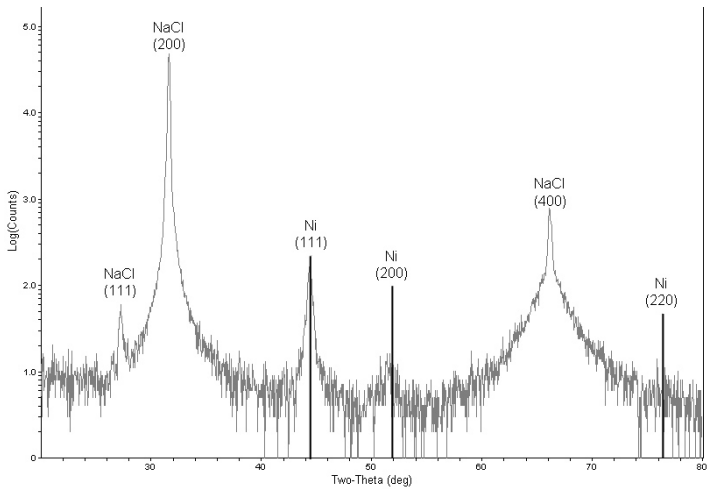

Figure 6-5. Powder x-ray diffraction from as-deposited nickel thin film
Powder x-ray diffraction data from as-deposited nickel thin film on sodium chloride substrate. The reflections marked for nickel are for the FCC phase. No reflections were observed for the HCP phase.

6.5. Discussion

There are several important observations that can be made about these complex microstructures. For the abnormal grains observed, there are no two HCP abnormal grains in contact, suggesting that HCP grains do not nucleate or grow from other HCP abnormal grains. In addition, the HCP abnormal grains are surrounded by many other, presumably FCC, grains that are 5-10 times smaller than the HCP grains. EBSD also showed that while the FCC abnormal grains possessed a strong <111> fiber texture or crystalline orientation with respect to the substrate, the HCP abnormal grains have seemingly random growth orientations. This observation is true even when abnormal grains of both phases are in contact with one another, as seen in the film annealed at 548K. Thus, the HCP abnormal grains are not templating upon the FCC abnormal grains in the microstructure. Our principal finding is that HCP grains compete with FCC grains during abnormal grain growth at these relatively low temperatures.

These observations highlight the complexity in nanostructural evolution when the system is far from equilibrium. In the absence of impurities, the Gibbs phase rule denotes that these structures are not in equilibrium, as it is not possible to have two phases in the same one-component (i.e. pure nickel) system. Compositional measurements such as Rutherford back-scattering, energy-dispersive x-ray spectroscopy, and electron energy loss spectroscopy performed on these films have not shown any significant presence of impurities which correlates with FCC and HCP grains (down to the 0.1 wt% level). Global minimization of the free energy of the thin film would drive the growth of FCC grains to reduce grain boundary area and to minimize the volume of the HCP phase. The calculated difference in cohesive energies for the FCC and HCP lattices is large enough, 1.83eV/nm^3[14], that the reduction in interfacial area alone cannot explain the appearance of the HCP phase for all but the smallest, less than 10 nm, grains.

Current theories for abnormal grain growth are also not able to explain the existence and grain growth of the HCP phase. Usually, abnormal grain growth is explained by particular grain boundaries possessing either a mobility advantage or an energy advantage. In other cases,

abnormal grain growth can be driven by a preferred crystallographic orientation for certain grains with respect to the surface. In these experiments, there was no meaningful difference in the size or shape of the HCP and FCC grains, thus casting doubt on the possibility of a significant difference in interfacial energy or mobility difference between HCP-FCC interfaces and FCC-FCC grain boundaries. Also, the HCP abnormal grains are randomly oriented thus nullifying explanations based on crystallographic orientation with respect to the film surface.

The defect structures within these films may provide clues for explaining the metastable existence and growth of the HCP phase. The observations in this letter combined with those in the recent work of Hattar et al. show both unusual planar defects, nanometer scale, lamellar structures in Figure 3; and point defect clusters, stacking fault tetrahedra, and dislocation loops. [11] One of the few differences between the HCP and FCC abnormal grains is the presence of the lamellar structures in some of the HCP grains observed, while none were observed in the FCC grains. Conversely, the FCC grains showed stacking fault tetrahedra and other defects that the HCP grains did not. The presence of the stacking fault tetrahedral and dislocation loops indicate a vacancy point defect concentration greater than would be expected for the annealing conditions examined in this article. It has been observed that the high angle grain boundaries of nanocrystalline metals have a large vacancy concentration. [15] When grains grow and reduce grain boundary area, the vacancies from the grain boundaries must be incorporated into the lattice or dispersed to a free surface. It is postulated that the FCC and HCP crystal structures incorporate the vacancies differently and so change the total energy of a given grain. If this change in energy is greater than or equal to 1.83eV/nm^3, then the growth of an HCP nickel phase would be energetically feasible.

6.6. Conclusions

The principal finding of this work is that HCP grains compete with FCC grains during abnormal grain growth in nanocrystalline, nickel thin films, exposed to low temperature anneals. This work was not able to definitively determine the origin of the HCP phase, but it suggests that the films are initially single phase, FCC structure. The abnormal HCP grains were similar in size and shape to the abnormal FCC grains, but possessed no crystallographic texture, while the abnormal FCC grains possessed a pronounced <111> fiber texture. In addition, some of the HCP grains observed exhibited a marked, nanoscale, lamellar defect structure without exhibiting the dislocations loops and stacking fault tetrahedra observed in abnormal FCC grains. The energetics that allow the apperance and growth of the HCP phase is currently not understood, but it is hypothesized that the difference in defect structures may be an important part of the explanation.

6.7. References:

[1] J. M. McHale, A. Auroux, A. J. Perrotta, A. Navrotsky, *Science* **1997**, *277*, 788.
[2] S. H. Huh, H. K. Kim, J. W. Park, G. H. Lee, *Physical Review B (Condensed Matter)* **2000**, *62*, 2937.
[3] U. Herr, *Advanced Engineering Materials* **2001**, *3*, 889.

[4] Y. H. Rong, Q. P. Meng, Y. L. Zhang, T. Y. Hsu, *Materials Science and Engineering A-Structural Materials Properties Microstructure and Processing***2006**, *438*, 414.
[5] X. Y. Song, L. M. Li, J. X. Zhang, *Rare Metals***2006**, *25*, 582.
[6] M. A. Shandiz, A. Safaei, S. Sanjabi, Z. H. Barber, *Solid State Communications***2008**, *145*, 432.
[7] Y. T. Jeon, J. Y. Moon, G. H. Lee, *Journal Physical Chemistry B***2006**, *110*, 1187.
[8] V. Tzitzios, G. Basina, M. Gjoka, V. Alexandrakis, V. Georgakilas, D. Niarchos, N. Boukos, D. Petridis, *Nanotechnology***2006**, *17*, 3750.
[9] Y. Mi, D. Yuan, Y. Liu, J. Zhang, Y. Xiao, *Materials Chemistry and Physics***2005**, *89*, 359.
[10] J. Vergara, V. Madurga, *Journal of Materials Research***2002**, *17*, 2099.
[11] K. Hattar, D. M. Follstaedt, J. A. Knapp, I. M. Robertson, *Acta Materialia***2008**, *56*, 794.
[12] C. Hitzenberger, H. P. Karnthaler, A. Korner, *Acta Metallurgica***1988**, *36*, 2719.
[13] H. T. Hesemann, P. Mullner, O. Kraft, E. Arzt, *Journal de Physique IV (Proceedings)***2003**, *112*, 107.
[14] X. He, L. T. Kong, B. X. Liu, *Journal of Applied Physics***2005**, *97*, 106107.
[15] R. J. Jahn, A. H. King, *Philosophical Magazine A (Physics of Condensed Matter, Defects and Mechanical Properties)***1986**, *54*, L3.

7. Temperature dependence of grain boundary free energy and elastic constants

7.1. Abstract

This work explores the suggestion that the temperature dependence of the grain boundary free energy can be estimated from the temperature dependence of the elastic constants. The temperature dependent free energy of a symmetric Σ79 tilt boundary is computed for an embedded atom method model of Ni using quasi-harmonic techniques at low temperatures and thermodynamic integration at moderate to high temperatures. The temperature dependent elastic constants are also computed for this model of Ni. It is shown that the grain boundary free energy scales with the product of the shear modulus, $C' = C_{44}$ times the temperature dependent lattice constant for temperatures up to about 0.75 T_M. At higher temperatures, the scaling is seen to break down.

7.2. Introduction

The distribution of internal interfaces, defects and phases, known as the material microstructure, governs many material properties such as strength, toughness, conductivity, magnetic susceptibility, etc. In polycrystalline materials, grain structure is a dominant feature of the microstructure and the focus of many aspects of materials processing. For these reasons the properties of grain boundaries, in particular their energies and mobility, are of fundamental importance. Therefore, there have been extensive studies of the energetics of grain boundaries from both computational and experimental perspectives[1].

The vast bulk of the computational studies of grain boundary energy have determined the zero-temperature excess enthalpy, or simply grain boundary energy, and have focused on the variation of the grain boundary energy with the structure and crystallography of the boundary. However, the relevant thermodynamic quantity is the finite-temperature interfacial free energy, γ, that represents the interfacial excess of the free energy [2]. This is a much more difficult quantity to calculate since free energies cannot be computed directly as an expectation value of an operator whereas the enthalpy can. Thus the determination of free energies requires more involved calculations such as thermodynamic integration techniques. There have been very few studies of the temperature dependence of the grain boundary free energy. Foiles[3] computed the temperature variation of interfacial free energy for a Σ5 (310)/[001] symmetric tilt boundary in Cu and found that γ decreases by about a factor of three as the temperature was increased from low temperature to near the melting point. Broughton and Gilmer [4, 5] examined the energy of selected tilt boundaries in a Lenard-Jones solid and found similar large decreases in the interfacial free energy. Due to the computational effort required to determine the temperature variation of γ, it would be convenient if this variation could be estimated from a more readily available quantity. Such a relationship would also be of value in theoretical modeling of high-temperature boundary effects such as grain boundary pre-melting[6]. The main point of this paper is to suggest such an approach.

Recall that a grain boundary can be treated, as least formally, as a array of dislocations [1]. The elastic strain energy of a dislocation is proportional to the shear elastic modulus of the material [7]. This suggests that there may be relationship between the energetics of a grain boundary and

the shear moduli. Also, the classic Read-Shockley model [8] indicates that the grain boundary energy should be proportional to the shear elastic moduli. For the case of the zero-temperature grain boundary energy, it has been seen that the relative energies of corresponding boundaries in different materials are correlated with the shear moduli of the materials [9, 10]. In this paper the possibility of determining the temperature variation of the grain boundary free energy from the temperature dependence of the shear moduli will be examined. The temperature dependent γ for a symmetric $\Sigma 79$ grain boundary in a model of Ni is computed and compared to the temperature dependence of the elastic moduli times the lattice constant computed for the same model of Ni.

7.3. Computational Method

The calculations here all use the same embedded atom method (EAM) [11] potential for Ni developed by Foiles and Hoyt [12]. This potential provides a reasonable description of the elastic properties, as seen below, and stacking fault energies of Ni. The computed melting point for this model is 1565 K compared to the experimental melting point of 1726 K. In the following, homologous temperatures are based on the melting point of this model.

The grain boundary considered in this study is a symmetric $\Sigma 79$ (-3 -7 10)/[1 1 1] tilt boundary. Due to the low density of coincident sites, this boundary should be a reasonable surrogate for a general boundary. The structure of this boundary was determined in an earlier study [13, 14]. The boundary structure optimization combined multiple conjugate gradient minimizations of different possible initial structures and the consideration of different combinations of atom addition and removal to obtain a near optimal structure.

The free energy of the grain boundary as a function of temperature is determined in two manners. For low temperatures, in this case $T/T_M \leq 0.25$, the free energy is determined via quasi-harmonic (QH) approximation calculations[15]. The QH approach is expected to be reliable at these temperatures since the atomic displacements are small. In addition, this temperature is near the Debye temperature of the bulk Ni and the QH approach incorporates quantum effects that are significant below the Debye temperature. In these calculations, the dynamical matrix of the system is computed and the phonon spectrum of the entire system is determined using standard techniques[11, 15]. The free energy of the full system is then obtained using the analytic expression for the free energy of a set of harmonic oscillators,

$$F = k_B T \sum_j \ln\left(2\sinh\frac{h\nu_j}{2k_B T}\right),$$

where T is the temperature, h is Planck's constant, k_B is Boltzman's constant and the ν_j are the normal mode frequencies of the oscillators. The structure used is the zero-temperature structure uniformly expanded to the finite temperature lattice constant determined by a bulk quasi-harmonic calculation. The interfacial free energy is then determined from the difference in free energy of the system with the grain boundary and that of a bulk system with the same number of atoms.

For higher temperatures, $T \geq 0.25\ T_M$, the free energy is computed via thermodynamic integration following the procedure described in detail by Frolov and Mishin[16]. A series of

molecular dynamics simulations are performed at differing temperatures with the bulk lattice constant chosen to yield zero stress in the bulk. For each calculation, one calculates the excess enthalpy, U^{ex}, and the interfacial stress, τ. The interfacial free energy can then be obtained by integrating the equation

$$d\left(\frac{\gamma A}{T}\right) = -\frac{U^{ex}}{T^2}dT + \frac{2\tau A}{T}\left(\frac{\partial e}{\partial T}\right)_{\sigma_{ij}=0}$$

where A is the interfacial area and e is the strain required to maintain zero bulk stress, σ. Note that one cannot extend this approach to zero-temperature due to the divergence of the integrand.

The last quantity that we need to calculate is the temperature dependent elastic constants. In this work we follow the procedure used by Wolf, Mansour, Lee and Ray[17]. In this approach molecular dynamics simulations are performed in the microcanonical ensemble with the internal energy and density chosen to yield the desired temperature and zero bulk pressure. The elastic constants are then evaluated from equations (3.4) through (3.8) of reference [17]. It should be noted that there is an inconsistency in the method of calculation used at low temperatures between the grain boundary free energy calculations and the elastic constant calculations. The grain boundary calculations employ quantum statistics at low temperatures while the elastic constant calculations employ classical statistics. However, at low temperatures, fluctuations make only a modest contribution to the elastic constant calculations so it is not expected that the difference between the use of classical and quantum descriptions of the fluctuations will alter the conclusions of this paper.

7.4. Results and Discussion

Figure 1 shows the computed grain boundary free energy, γ, for the symmetric $\Sigma 79$ grain boundary described above as a function of temperature from zero temperature to near the melting point. Similar to the results for a $\Sigma 5$ boundary determined in a prior study[3], there is a substantial variation of γ such that its value at the melting point is about a third of the low temperature value. There is also a point shown at zero temperature on Figure 1. This is the classical zero temperature grain boundary energy computed for this boundary and set of potentials. It differs slightly from the zero temperature value of γ due to the contributions to the excess free energy from changes in the quantum zero-point motion in the vicinity of the boundary.

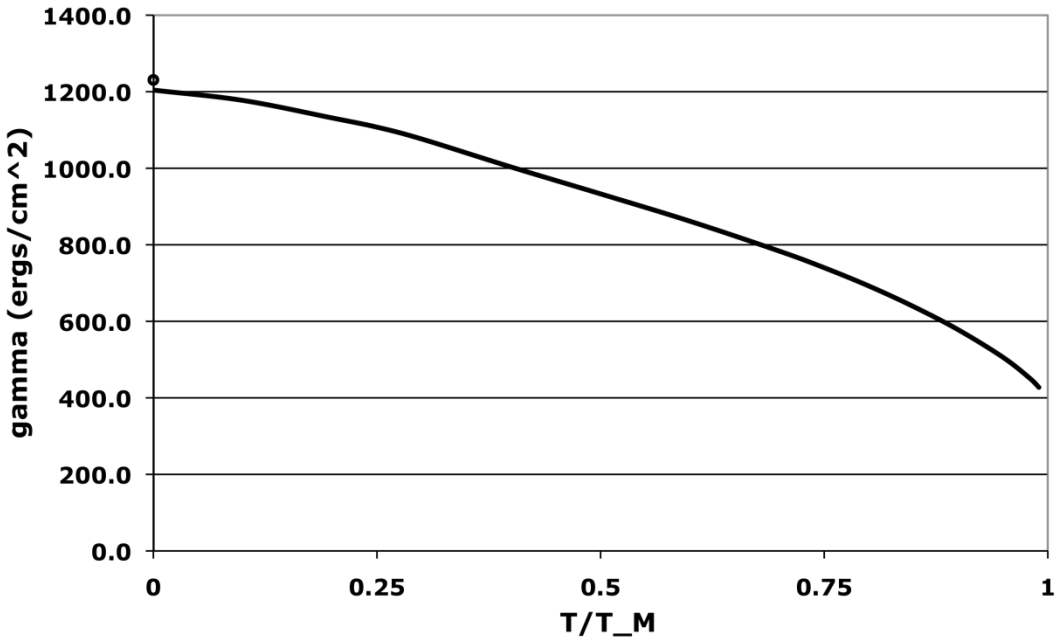

Figure 7-1. Temperature dependence of grain boundary free energy
The temperature dependence of the grain boundary free energy for a symmetric Σ79 tilt boundary computed as described in the text for a EAM model of Ni. The point at T=0 is the classical zero-temperature excess energy computed for this boundary.

The computed temperature variation of the elastic constants is presented in Figure 2. In particular, the bulk modulus, B, and the two shear moduli, $C = C_{44}$ and $C' = (C_{11} - C_{12})/2$ are presented. The experimental values of these elastic constants due to Ledbetter and Reed[18] are also shown. The difference between the low temperature calculated and experimental lattice constants reflects the imperfect fit of the interatomic potentials to the elastic constants. While a comparison of the temperature-dependence of the computed and experimental elastic constants is not the main point of this work, the reasonable agreement of the variation of the elastic constants compared to experiment supports the interatomic potential model used here.

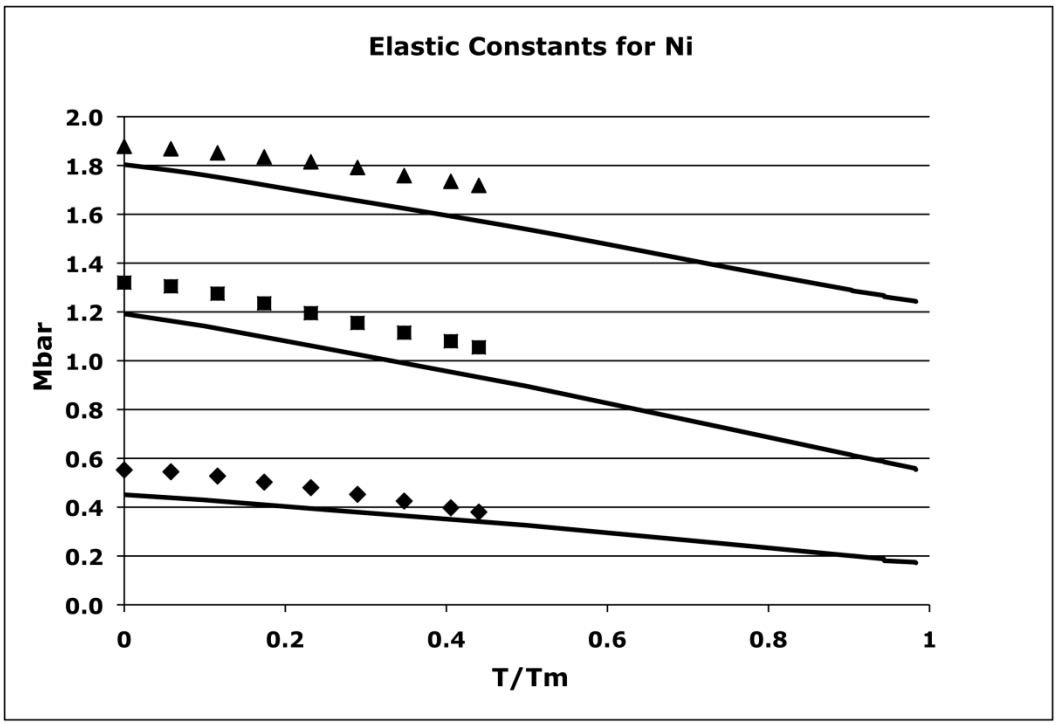

Figure 7-2. Temperature dependence of the elastic moduli
The computed temperature dependence of the elastic moduli for the EAM model of Ni (solid lines) along with experimental values (points) of the elastic moduli from Ledbetter and Reed [18]. The triangles are the bulk modulus, B, the squares are shear modulus, C, and the diamonds are the shear modulus, C'.

The main result of this paper is presented in Figure 3 that compares the variation of γ to the variation of the elastic constants. Note that γ has units of energy per unit area, but elastic constants have units of energy per unit volume. In order compare dimensionally equivalent quantities, we choose to compare γ to elastic constants multiplied by the temperature dependent lattice constant of the material. In particular, Figure 3 plots $R(T) = \frac{\gamma(T)B(0.2)a(0.2)}{B(T)a(T)\gamma(0.2)}$ and similar quantities for the other elastic constants, C and C'. Here the 0.2 represents a reference temperature of T = 0.2 T_M which is a temperature near room temperature. Note that if the temperature dependence of γ is proportional to the temperature dependence of the elastic constant times the lattice constant that this ratio will be unity. It is observed that scaling by the bulk modulus does not yield a constant value. Scaling by the shear elastic moduli provides a substantial reduction in the temperature variation over a substantial temperature range. In particular, if the grain boundary free energy is scaled by C*a, this ratio stays within 4% of unity for temperatures up to around 0.75 $T_{M.}$ At higher temperatures, the scaling with the shear elastic moduli breaks down. The scaling predicted based on C'*a is also reasonable though not quite as good. Similar results are obtained if one chooses T = 0 as the reference temperature.

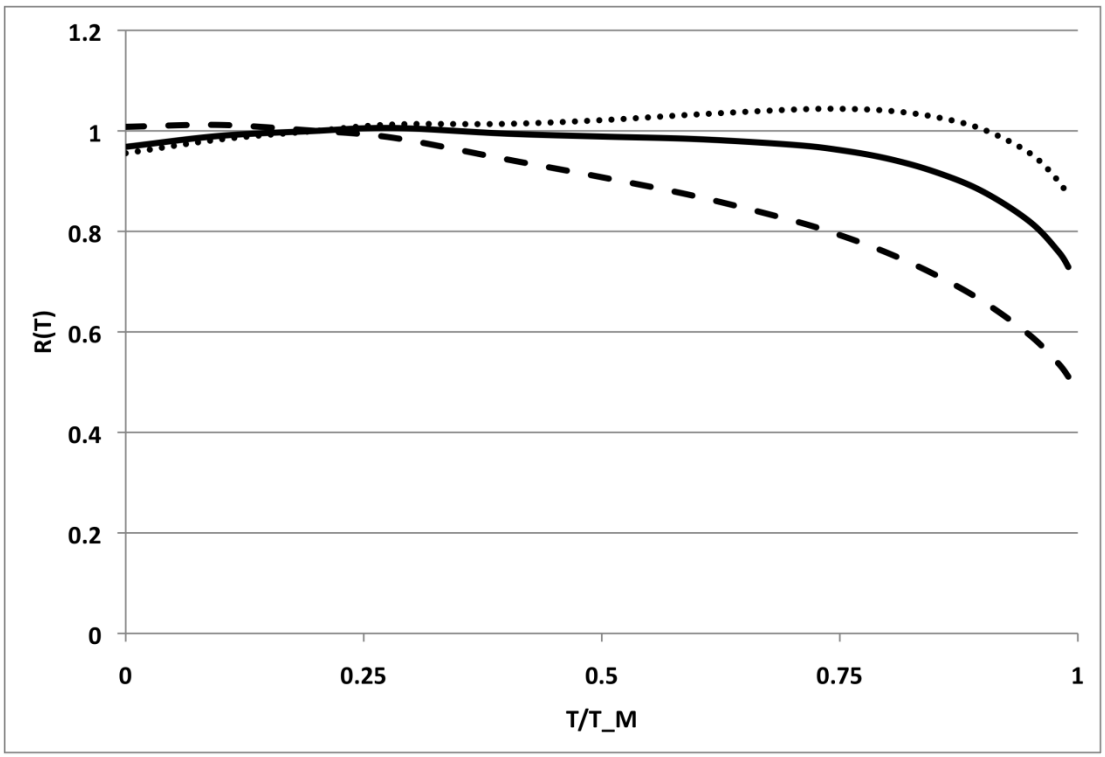

Figure 7-3. Scaled temperature dependent grain boundary free energy
The temperature dependence of the grain boundary free energy divided by the product of various elastic moduli times the lattice constant relative to the room temperature, R(T) as described in the text. The selected elastic moduli are the bulk modulus (dashed line), $C = C_{44}$ (solid line) and $C' = (C_{11} - C_{12})/2$ (dotted line).

This result suggests that for temperatures up to about 0.75 T_M, the variation of the grain boundary free energy can be estimated by scaling with the temperature dependence of C*a. Since the temperature dependence of elastic constants is in many cases measured or can be computed more easily than the temperature dependence of γ, this provides a convenient way to estimate γ at moderate temperatures. In addition, the idea that grain boundary free energy will scale with elastic constants has been incorporated into a recent phase-field model of grain boundary premelting [6].

The break down of this scaling relationship at high temperatures is reasonable. The scaling with elastic constants implicitly assumes that the dominant variation is due to the change in the elastic strain energy associated with the grain boundary. However, previous studies [19, 20] have shown that the defect formation energy of vacancies, interstitials and other defects at grain boundaries is lower than their formation energy in the bulk. Thus at high temperatures one would expect a contribution to the free energy from the thermal creation of such defects.

7.5. Summary

The temperature dependence of the grain boundary free energy, γ, has been computed for a symmetric $\Sigma 79$ tilt boundary for an EAM model of Ni. The calculations were based on quasi-

harmonic calculations at low temperatures and thermodynamic integration at moderate to high temperatures. In addition, the temperature dependence of the elastic constants of this model was computed. It was shown that variation of the grain boundary free energy with temperature can be estimated by scaling with the temperature dependent product of the shear elastic constants times the lattice constant up to temperatures of about three-fourths of the melting point. In this case study, C*a represents the scaling somewhat better than C'*a for temperatures $T < 0.75\ T_M$. This provides a convenient way to estimate the finite temperature grain boundary free energy at moderate temperatures. At higher temperatures, the scaling breaks down which is suggested to be due to the creation of thermal defects at the boundaries at high temperatures.

7.6. References

[1] Sutton AP, Balluffi RW. Interfaces in Crystalline Materials. Oxford: Clarendon Press, 1995.

[2] Cahn JW. Thermoynamics of Solid and Fluid Surfaces. In: Johnson WC, Blakely JM, editors. Interfacial Segregation. Metals Park: American Society for Metals, 1979. p.3.

[3] Foiles SM. Evaluation of harmonic methods for calculating the free energy of defects in solids. Physical Review B 1994;49:14930.

[4] Broughton JQ, Gilmer GH. Interface Melting: Simulations of Surfaces and Grain Boundaries at High Temperature. Journal of Physical Chemistry B 1987;91:6347.

[5] Broughton JQ, Gilmer GH. Harmonic analysis of Lennard-Jones FCC grain boundaries. Modelling and Simulation in Materials Science and Engineering 1998;6:393.

[6] Mellenthin J, Karma A, Plapp M. Phase-field crystal study of grain-boundary premelting. Physical Review B 2008;78:184110.

[7] Hirth JP, Lothe J. Theory of Dislocations. New York: John Wiley & Sons, 1982.

[8] Read WT, Shockley W. Dislocation Models of Crystal Grain Boundaries. Physical Review 1950;78:275.

[9] Olmsted D, Foiles SM, Holm EA. Survey of Computed Grain Boundary Properties in FCC Metals: I. Grain Boundary Energy. Acta Materialia 2009;in press.

[10] Udler D, Seidman DN. Grain Boundary and Surface Energies of FCC Metals. Physical Review B 1996;54:R11133.

[11] Daw MS, Foiles SM, Baskes MI. The embedded-atom method: a review of theory and applications. Materials Science Reports 1993;9:251.

[12] Foiles SM, Hoyt JJ. Computation of Grain Boundary Stiffness and Mobility from Boundary Fluctuations. Acta Materialia 2006;54:3351.

[13] Pao C-W, Foiles SM, Webb III EB, Srolovitz DJ, Floro JA. Atomistic simulaitons of stress and microstructure evolution during polycrystalline Ni film growth. Physical Review B 2009;79:224113.

[14] Pao CW, Foiles SM, Webb EB, Srolovitz DJ, Floro JA. Thin film compressive stress due to adatom insertion into grain boundaries. Physical Review Letters 2007;99:036102.

[15] Maradudin AA, Montroll GH, Weiss GH, Ipatova IP. Theory of Lattice Dynamics in the Harmonic Approximation. New York: Academic, 1971.

[16] Frolov T, Mishin Y. Temperature dependence of the surface free energy and surface stress: An atomistic calculation for Cu(110). Physical Review B 2009;79:045430.

[17] Wolf RJ, Mansour KA, Lee MW, Ray JR. Temperature dependence of elastic constants of embedded-atom-models of palladium. Physical Review B 1992;46:8027.
[18] Ledbetter HM, Reed RP. Elastic properties of metals and alloys, I. Iron, nickel and iron-nickel alloys. Journal of Physical and Chemical Reference Data 1973;2:531.
[19] Suzuki A, Mishin Y. Interaction of Point Defects with Grain Boundaries in fcc Metals. Interface Science 2003;11:425.
[20] Suzuki A, Mishin Y. Atomistic Modeling of Point Defects and Diffusion in Copper Grain Boundaries. Interface Science 2003;11:131.

8. Direct molecular dynamics simulations of nanocrystalline grain growth

8.1. Introduction

The results of Hattar et al. [1] show that grain growth in nanograined metals has some fundamental differences from that observed in conventional scale material especially for the case of abnormal grain growth. In convention materials, abnormal grain growth leads to grains which are largely defect free [2]. However, Hattar et al. showed that the annealing of pulsed laser deposited Ni thin films leads to abnormal grain growth. However, in this case there is a high defect density in the abnormally grown grains including twins, dislocation loops and stack fault tetrahedra.

In order to understand these experimental observations, direct molecular dynamics simulations of the growth of nanoscale grains have been performed. Current computer resources allow for the simulations of the dynamics of millions of atoms for times of several nanoseconds. This is sufficient to examine the high temperature evolution of a system of hundreds of grains with sizes of a few nanometers. Such simulations have been performed and analyzed to address two questions. First, are the dynamics of grain growth fundamentally different at the nanoscale than at conventional scales? Some prior molecular dynamics simulations by Farkas, Mohanty and Monk [3] suggested that grain growth is linear in time for nanoscale systems as opposed growth with the square root of time observed in conventional scale materials. The present results will challenge this observation. Second, the formation of defects during the growth will be examined to compare to the qualitative features of the experimental observations.

8.2. Computational Method

The simulation of the grain growth is performed by standard molecular dynamics simulations methods. In these simulations, the interatomic interactions are based on the embedded atom method (EAM) [4] potentials developed by Foiles and Hoyt [5] to describe Ni. In the following, temperatures will be presented in terms of homologous temperatures, ie relative to the melting point for these potentials. The melting point for these potentials is 1565 K compared to the experimental melting point of 1726 K. The simulations are performed in an isothermal-isobaric ensemble with periodic boundary conditions in all three directions and were performed using the LAMMPS [6] molecular dynamics code.

The initial atomic configuration was generated using a Voronoi cell construction. First, a set of points is chosen at random in the 3-dimension periodic cell. Each point is assigned a set of randomly determined Euler angles. The grains correspond to the Voronoi cells, region of space closer to a given point than to any other point, with the Euler angles defining the grain orientation. Atomic coordinates are then produced within each grain based on the FCC lattice rotated by the Euler angles. In the regions of the grain boundary, an atom is eliminated if it had an initial neighbor with 2 angstroms. This produces an initial grain structure. It should be noted

that while this grain structure fill space, it is inherently out of equilibrium since the grain boundary network so produced will not have the correct orientations at the triple junctions.

Results for two sizes of simulation cell will be discussed here. For the larger simulations performed here, the periodic cell has an edge length of $110a_0$ = 38.72 nm at zero temperature. There were 800 initial grains in these simulations. The total number of atoms was 5,103,926. This is less than the number that would be present in a single crystal of this volume due to the lower density of atoms at the grain boundaries. For the smaller simulations, the cell edge dimension was half this amount and there were 100 initial grains. The initial average grain size is thus the same in the smaller and larger simulations. The initial configurations were then relaxed to a local energy minima before being expanded by the known bulk thermal expansion for the desired temperature and then equilibrated for 10 ps.

The analysis of the resulting evolution is a non-trivial portion of the simulation. The approach used here is to examine the nearest neighbor environment of each atom. First, a coarse minimization of the finite temperature structure is performed to eliminate most of the thermal displacements of the atoms. The relative positions of the twelve nearest neighbors of each atom are compared to that for the nearest neighbor shell of an FCC lattice. In doing this, the rotational orientation of the reference FCC neighbor positions is optimized to provide the best fit between the actual relative neighbor positions and the ideal neighbor positions. If a satisfactory fit is obtained, the atom is considered to be in a FCC crystal and the optimal rotation determines the local crystal orientation. If a satisfactory fit is not obtained, the location of the nearest neighbors is compared that of an ideal HCP crystal and a similar optimization of the rotational orientation of the ideal HCP lattice is performed. For this case, it is assumed that the HCP lattice has the ideal c/a ratio of $\frac{c}{a} = \sqrt{\frac{8}{3}}$ with the lattice constant assume to be such that the volume per atom is the same in the FCC and HCP lattice. Calculations of the equilibrium HCP structure with these potentials indicate that this is approximately correct for these potentials. Finally, if there is not satisfactory fit to the HCP structure, the atom is then assign to be non-crystalline. Visualization of the resultant assignments (see below) indicates that the vast majority of these atoms are located at grain boundaries

There are two common ways that an atom will have a local HCP neighbor environment. The first is in a twin boundary where the local stacking sequence will be ABCBA. In this case, the atoms in the central C layer will have a first neighbor shell that corresponds to the HCP lattice while atoms in the adjacent layers will have a local FCC environment. This provides a means of identifying twin boundaries. In a twin boundary, an atom that has an HCP environment and has six nearest neighbors that also have an HCP environment will be assumed to be in a twin boundary. In the case of an intrinsic stacking fault, the stacking sequence is ABCABABCAB. In this case the atoms in the central B and A layers have local HCP environments. Thus the HCP environment atoms in an intrinsic stacking fault will nine nearest neighbors that also have an HCP environment. This can be used to identify intrinsic stacking faults.

The average grain size can be readily estimated from the above data. As discussed by Farkas, et al. [3], the average grain diameter, d, scales with the system volume, V and grain boundary area, A, by the relation $d \propto V/A$. Since the non-crystalline atoms are dominantly at the grain

boundaries, this suggests that $d \propto V / N_{non-crys}$. This provides a computationally efficient way to estimate the average grain size at a given time by simle counting the number of non-crystalline atoms.

In the following results from simulations at three different temperatures, T/T_M = 0.65, 0.75 and 0.85. The simulation at T/T_M = 0.65 was performed for the smaller system size discussed above and was run for 10 ns. The two higher temperature simulations were performed at the larger system size and were continued for 7 ns at T/T_M = 0.75 and 2 ns at T/T_M = 0.85.

8.3. Results

Figure 1 represents snapshots at a time interval of 1 ns for the simulations at the reduced temperature of 0.75. There are a couple of important qualitative observations that can be made based on the examination of the dynamics of all of the slices as a function of time. The most obvious feature is that there are a significant number of twin boundaries in the system. This is consistent with the experimental observation of Hattar, et al. [1] of a high density of twin boundaries in annealed pulsed laser deposited nanocrystalline Ni. Observation of the dynamics of the grain growth suggests that the twin boundaries form via a mechanism discussed by Mahajan, et al. [7]. In this mechanism, a growth accident occurs in the vicinity of a triple junction that forms a short segment of twin boundary. As the grains continue to grow, the twin boundary remains, but the triple junction moves away from the boundary as the grain structure coarsens. This results in a twin boundary that crosses the grain and grows as the overall grain grows.

Another qualitative observation is the presence of vacancies in the grains. An example of a vacancy can be seen in the snapshot at 3 ns in Figure 1. In the large reddish grain near the top of the image (and also its periodic image near the bottom), one can see a black shaded point defect. These are the non-crystalline atoms located adjacent to a vacancy. At these elevated temperatures, the vacancies are observed to be quite mobile in the visualization of the dynamics as one would expect. The presence of vacancies in the grain interiors is consistent with the presence of stacking fault tetrahedra in the experimental observations of Hattar et al. [1]. A stacking fault tetrahedra results from the clustering of vacancies [8]. Thus the presence of vacancies in the grain interiors in our simulations supports the conecture by Hattar et al. that the growth process introduces vacancies which in their case for the stacking fault tetrahedra. In the present simulations, the high temperatures and small grain sizes account for the absence of vacancy clusters in the simulation. For the simulation conditions, the vacancies are most likely to be absorbed at grain boundaries rather than form clusters.

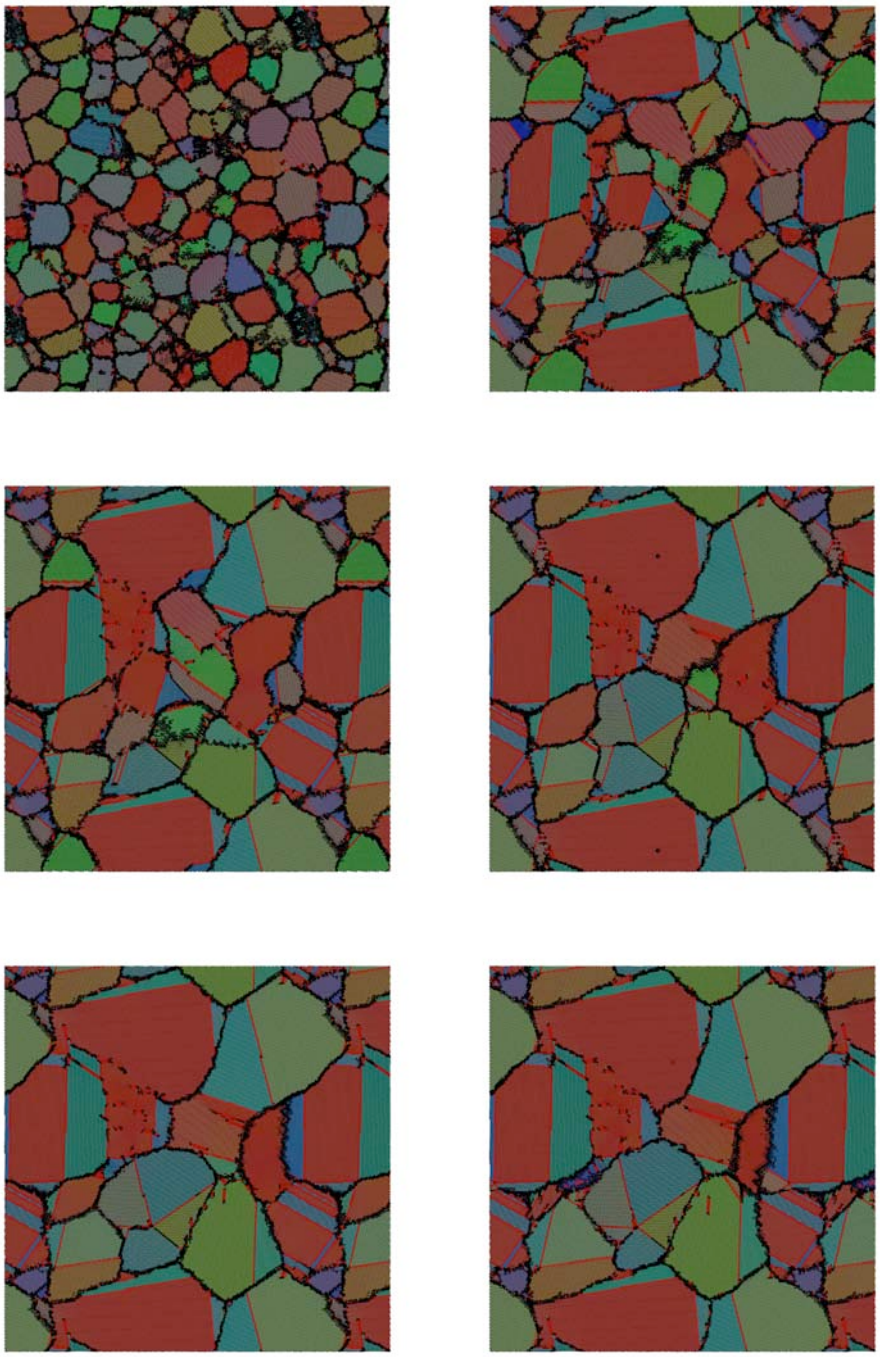

Figure 8-1. Representative snapshots of MD simulated grain growth
These are snapshots of a representative slice through the simulation cell for T/T_M = 0.75 at times of 0 to 5 ns in 1 ns increments. The black atoms are non-crystalline atoms, the red atoms have HCP nearest neighbor environments. The other colors have FCC nearest neighbor environments with the shade representing the local crystal orientation as discussed in the text. The image shows a region larger than the periodic boundaries of the computational cell.

The growth kinetics are presented in Figure 2 which presents the average grain size determined using the procedure described above as a function of the square root of time. It is well known that in conventional grain growth the average grain size grows as the square root of time. In the present results, one observes that after an initial transient that the average grain diameter follows the conventional square root of time behavior. The presence of a transient is expected in these simulations. The initial configuration of the grains that is contructed through the Voronoi procedure discussed above does not have the correct grain boundary angles at triple junctions. Thus the initial dynamics seen here is artificial as the system corrects the triple junction angles. After this initial transient, the growth is observed to follow a linear behavior in the square root of time for a significant period. This is consistent with grain growth in conventional scale materials. At later times for the two lower temperatures, the rate of grain growth falls below this trend and appears to be stagnating. We speculate that this behavior is related presence of a temperature dependent population of fast and slow boundaries due to the roughening transition discussed in an earlier chapter. This will be discussed more extensively elsewhere.

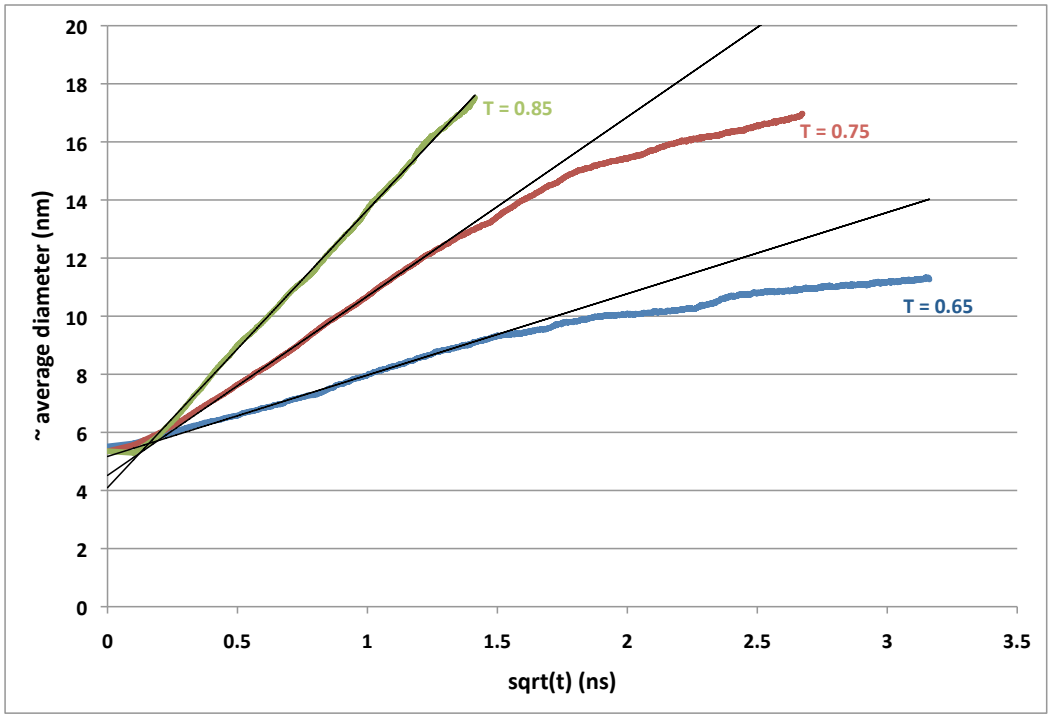

Figure 8-2. Time evolution of grain size
The average grain size determined as described in the text as a function of the square root of time for the three simulation temperatures.

The observation of parabolic grain growth kinetics in these simulations is at odds with the earlier results of Farkas, Mohanty and Monk [3] who claim to observe a linear increase in the grain size with time. There are two possible explanations for the disagreement with the earlier results. First, the earlier results do not account for the transient required to correct the triple junction angles. Since this transient is due to the arbitrary, somewhat unphysical, initial grain structure it is not expected to conform with experiment. Second, the earlier work uses a system with far fewer grains such that artificial system size effects are more likely. In the current work, the

simulations are halted well before largest grains com close to their periodic images. For these reasons, we believe that the earlier results are incorrect and that grain growth in the nanocrystalline regime follows parabolic kinetics consistent with grain growth in conventional scale metals.

8.4. References

[1] Hattar K, Follstaedt DM, Knapp JA, Robertson IM. Defect structures created during abnormal grain growth in pulsed-laser deposited nickel. Acta Materialia 2008;56:794.

[2] Humphreys FJ, Hatherly M. Recrystallization and Related Annealing Phenomena. Oxford: Elsevier, 1995.

[3] Farkas D, Mohanty S, Monk J. Linear Grain Growth kinetics and Rotation in Nanocrystalline Ni. Physical Review Letters 2007;98:165502.

[4] Daw MS, Foiles SM, Baskes MI. The embedded-atom method: a review of theory and applications. Materials Science Reports 1993;9:251.

[5] Foiles SM, Hoyt JJ. Computation of Grain Boundary Stiffness and Mobility from Boundary Fluctuations. Acta Materialia 2006;54:3351.

[6] Plimpton SJ. LAMMPS: Large-scale Atomic/Molecular Massively Parallel Simulator. Sandia National Laboratories, 2007.

[7] Mahajan S, Pande CS, Imam MA, Rath BB. Formation of Annealing Twins in FCC Crystals. Acta Materialia 1997;45:2633.

[8] Hirth JP, Lothe J. Theory of Dislocations. New York: John Wiley & Sons, 1982.

9. Distribution

1	MS0899	Technical Library	9536 (electronic copy)

Sandia National Laboratories